Nordic Concrete
Research

NCF | Nordic Concrete Federation

NORDIC CONCRETE RESEARCH

Preface

Nordic Concrete Research is since 1982 the leading scientific journal concerning concrete research in the five Nordic countries, e.g., Denmark, Finland, Iceland, Norway and Sweden. The content of Nordic Concrete Research reflects the major trends in the concrete research.

Nordic Concrete Research is published by the Nordic Concrete Federation which also organizes the Nordic Concrete Research Symposia that have constituted a continuous series since 1953 in Stockholm. The XXII Symposium was held i August 2014 in Reykjavik. Most of the papers in this volume of NCR is full papers, where only 4 pages extended abstracts were presented in Reykjavik.

The next symposium, no. XXIII, will be held Aalborg, Denmark in August 2017. We do look forward to welcome you there.

Since 1982, 423 papers have been published in the journal. Since 1994 the abstracts and from 1998 both the abstracts and the full papers can be found on the Nordic Concrete Federation's homepage: www.nordicconcrete.net. The journal thus contributes to dissemination of Nordic concrete research, both within the Nordic countries and internationally. The abstracts and papers can be downloaded for free. Proceedings from miniseminars and the proceedings from the Research Symposia are about to be published on the homepage as well.

The high quality of the papers in NCR are ensured by the group of reviewers presented on the last page. All papers are reviewed by three of these, chosen according to their expert knowledge.

Since 1975, 76 Nordic Miniseminars have been held – it is the experience of the Research Council of the Nordic Concrete Federation, that these Miniseminars have a marked influence on concrete research in the Nordic countries. In some cases, the information gathered during such Miniseminars has been used as Nordic input to CEN activities. The latest Miniseminar concerning Alkali Silica Reactions was held in Riga in our attempts to involve the Baltic countries in our Nordic activities.

The next miniseminar, " Residual capacity of deteriorated concrete structures" will be held in Trondheim, 21 - 22 of April.

Vodskov, December 2014

Dirch H. Bager
Editor, Nordic Concrete Research
Chairman, Research Council of the Nordic Concrete Federation

CONTENTS

EARLY PROPERTY DEVELOPMENT IN CONCRETE

Gitte Normann Munch-Petersen
Civil engineer, senior lecturer
VIA University College
Chr. M. Østergaardsvej 4
DK-8700 Horsens
E-mail: gin@via.dk

Christian Munch-Petersen
Civil engineer, MSc
Emcon a/s
Ordrupvej 60
DK- 2920 Charlottenlund
E-mail: cmp@emcon.dk

ABSTRACT

The Freiesleben Maturity-function is widely used for planning of execution, also for concrete containing fly ash. The strength and electrical resistance are investigated for concrete with and without fly ash at different curing temperatures. This investigation showed that the standard maturity function is not valid in general. Curing at high temperature gave a significant decrease in strength. Fly ash reduces this decrease for the 28-days strength, but not for long-term strengths. The resistance is reduced at high temperatures for concrete without fly ash, and increased for concrete with high fly ash content. The exact maturity function for a specific concrete type must be determined by experiments.

Key words: Additions, Chlorides, Execution, Testing

1 INTRODUCTION

In Denmark, planning of execution parameters like strength development is based on the Freiesleben Maturity function. The parameters for the maturity function is only tested for 12 to 48 hours and from 5˚C to 40˚C according to the test method for the maturity function [1]. In most cases standard values for these parameters are used without testing regardless of the concrete composition and the cement type. The Freiesleben Maturity function is widely used for planning of execution, also beyond the maturity which it was derived for and also for concrete containing fly ash, even though fly ash was not used at the time when the function was derived. By using additives that act retardant, it is a fact that the influence of temperature on the retarding period is not described accurately by using the maturity function. [2]

Freiesleben Maturity function is given by:

$$H_{20}(\theta) = \exp\left(\frac{E(\theta)}{R} \cdot \left(\frac{1}{293} - \frac{1}{\theta + 273} \right) \right) \tag{1}$$

Where:

- $H_{20}(\theta)$ Relative speed at temperature θ
- $E(\theta)$ Standard Activation Energy, [J/mol]

$$E(\theta)=\begin{cases} 33500 \text{ J/mol, for } \theta \geq 20^{o}C \\ 3350+1470\cdot(20-\theta) \text{ J/mol, for } \theta < 20^{o}C \end{cases}$$

The maturity is the equivalent hardening time at 20˚C. At the time τ, it can be calculated as:

$$M_{20}=\int_{0}^{\tau} H_{20}(\theta)dt \qquad\qquad (2)$$

In Denmark the standard activation energy parameters is often used without any documentation, and determination by testing according to method TI-B 103 (94) [3] is seldom done.. In practice, the maturity function with the standard parameters regardless of concrete mix design and cement type is used far beyond the period and temperatures for which it is actually valid and the consequence of this is not generally known in the concrete industry.

Concrete structures service life is a key factor in ensuring the economy and the environmental profile of large infrastructure projects. For a number of concrete properties the development between 6 hours and 28 days (and after 28 days) is poorly known, and for the modern concretes with addition of residues (fly ash) almost unknown. Nevertheless it is during this period that the concrete is subjected to excessive impacts associated with de-moulding, wetting, loading (pre stressing) and exposure to the environment (e.g. sea water). If the concrete is exposed too early, it will reduce the durability of the concrete.

A detailed knowledge of property development in modern concretes is therefore essential to provide the necessary and sufficient requirements and to formulate and implement realistic schedules without reduction in the durability of concrete.

In recent years it has been a growing recognition that concrete properties in the long term cannot be seen independently of the temperatures during curing. At very high temperatures (above 60-70 °C), there is even in some cases a subsequent total destruction of the concrete (DEF - Delayed Ettringite Formation). It is possible that even at lower and more common temperatures a smaller, partial degradation of the concrete will take place.

Kjellsen et al. [3] investigated the microstructure of concrete cured at temperatures between 5˚C and 50˚C. They found that low curing temperature resulted in a uniform distribution of hydration products and fine pores, while curing at higher temperatures resulted in coarse, interconnected pores. A proportion of the pores will always remain unfilled, and the poorer physical structure will cause a lower strength and durability.

The influence of fly ash and curing temperature on compressing strength has been investigated by Maltais & Marchand [4]. This investigation clearly confirmed that an elevation of the curing temperature contributes to reduction of the long-term compressive strength of ordinary Portland cement mixture. It also indicated that a higher curing temperature is much less detrimental for fly ash mixtures.

The strength of concrete is according to the standards tested under laboratory conditions, at a constant temperature of 20̊C. I n real constructions, the temperature inside the concrete in massive constructions, can reach 50-60 ̊C or even in some cases 70-80 ̊C. There are only a limited number of studies of how concrete with fly ash is affected by the temperature regarding to strength and durability of concrete structures.

The objective of this paper is to investigate the temperature interval were the Maturity function is reliable for different concret types and to investigate how curing at different temperatures affect the resistance against diffusion.

The survey was conducted with fixed temperatures over a longer period, to determine how long the Maturity function is valid with modern types of concrete.

2   EXPERIMENTATION

The tests carried out comprise curing of concrete in a temperature range from 20 °C to 70 °C. Three commercially available concrete types were used with varying content of fly ash. The cement was the Danish Rapid cement, which is a CEM I 52,5 N (LA) with a C_3A less than 8%. The commercial name includes "Rapid" for historical reasons, but according to EN 197-1 this cement is normal hardening.

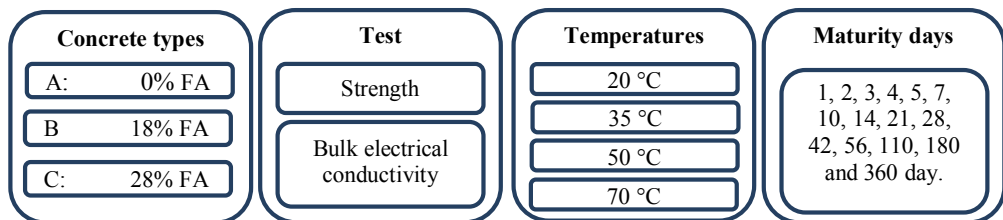| Concrete types	Test	Temperatures	Maturity days
A: 0% FA B 18% FA C: 28% FA	Strength Bulk electrical conductivity	20 °C 35 °C 50 °C 70 °C	1, 2, 3, 4, 5, 7, 10, 14, 21, 28, 42, 56, 110, 180 and 360 day.

Figure 1 Test programme

The specified day is the maturity day. The function is based on The Arrhenius function. This has the consequence, that if the maturity function was correct a given mix would obtain the same strength at the same maturity days. Any deviation from this is therefore a symptom on the maturity function being wrong. In addition – if the maturity concept is correct – the long term strength must be independent of the temperature history.

Concrete mix used in this study are listed in Table 1. All concrete were delivered by UNICON and are commercial mixes.

Table 1 Concrete mix design for the used concrete mixes

Material	Type	A kg/m^3	B kg/m^3	C kg/m^3
Cement	Rapid CEM I 52,5 N (LA)	393.6	339.0	205.0
Fly ash	Emineral B4	-	61.0	57.4
Water	Koldt procesvand Horsens	161.7	151.6	165.6
Air entrainment	Amex SB 22	1.1	0.8	0.3
Plasticizers	Lubricon N20	1.6	2.4	1.6
Super plasticizers	Glenium Sky 531	1.4	1.6	-
Equivalent water content		165	155	167

Sand	E0002 NCC Vestbirk	686.5	687.2	812.7
	E0408 Halsvik - Dalsøyra	209.0	-	-
Stones (4-8 mm)	E0508 Ansit - Rekefjord	-	212.9	-
	P0408 NCC Vestbirk	-	-	248.6
	E0816 Halsvik - Dalsøyra	836.2	-	-
Stones (8-16 mm)	E0816 Ansit - Rekefjord	-	851.8	-
	P0816 NCC Vestbirk	-	-	743.0
Fly ash		0 %	18 %	28 %
Desired air content, vol. %		6.0	6.0	4.5
Equivalent w/c-ratio		0.419	0.419	0.715
Start time for mixing concrete		12:11	11:28	11:08
Setting completed		15:30	16:00	18:00

After casting the concrete cylinders (still in the steel moulds) were placed in the water vessel immediately after setting was completed, see Table 1. Next day, the test cylinders were taken out of its mould, labelled and taken back into the water vessel.

3 METHODS

3.1 Compressing strength

Measurement of compressing strength in accordance with the test method DS/EN 12930 "Testing hardened concrete –Part 3: Compressing strength of test specimens" ". The used test equipment is named ADVANTEST 9th.

For each concrete composition and at each curing temperature the compressing strength of the test specimens was measured at the maturity days: 1, 2, 3, 4, 5, 7, 10, 14, 21, 28, 42, 56, 110, 180 and 360 days.

The stated maturity days are days - assessed by the commonly agreed Freiesleben maturity function. This means that the results can be interpreted as deviations from the generally accepted maturity function.

After the compressing strength was measured, curve fitting was made on strength development curves from the experimental data. The exponential equation proposed by Freiesleben Hansen and Pedersen 1977 [5] was used:

$$f_c = f_\infty \cdot \exp\left[-\left(\frac{\tau}{M}\right)^\alpha\right] \tag{3}$$

Where:

- $f_{c,\infty}$ the total strength development for M tending to infinity [MPa]
- f_c the strength at the maturity M, [MPa]
- M concrete maturity in hours [h]
- T   time constant [h]
- A   curvature parameter [-]

3.2   Bulk electrical conductivity

Measurement of conductivity (resistance) in accordance with the test method ASTM C1760-12 "Standard Test Method for Bulk Electrical Conductivity of Hardened Concrete". The used test equipment is named Merlin, from Germann Instruments.

The bulk electrical conductivity was measured at the same maturity days as the compressing strength was measured.

Curve fitting was made on resistance development curves from the experimental data

It was assumed that the curves with good approximation could be described by the exponential equation shown:

$$\Omega = \Omega_\infty \cdot \exp\left[-\left(\frac{\tau}{M}\right)^\alpha\right] \tag{4}$$

Where

- Ω_∞ the total resistance development for M tending to infinity [Ωm]
- Ω the resistance at the maturity M, [Ωm]
- M concrete maturity in hours [h]
- τ time constant [h]
- α curvature parameter [-]

The Merlin was used to measure the bulk electrical conductivity, of saturated 100 by 200 mm concrete cylinders.

The electrical resistance R of a conductor of length L and uniform cross-sectional area A is given by the equation:

$$R = \rho \frac{L}{A} \tag{5}$$

Where:

- R   electrical conductivity [mS/m]
- ρ electrical resistivity [ohm]
- L   length of the cylinder [m]
- A   cross-sectional area [m^2]

In assessing the ability of a concrete mixture to resist penetration of a particular type of ion, one of the key properties is the diffusivity, which defines how readily the given type of ion will migrate through saturated concrete in the presence of a concentration gradient. For a saturated porous material, such as hardened concrete, the diffusion coefficient of a give type of ion can be related to electrical conductivity through the Nernst-Einstein equation as follows [6] and [7]:

$$\frac{\sigma}{\sigma_p} = \frac{D}{D_w} \tag{6}$$

Where:

- σ   bulk electrical conductivity of the saturated porous material [mS/m]
- σ_p conductivity of the pore fluid
- D   bulk diffusion coefficient of the specific type of ion through the porous material
- D_w diffusion coefficient of the specific ion through water [8]

If the conductivity of the pore fluid is assumed to be similar among different concretes (which is hardly always the case), the measured bulk electrical conductivity is related directly to the bulk diffusion coefficient [9]. Measurement of the bulk diffusion coefficient of a particular type of ion through concrete is a time consuming process, while electrical conductivity can be measured in a matter of seconds.

The electrical conductivity of saturated cement paste is related to the paste porosity (volume of pores and how they are connected). The paste porosity is in turn related to the degree of hydration, the types of cementitious materials, and the water-cementitious materials (w/c – ratio).

The conductivity of the pore fluid affects the measured specific electrical conductivity of the concrete. Therefore, one cannot compare the measurements on concrete if there is a big difference in pore fluids conductivity. Concrete with fly ash can have a reduced conductivity of the pore fluid, which will reduce the conductivity measurement, although the actual diffusivity is not reduced. The conclusion must be that, since there are different levels of fly ash in the 3 types of concrete, the development may be compared, while the absolute level cannot be compared without additional studies of the actual diffusivity at a couple of selected dates. Unfortunately, this has not been possible within the project's limited budget.

4   RESULTS AND DISCUSSION

4.1   Results

The influence of temperature on strength development
In Figure 2, the measured compression strength is compared with the curing temperature, by 1, 7, 28, 180 and 360 days.
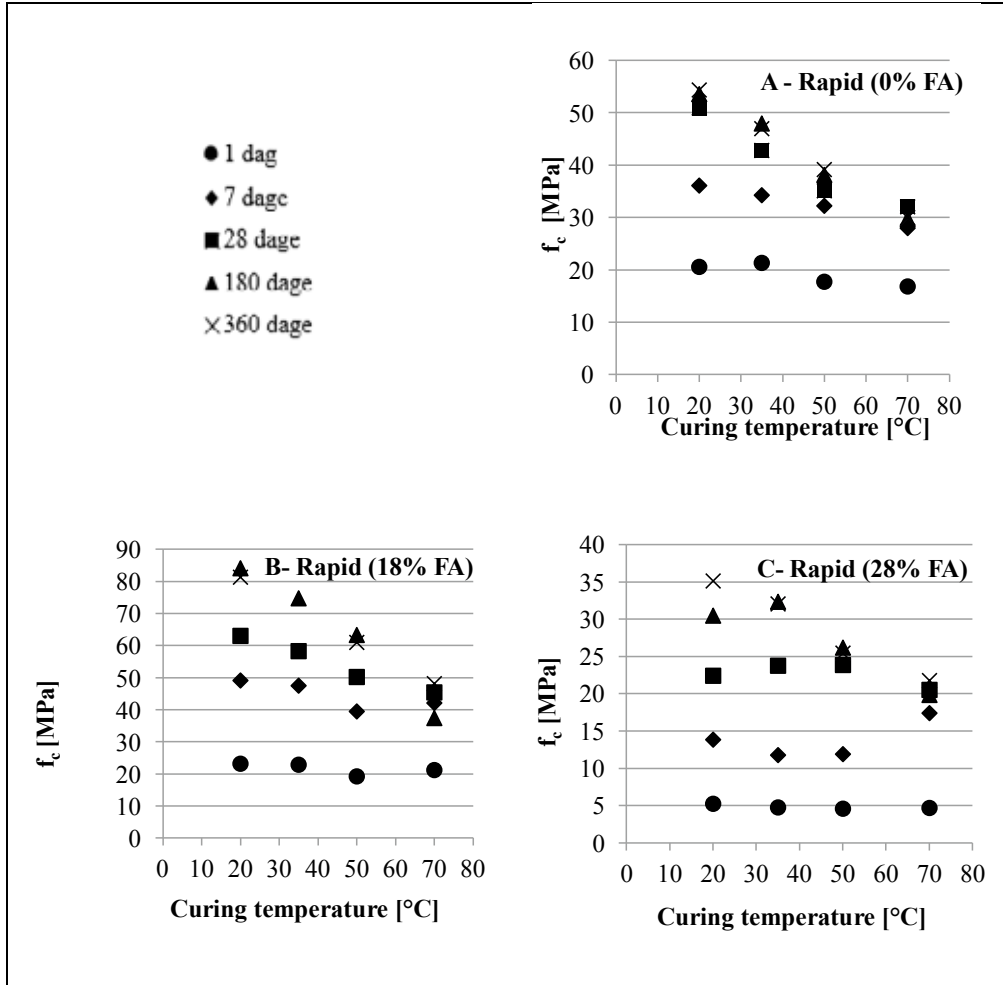
Figure 2 Measured strength

Based on the measured data strength developing curves are carried out from formula(3). The fitted curves can be seen in Figure 3.
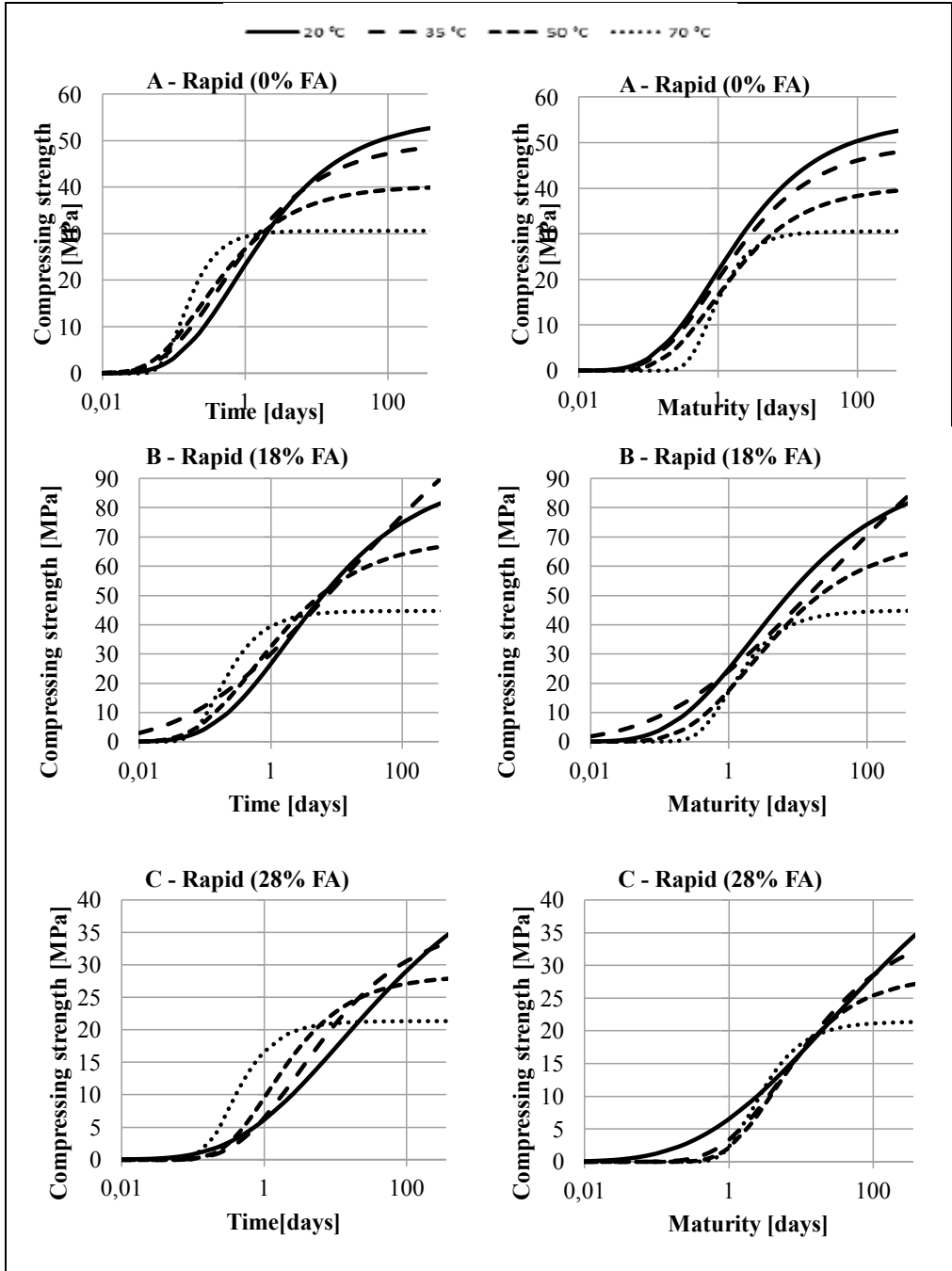
Figure 3 Strength development
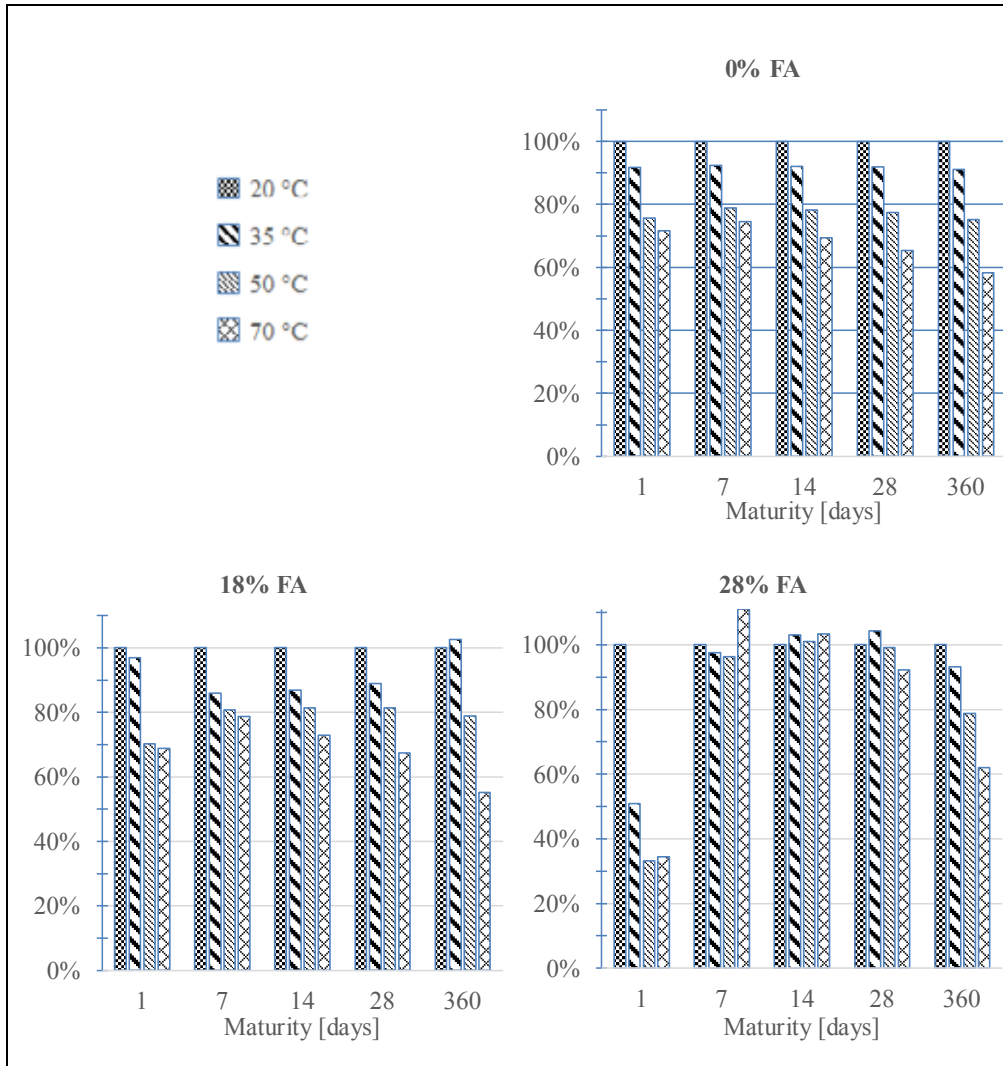
Figure 4 Achieved strength compared with the strength at 20 ˚C

For all three types of concrete, it applies that the 28 days of strength obtained at 20 °C was not obtained for concrete cured at 70 °C, and for concrete type A and B the strength were not obtained even if the concrete is stored at 50 °C.

For concrete cured at 50 °C the long term strength was app. 80% compared with the strength at 20 ˚C, and for concrete cured at 70 °C the long term strength was app. 60% compared with the strength at 20 ˚C (Figure 4).

From Figure 4 it can be seen that for concrete with fly ash the strength after 1 day was significant lower at curing temperatures of 50 and 70 degrees, and it was seen that the difference is significant higher at higher content of fly ash. For the concrete with 28% fly ash the 28- days

strength was not affected by high curing temperatures, but still the long term strength was affected.

Generally, the strengths at 50 and 70 ° C were significantly lower than the strengths of 20 and 35 °C. Strength curves for 20 and 35 °C were almost identical, if uncertainties in the measurements were included.

The measurements show therefore, that the maturity function of the tested concretes, only with considerable uncertainty can be considered to be only fairly valid up to 35 °C.

The influence of temperature on bulk electrical conductivity
In Figure 5, the measured bulk electrical conductivity is compared with the curing temperature, by 1, 7, 28, 180 and 360 days. The measured values are corrected since the resistance decreases with increasing temperature.
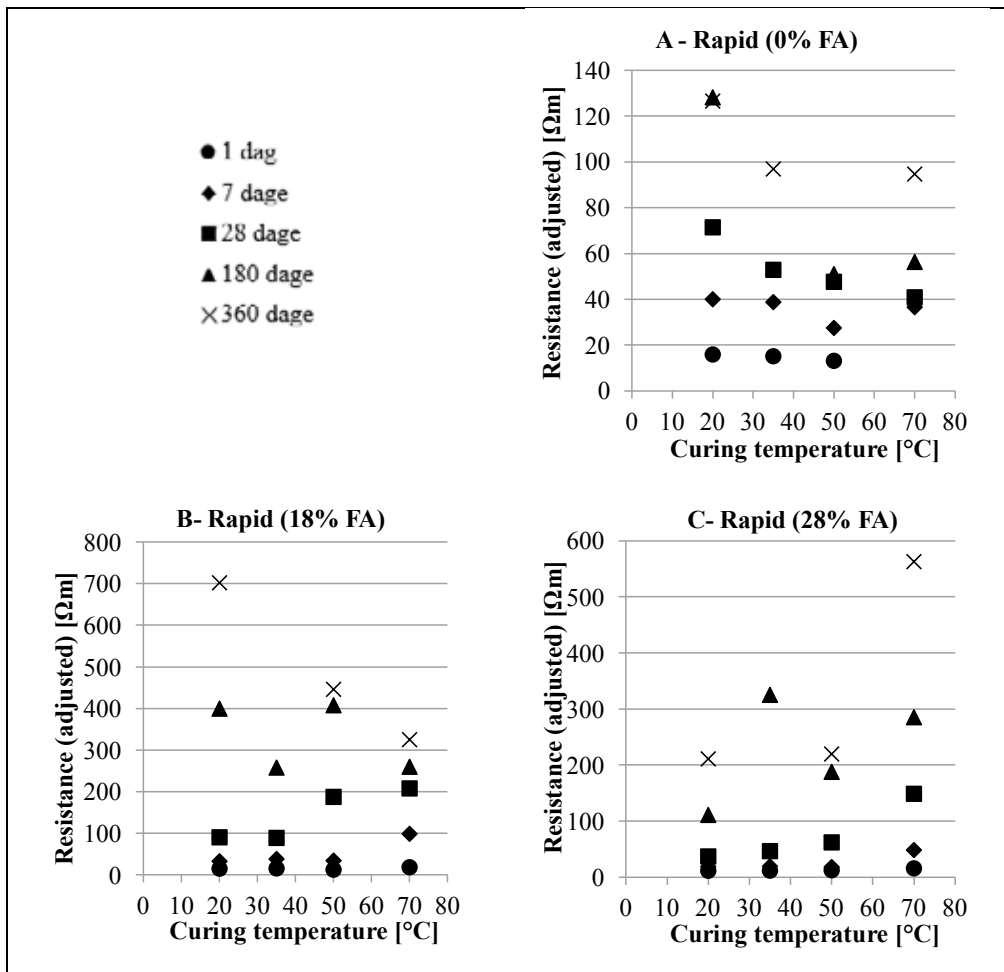
Figure 5 Measured resistance (adjusted)

Based on the measured data resistivity developing curves are carried out from formula (4). The fitted curves can be seen in Figure 6.
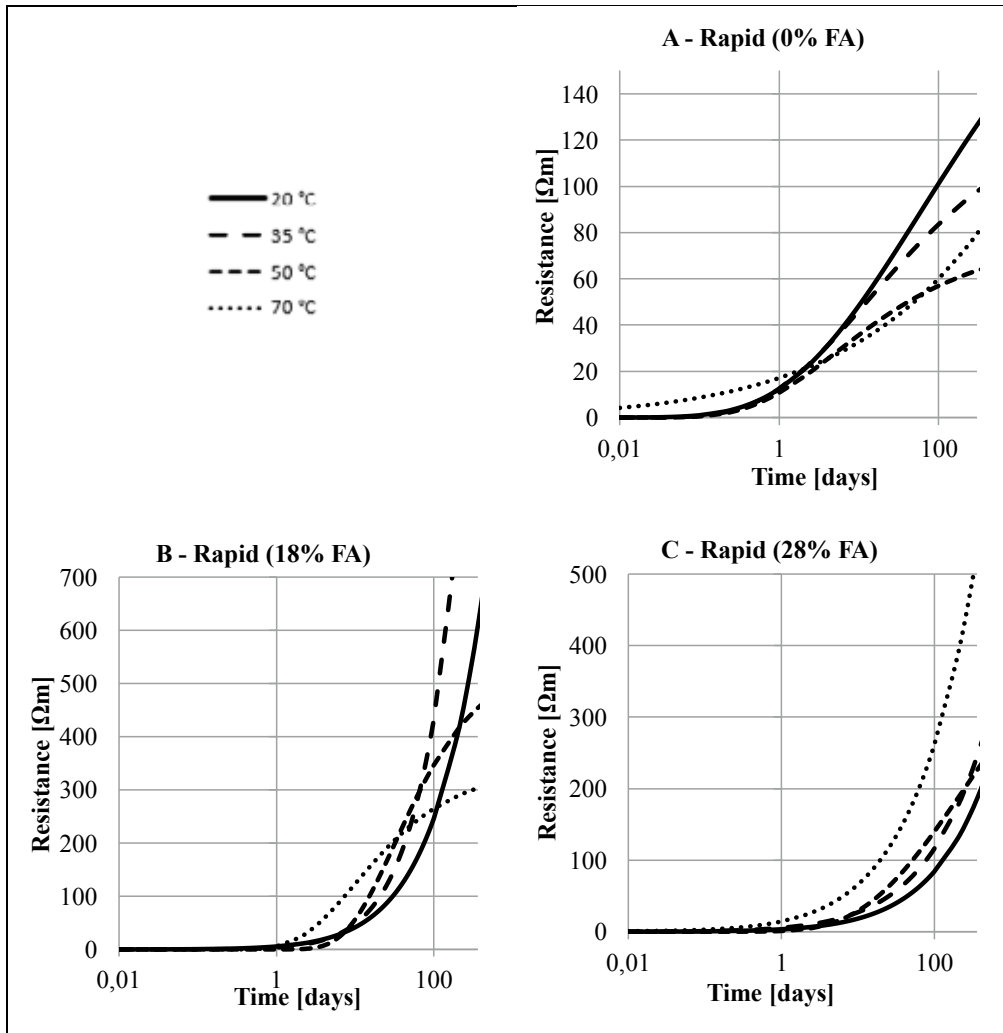

Figure 6 Development in resistivity

For concrete type A (without FA) it was seen that at almost all dates the resistance was higher the lower the curing temperature. This corresponds well with the strength development.

For concrete type B, containing 18% FA, it was seen that the resistance at the early dates was highest at 70 °C, but the curve flattens after 15 days while the other curves were still increasing. After 360 days the resistance at 20 °C were twice as that at 70 °C and at 35° C the resistance was three times as that at 70 °C.

For concrete type C containing 28% FA, it was seen that the rising temperature, gave higher resistance, i.e. curing of concrete with high content of fly ash at high temperatures encouraged the development of the resistance (and therefore also the chloride resistance).

4.2   Discussion

Based on this very small series of tests it can be concluded, that the traditional Danish maturity function used with the standard parameters does not give reasonable results for strength development at temperatures higher than 35 ^{o}C. For the electrical resistance (correlated to chloride penetration parameters) the maturity function used with the standard parameters does not give reliable estimations after 10 days for any temperature. Even if the maturity function was developed on concrete without additions, it seems that concrete with fly ash performs somewhat closer to the maturity function.

Concrete with high fly ash content, seems to withstand curing at high temperatures, without any affect on the 28 days the strength. However, the long term the strength is reduced just as much as for the concrete with less or no fly ash.

Since the three types of concrete develop differently at the high temperatures, the Arrhenius temperature function cannot be used. There must be other parameters than the temperature of importance - probably primarily concrete binder composition.

Furthermore, it is seen that if concrete is heat cured at more than 35 ˚C, it generally achieve lower strength than concrete cured at 20 ˚C. This is not only caused by the very long exposures at high temperatures. Other research shows clearly that there is a decrease in the final strength when concrete is exposed to high temperatures at an early age - even if the temperature in the rest of the lifetime is normal. This is due to a relatively more uniform microstructure of the hydrated cement paste [1].

This means in principle that in the future either all concretes maturity development has to be investigated, or new investigations should be done to find the parameters for how temperature influences the final property development.

The electrical resistance can for some mixes with fly ash become substantial higher at elevated curing temperatures. This could indicate that the durability might be improved by heat curing. On the other hand the high resistance may also be due to leaching of alkali ions at elevated temperatures, especially for long term results. It requires further investigation to determine the actual cause.

5   CONCLUSION

Three concrete mixes with 0, 18 and 28% of fly ash were tested for strength and electrical resistance after curing at 20, 35, 50 and 70 ˚C. The long term strength and the electrical resistance were highly dependent on the temperature history, and the maturity function used with the standard parameters could only foresee the strength at temperatures up to 35 degrees.

Concrete with fly ash followed the maturity function better than concrete without fly ash.

In this research the temperature were held constant in the whole period. The is not the case in real-life in-situ castings, but can be the case in special industrial production of concrete products as sleepers etc. Further research must be carried out to see if a more normal temperature history affects the concrete properties in the same way – for example if a temperature history where the temperature rises from 20 ˚C to 70 ˚C and back to 20 ˚C again during a few days also affects the long term strength.

It can nevertheless be concluded that, the exact maturity function for a specific concrete mix design must be determined by experiments on the actual mix design.. Great care must be taken if the maturity function with standard parameters is used, especially at temperatures above 35 ˚C and for concrete older than a few days..

REFERENCES

[1] *TI-B 103 (94): Prøvningsmetode. Aktiveringsenergi i den relative hastighedsfunktion,* Teknologisk Institut, 1994.

[2] T. H. Rasmussen og T. Andersen, *Hærdeteknologi,* Aalborg, Denmark: Aalborg Portland, 1989.

[3] K. O. Kjellsen, R. J. Detwiler og O. E. Gjorv, »Developement of Microstructure in plain hydrated at different Temperatures,« *Cement and Concrete Research. Vol. 20,* pp. pp. 927-933, 1990.

[4] Y. Maltais og J. Marchand, »Influence of curing temperature on cement hydration and mechanical strength development of fly ash motars,« *Cement and Concrete Research,* årg. 27, nr. 7, pp. 1009-1020, July 1997.

[5] P. Freiesleben Hansen og E. Pedersen, »Maturity computer for controlled curing and hardening of concrete,« *Nordiska Betongfoerbundet,* pp. 21-25, 1985.

[6] K. Snyder, C. Ferraris, N. Martys og E. Garboczi, »Using Impedance Spectroscopy to Assess the Viability of the Rapic Chloride Test for Determining Concrete Conduktivity,« *Journal of Research of the National Institute of Standards and Technology,* årg. 105, nr. 4, pp. 497-509, July-August 2000..

[7] M. Nokken og R. Hooton, »Elctrical conductivity testing,« *Concrete International,* pp. 58-63, 2006.

[8] R. Mills og . V. M. M. Lobo, »Self-Diffusion in Electrolyte Solutions,« Elsevier,, New York, 1989.

[9] N. Berke og M. Hicks, »Estimating the Life Cycle of Reinforced Concrete Decks and Marine Piles Using Laboratory Diffusion and Corrosion Data,« i *Corrosion Forms and Control for Infrastructure*, ASTM STP1137, 1992, pp. 207-231.

[10] T. Institut, *TI-B 103 (94) Prøvningsmetode: Aktiveringsenergi i den relative hastighedsfunktion,* 1994.

[11] P. K. Mehta og P. J. M. Monteiro, Concrete: Microstructure, properties and materials, Fourth Edition, McGraw-Hill Education books, 2014.

Design of a simple and cost-efficient mixer for matrix rheology testing

Serina Ng
PhD, Research Scientist
SINTEF
Richard Birkelandsvei 3
NO 7465 Trondheim
Email: Serina.Ng@sintef.no
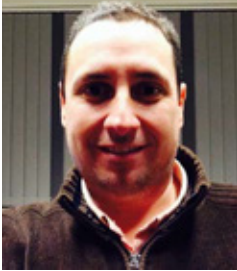
Hernan Mujica
Civil Engineer
Velde Betong AS
Noredalsveien 294
4308 Sandnes
Email: Hernan@veldeas.no

Sverre Smeplass
Prof. II, Dept leader, Skanska Technikk
Skanska Norge AS
Drammensveien 60
Skanskahuset Oslo
Email: Sverre.Smeplass@skanska.no

Abstract

A novel, simple and cost efficient mixer setup was investigated here. The results showed that at the moderate shear rate of 1,850 rpm, the new mixer setup produced matrixes which possessed good homogeneity and flowability, little air entrainment and stable temperature, showing little influence on the heat of hydration of the matrix. This is designed for usage on mixing matrix at lab scale, with the aim to obtain better rheological correlations between the matrix phase and concrete at an affordable price.

Key words: Mixer, matrix-concrete correlation, rheology, calorimetry

1.   INTRODUCTION

Small scale testing, utilizing cement pastes representing full scale concretes were often the choice for investigation in research to increase efficiency and also reduce materials, labour and cost. However, in practical applications, the paste is rarely used alone, but instead in

combination with coarser materials such as aggregates to form concrete. Therefore, accurate correlation of the research findings on cementitious pastes to concretes is of great interest.

In general, workability of concrete is often of great interest to the user. Among which, the shear rate during mixing is one of the most important parameters affecting the rheological properties of the pastes or concrete [1–3]. It has been shown that through the Particle Matrix (PM) model, prediction of the workability of specific concrete types such as ordinary concretes, self-compacting concrete (SCC) or low weight aggregate concrete (LWAC) could be derived [4, 5]. PM model was developed and verified by Ernst Mørtsell as part of his dr. ing. Thesis [6]. There, it was demonstrated that the workability of concrete is a result of the inherent properties of the constituents, the mix proportions and the physical and chemical interference between them. In simple terms, the concrete can be considered as a two phase material consisting of a matrix phase and a particle phase, or as defined by their properties, the fluid material and frictional material. By definition, the matrix phase consist of water, added chemical additives and all fines, including cements, pozzolans and aggregate fines with particle size below 125µm. The particle phase, on the other hand consists of all other particles with particle sizes greater than 125µm.

Despite the applicability of this model, there exist still some limitations for example in some cases, the performance of admixtures such as superplasticizers in a cement paste or concrete cannot be drawn directly from the PM model as a result of the additional shearing impact arising due to presence of aggregates in a concrete [7]. In general, concrete is normally mixed with a moderate shear rate in the order of 10^2 rpm. Additional shearing from aggregates result in higher shear exerted on the matrix in concrete and can better disperse admixtures such as superplasticizers. The increased dispersion of such admixtures can in turn improve or worsen their performances on influencing the rheology of concrete as compared to matrix when both systems are processed under the influence of the same external shear forces. As a result, the deviation arising from the shear effect of aggregates, or so called the frictional phase in the PM model thus influence greatly the correlation between the rheological properties obtained when testing at the matrix level versus in the concrete.

Different attempts were made to improve this rheological correlation between matrix and concrete through parametric studies of the impact of different existing mixing methods [8,9] or even via the investigation of the flow properties of sieved cement pastes from normally proportioned concretes [10]. In a rheological study employing the rheometer by Williams e*t al*, it was found that moderately high shearing (~ 1500 rpm) produced pastes with the most ideal rheological properties similar to the matrix phase sieved from a 'drum mixed concrete' [11]. On the other hand, low shear mixing (< 500 rpm) resulted in more viscous pastes which are more sensitive to pre-shearing. From literature, it can thus be clearly seen that a moderate shearing of the matrix phase can produce results which can be extrapolated to the rheological values expected in a concrete.

In a separate case, according to the standard ASTM C1738-1 [12], high shear mixing was adapted in laboratory research on rheology of hydraulic cement systems as it had been shown that increased shearing allows the paste to have similar rheological properties to that in concrete, similar to the study by Williams *et al*. In this standard, the tested shear speed was initially 4,000 rpm, followed by a second pre-set speed of 12,000 rpm. Due to the high shear rate, rapid rise in temperature was observed which was identified there as one of the key parameters in affecting the matrix through enhancing the hydration process. This increase in temperature is generally absence in normal concrete mix. Therefore, in this setup, isothermal conditions were maintained

throughout mixing, which increased the cost price of the setup. Entrained air, on the other hand, was identified as a minor factor according to the standard ASTM C1738-1.

The current research available demonstrated that a shear mixer with a moderate speed of $\sim 10^3$ rpm is required for good correlation of workability between matrix and concrete. Currently, an isothermal setup is already in place as presented in the ASTM C178-1 standard. However, this setup is costly which is not so practical for simple laboratory usage. Therefore, the aim of this article was to present and test a new mixer setup which is suitable to be used for good correlations between the matrix and concrete (moderate shear rate of $\sim 10^2$ rpm) at an affordable price. In this way, a routine lab mixing device can thus be developed and be employed in general laboratories with ease.

2.   MATERIALS AND METHODS

2.1   Mixer setups

A total of three different setups are presented in this paper. The novel mixing setup was compared with two conventionally used laboratory setups. The main difference between the three setups was their mixing speeds.

For low speed mixing (up to ~150 rpm), the Hobart mixer was employed. The new mixing setup has a moderate mixing speed of ~2,000 rpm. For high shear mixing, the Waring blender was selected and it was employed at a shear rate of 12,000 rpm. Details of the mixing conditions are displayed in Table 1. The prices of the different mixers were also included for comparison. For the Waring setup maintained under isothermal condition as mentioned in ASTM C1738-1, the usual price range between 100k to 200k NOK. Due to the high price, this condition was not tested in this study. For Hobart mixing, 2 different blades were utilized to highlight the effect of blade types (Figure 1).

Table 1 – Different mixer setups used in investigation

No.	Mixer	Blade	Speed$_{low}$ [rpm]	Speed$_{high}$	Cost [NOK]
1	Waring blender	Vortex blade	4,000	12,000	~10,000
2 3	Hobart	Flat Round	75	150	~13,000
4 5	Drill mixer	Steel Plastic	1,000	1,850	~3,000

*All speeds given are approximation, depending on the viscosity of the matrix
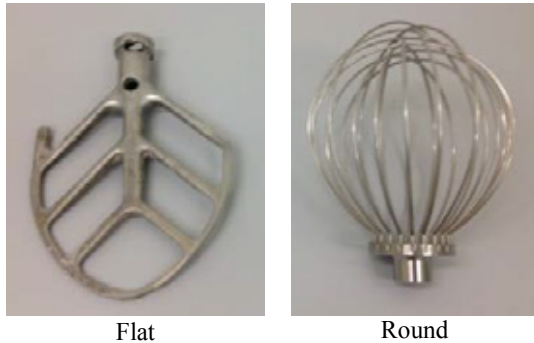
Flat   Round

Figure 1 – Two different types of blades employed in the Hobart mixing: (left) flat blade, standard used in EN-196; (right) round blade used occasionally to produce better mix

The new mixing setup was built in-house to introduce an intermediate mixing speed of ~2,000 rpm in the matrix system which has been identified as ideal for correlating matrix phase to the actual concrete [11]. The proposed design includes a handheld drill and an attached blade which was specially designed for mixing cements, in an effort to reduce air entrainment. The drill possessed a maximum rotation speed of 1,850 rpm. A container with dimensions presented in Figure 2 and a cap to ensure no spilling during the high shear mixing were also included. The setup was designed to possess an optimal setup with an intermediate external shear force in the order of low 10^3 rpm as discussed from literature and the statistical error from volume can be minimized while maintaining a homogeneous mixing of the paste. The new mixer setup was simple, user friendly, and is made up of commercially and affordable parts. Two different blades were also selected. The two blades are of similar sizes, whereby the steel blade possesses a diamter of 90 mm, whereas the plastic one was 85 mm. The main difference between these two blades lies in 3 main points: (1) air entraining effect, (2) scalability and (3) durability. In general, the steel blade allows less air entrainment and is more durable to wearing, whereas the plastic blade was described to be more apt for small scale mixing (up to 2~3l). The steel blade is described to be ideal for mixes of > 5l.
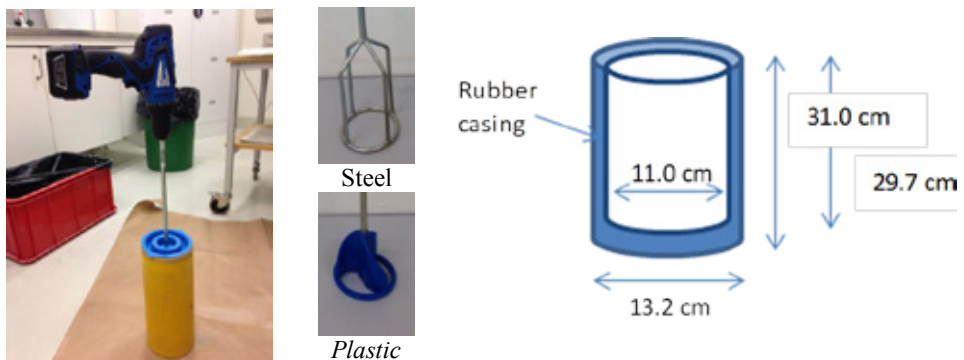

Steel

Plastic

Figure 2 (left to right) – Mixer setup; the two different blades employed in investigation and dimensions of mixing container (with lid, approximate volume = 2.8 l)

For simplicity, the blades employed in the different mixers are denoted as follow: Hobart mixer, round – (r) and flat – (f); Drill mixer, plastic – (p), steel – (s).

2.2 Mixing methods

The mixing procedure was similar for all three mixing setups to eliminate any variation due to mixing procedure, ensuring that the mixing setup (speed) is the sole reason for differences observed in the results. This mixing sequence was selected based on routine mixing procedure employed in the Velde AS laboratory. The choice of mixing method was to ensure familiarity in mixing to prevent and eliminate any additional errors which could arise. The method for mixing of the matrix is displayed in Table 2.

The sample was allowed to stand in the 3l flask between step 8 and 9 where properties of the matrix were measured. The mixture was given a light shake just before pouring into the flow cyl at step 9.

Table 2 – Preparation of mix for FlowCyl measurements

Step	Time		Procedure
	Total [min]	Each [min]	
Pre-mix (dry)			
1*	-3.0	2.0	All fillers and cements were premixed in a Hobart at speed 1(low). The standard flat blade was chosen.
2	-1.0	1.0	Water and admixtures were pre-mixed together in
Wet mixing			
3	0.5	0.5	Sample from step 1 added to step 2.
4	2.5	2.0	All materials were mixed at high speed
5	4.5	2.0	Left at rest
6	6.5	2.0	All materials were mixed at low speed
7	7.0	0.5	All materials were transferred into a 3L flask
8'	10.0		FlowCyl, rheometric and calorimetric measurements (1)
9'	30.0		FlowCyl, rheometric and calorimetric measurements (2)

*Step 1 is optional.
' FlowCyl measurements were performed exactly at the 10 minutes mark. For rheological and calorimetric measurements, these were started within 3 to 5 minutes after starting FlowCyl measurements.

2.3 Laboratory test methods

The parameters analysed can be divided into two categories. The first group of analysis consists of visual examinations. These observations were performed immediately after mixing of matrix by the different blenders. The parameters qualitatively determined are: air entrainment, temperature rise and degree of agglomeration of matrix. The purpose of identifying these qualitative properties is to give a quick and easy analysis of the matrix.

The second group comprises of quantitative measurements of flow resistance, viscosity and yield stress and hydration profiling. For this purpose, three different test methods were engaged

here. They include rheological measurements on a parallel plate rheometer and a flow cyl apparatus, followed by hydration profiling through isothermal calorimetric studies.

For rheological measurements in step 8 and 9 (10 and 30 minutes after wet mixing respectively), a flow cyl (base radius = 0.008 m; top radius = 0.08 m, height = 0.26 m) and a Physica MCR 300 (parallel plate rheometer with a gap size of 1 mm) were utilized. The degree of hydration of the matrix was observed via isothermal TAM Air calorimetry up to 12h of hydration. Detailed write-up of each investigation method is given as below:

FlowCyl measurements
The flow resistance ratio (λ_Q) is determined in the FlowCyl test [4], which is a modification of the Marsh Cone test. In general, λ_Q is defined as the difference in flow rate between the test material and an ideal fluid flowing through a vertical, cylindrical steel tube with an outlet formed as a cone ending in a narrow nozzle. An "ideal" fluid which is very liquid has a λ_Q-value of 0.0, while the theoretical upper limit of the λ_Q is 1.0 for a very viscous fluid. As an example, λ_Q of water is determined to be in the range of 0.10 to 0.15.

λ_Q of the matrix materials was determined in a simple FlowCyl setup as shown in Figure 3 (left). This setup is attached to a computer running the BalanceLink program (Mettler Toledo). Dimension wise, the FlowCyl apparatus consist of a cylinder tube with inner diameter of 80 mm and outlet 8 mm. The total length of the tube is 400 mm of which the cylindrical portion is 300 mm. It also possessed an outlet formed as a cone ending in a narrow nozzle and is represented in Figure 3 (right).
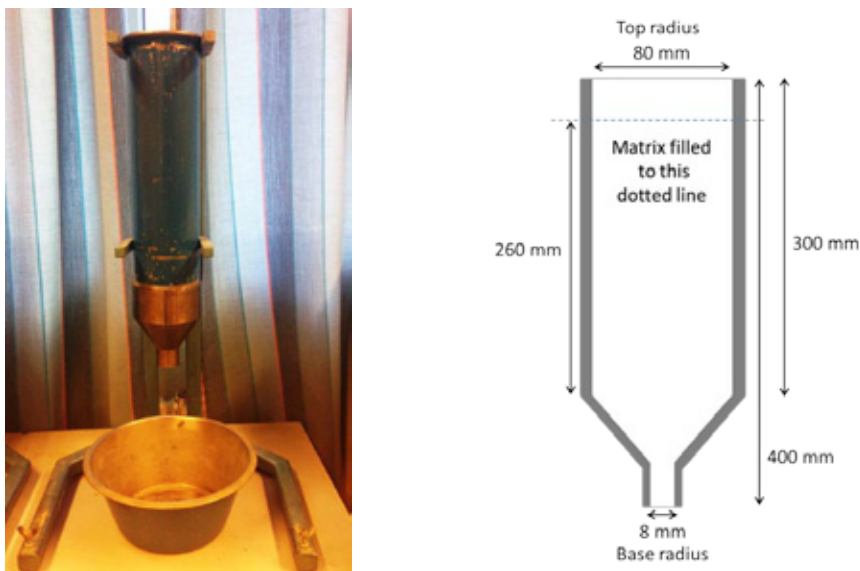

Figure 3 (left) Actual and (right) schematic drawing of FlowCyl cylinder tube

During the measurements, the cylinder is placed vertically in a rack and a steel bowl placed on an electronic scale connected to a computer is positioned directly under it. The weight of the matrix flowing into the bowl is recorded continuously at a sampling rate of 2s till the cylinder is

empty. The final results are processed based on time taken for the matrix to flow down the column, giving the λ_Q of the matrix.

Rheological measurements

A Physica MCR 300 rheometer (Anton Paar, Graz/Austria) equipped with a parallel plate geometry was utilised (Figure 4 (left)). The plates were aerated to increase the contact surface of paste with plates. After the paste was mixed for 10min, ~1.5g of the total (~4kg) was transferred to between the parallel plates before setting the gap space during the measurement at 1 mm. All measurements were conducted at 20°C and the paste was first homogenised for 30s at a shear rate of $100s^{-1}$. Thereafter, it was subjected to increase shear rate from 2 to $150s^{-1}$ over a period of 3min, followed by a step down of shearing from 150 to $2s^{-1}$ for a further 3min. The variations in shearing give rise to the corresponding shear stress of the paste, as represented by the up and down flow curves shown in Figure 4. The same test was repeated for paste at the 30min interval.
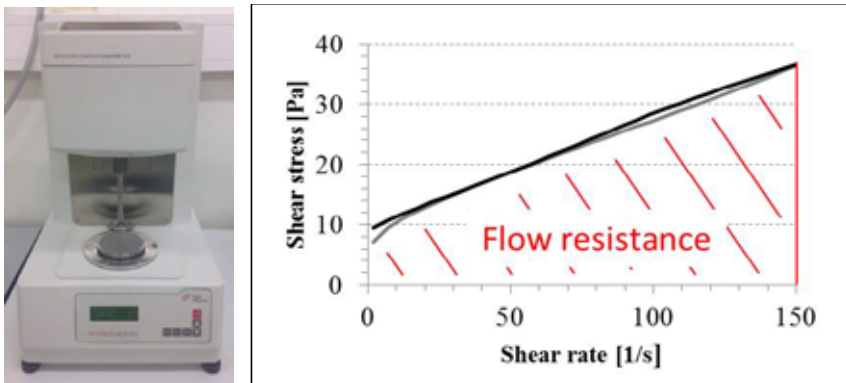

Figure 4 – (left) Physica MCR 300 rheometer with parallel plate attached (standby mode); (right) Flow curve of a matrix prepared according to recipe shown in Table 3. Sample was mixed with the Drill (steel) setup. Area under down curve represents the flow resistance.

The down flow curve obtained during measurements is fitted with a linear regression at the high shear rates ($> 30s^{-1}$).The Bingham viscosity (μ_2) can be obtained from the gradient of the fit, while the dynamic yield point (τ_d) of the cement slurry is determined from the y intercept of the linear regression line [13]. The flow resistance (FR_2) which is a measurement of the work done to shear the paste within the given range of shear rate is calculated from the area under the down curve.

Calorimetric measurements

All heat evolution measurements were performed for 12h. Samples were placed into the calorimeter after 10 and 30min of wet mixing to ascertain the independence on evolved heat to the point of measurement. ~8g of sample was used in each measurement. A scan rate of 2s per point of measurement was used.

2.4   Materials

For this investigation, three materials were used: cement, fillers sieved to obtain materials with a maximum particle size of 0.125mm, and superplasticizers. The cement was "Miljøsement" supplied from Cemex AS (Type I cement, Norway). It possessed a Blaine value of 470 m^2/kg and density of 3.08g/cm^3. The fillers were obtained from Velde AS (Sandnes, Norway) and possessed a D_{50} value of 24.9μm as determined by the sedigraph method. These fillers are prepared by crushing granite stones. The superplasticizer employed was a commercial product with trade name Dynamon SX–N. It was supplied from Mapei AS, Norway and is an acrylic based polymer commonly used in ready-mix concretes in Norway. All three materials were used as per obtained.

The materials were prepared according to the recipe as given in Table 3 for all mixing tests. This was based on a simplified recipe for M60 (S class) concretes, where only the matrix was tested.

Table 3 – Formulation recipe employed in current investigation

Materials	Amount [g]
Miljø cement	1800
Water	1062
Velde fines (< 0.125 μm)	1020
SP (Rescon SXN FG = 18 %)	0.50
w/c	0.59
filler/cement	0.51

3   RESULTS AND DISCUSSION

3.1. First observations immediately after mixing

The first observations based on quick qualitative analysis of the matrix immediately after mixing include (1) change in temperature, (2) visual analysis of air contents and (3) visual analysis of the dispersion of the pastes. The results are summarized in Table 4. As can be seen, mixer setup 1 to 3 showed immediate flaws in the paste obtained. When the Waring blender was utilized, due to the high rotating speed, rapid temperature rise was observed. As mentioned in ASTM C1728-1, the temperature of the matrix should be kept similar to before mixing. Therefore, such a rapid increase in the temperature of matrix mixed in the non-insulated Waring blender rendered it less ideal as a mixer when used alone for the purpose of producing matrix with rheological properties which can correlate to that of concretes. Maintaining an isothermal condition with the Waring blender will however increase its price by ~10 times. The high air entrainment can be attributed to the vortex rotating effect of the blades.

In the case of Hobart, depending on the type of mixing blade employed, low amounts of dispersion (flat) and entrainment of air bubbles (round) were observed. This could effectively be attributed to the low speed of mixing, thus causing inhomogeneity during mixing with the flat blade. On the other hand, when the round blade was employed, the rapid twirling of the metal pieces generated and captured air bubbles within the paste. With the drill mixer which possessed an intermediate mixing speed, no significant rise in temperature or any air bubbles were detected. The pastes prepared with this new mixer also appeared well dispersed.

Table 4 – Observation of the samples mixed in different mixer setups

No.	Mixer	Blade	Observation Temperature rise	Air	Disperse
1	Waring	-	yes	yes*	yes
2^	Hobart	Flat	no	no	no
3	Hobart	Round	no	yes	yes
4	Drill	Steel	no	no	yes
5	Drill	Plastic	no	no	yes

*Air entrained in pastes prepared with Waring blender much more than that from Hobart (round)
^Lumps observed in paste even after mixing, and samples lost due to splashing during mixing

3.2. Flow properties of the pastes

Rheological properties of the pastes were determined via FlowCyl and rheometric measurements at 10 and 30min after the start of wet mixing. Figure 5 displays the flow resistance of the pastes prepared using different mixing setups as measured by FlowCyl test. It can be clearly observed that the flow resistance varied for different mixers and the lowest flow resistance (independent of the time) was observed when the drill mixer was utilized. The high flow resistance from pastes produced from the Hobart mixer can be attributed to the lower dispersing ability of this setup, where presence of agglomerates and lumps greatly decreased the overall flow of the paste. In general, mixing at low speed was more detrimental to the flowability of the pastes than high speed.
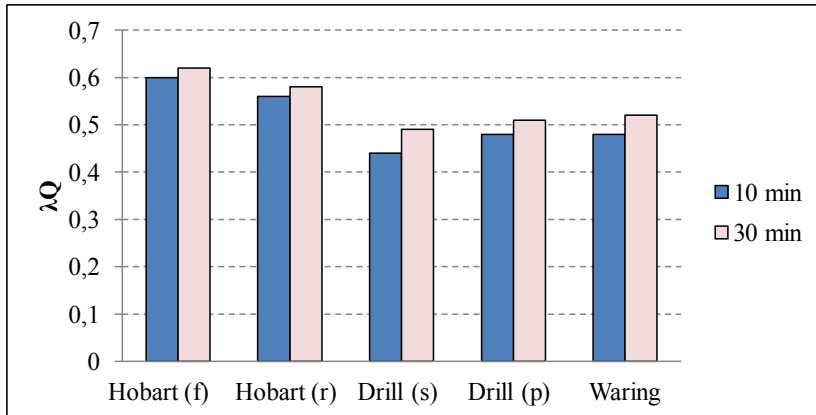

Figure 5 – Flow resistance (λ_Q) of pastes prepared by different mixing methods measured by Flow cyl at time intervals of 10 and 30 min respectively

The shear viscosities and dynamic yield stresses of the pastes prepared by different mixing methods can be observed in Table 5. The pastes prepared with Hobart mixer (regardless of blade type) produced the highest plastic viscosity. The λ_Q as measured in the FlowCyl test is dominated by the plastic viscosity. The Waring blender increases the dynamic yield stress significantly, which has a secondary effect on the flow resistance in the FlowCyl test. The increase in yield stress may be correlated to cement particle crushing, early hydration or other effects. It can be concluded that shear viscosity had a higher impact on the flow resistance of the paste (from the flow cyl) as compared to the dynamic yield stress.

Table 5 – Shear viscosity (μ) and dynamic yield stress (τ) of the pastes at 10 and 30 min

	μ_{10}	μ_{30}	τ_{10}	τ_{30}
	[Pas]	[Pas]	[Pa]	[Pa]
Hobart (f)	0.30	0.29	10.3	10.1
Hobart (r)	0.26	0.25	6.2	5.8
Drill (s)	0.16	0.17	10.2	9.8
Drill (p)	0.19	0.19	9.5	9.1
Waring	0.14	0.14	38.4	36.7

Comparing the yield stress of matrix produced by different mixers, Waring blender showed the highest values which was at least ~4 times higher than the next sample (Hobart (f) with a τ_{10} = 10.1Pa), indicating that the slump flow of this paste is much lower compared to the other mixing methods. This high deviation signifies that matrix produced with this mixing procedure is not as ideal, especially in the case of SCC formulations.

Figure 6 displays the rheometric flow resistance of the pastes measured by rheometer at 10 and 30min respectively. It can be distinctively observed that in the same way, samples prepared using the drill (steel) setup possessed the lowest flow resistance, and this flowability was maintained up to 30min. Samples prepared using the Hobart mixer had a moderate flow resistance due to the pre-dispersing effect from the initial shearing of the paste in the rheometer. The sample prepared with Waring blender displayed the highest flow resistance, clearly related to the significantly higher yield stress.
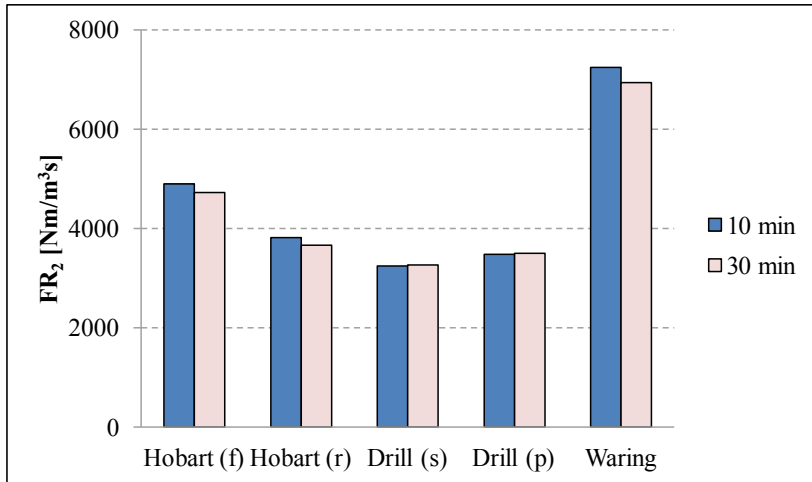

Figure 6 – Flow resistance of pastes prepared by different mixing methods measured by Physica MCR 300 rheometer at time intervals of 10 and 30 min respectively

The main difference between FlowCyl and rheological measurements was the condition under which measurements were conducted. In the case of FlowCyl, the flow of paste was measured after paste was allowed to stand and was measured under the effect of acceleration due to gravity. In the rheometer, a constant force was exerted on the paste over a range of shear rate (2–150 s^{-1}). With such a high shear in the latter method, the agglomerates that were initially present in the pastes prepared with Hobart will be dispersed, resulting in a seemingly lower flow

resistance. On the other hand, in the case of Waring blender, the high flow resistance can be potentially attributed to the increased in hydrate phases formed as a result of the increase in temperature. In general, λ_Q from FlowCyl test can be correlated to the Bingham viscosity of the matrix, whereas FR_2 from rheological measurements with the parallel plates is defined by the dynamic yield stress (slump flow).

3.3   Hydration behaviour of the pastes

Isothermal calorimetric analysis was performed on all the samples. The samples were introduced into the calorimeter at 10min after water addition, corresponding to the first measurement by FlowCyl and rheometer. For analysis, both the initial heat rates of pastes up to 30 minutes of hydration and the accumulated heat evolved up to 12h were recorded.

The initial heat rate of pastes up to 30 minutes after water was first added is shown in Figure 7. In general, mixing greatly affected the gain in heat of cement pastes right from the onset of hydration. The initial heat rates of the samples can be correlated to the rise in temperature as observed in section 3.1. The paste prepared with the Waring blender showed the highest deviation in heat rate, indicating the highest degree of crushed cement particles among all the pastes prepared. The heat rates of the other four pastes, on the other hand were less than half of that of the former, whereby paste prepared with the drill (s) registered the highest heat rate, followed by drill (p), Hobart (f) and Hobart (r) respectively. Relative to paste prepared with Waring, these four pastes displayed similar heat rates (Figure 7), indicating that the increase in shear speed from the drill mix did not influence hydration of matrix significantly. The distinctive difference in heat rate of pastes prepared from Waring from the other four indicated an increase in hydration of the sample, thus accounting for its higher flow resistance.
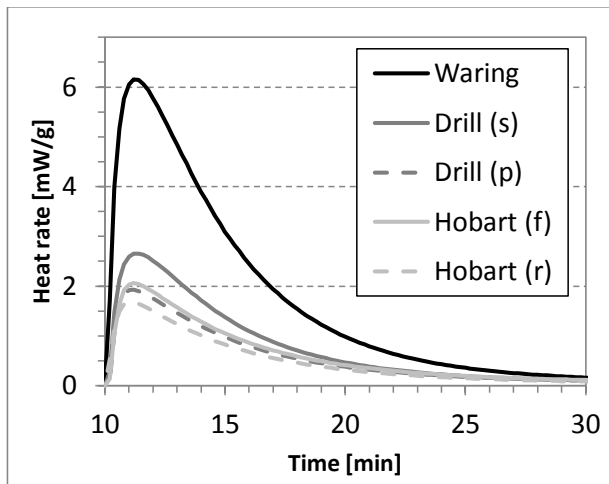

Figure 7 – Rate of heat evolution of pastes introduced into the calorimeter after 10min of mixing prepared with the Waring blender, Drill (steel), Drill (plastic), Hobart (flat), Hobart (round) mixers respectively

The accumulated heat of pastes hydrated up to 12h further confirmed this. As observed in Figure 8, the main variation lies in the fact that at 1h after water addition, pastes prepared with the

Waring blender displayed a much higher accumulated heat (6.5J/g by 12h) than the others (~4.3J/g by 12h). When the Waring blender was utilized, the early acceleration of the heat rates (Figure 6) shortened the induction period, leading to a hastening in the hydration of silicate phase, thus increased flow resistance of the pastes. It is of interest to note that acceleration of the silicate hydration only occurred when mixing speed was in the order of 10^4 rpm (Waring). On the other hand, only a small variation in hydration rates was detected when shear was varied from 10^2 rpm (Hobart) to low 10^3 rpm (drill). In such a situation, the higher flow resistance of pastes prepared with Hobart can thus be attributed to the air entraining and agglomeration of the matrix during mixing.

Another observation from Figure 8 is the similarity in the rate of heat evolved after 30min. For all pastes, the rate of heat evolved was similar, thus indicating no variation in their hydration mechanism despite the variation in temperature and degree of hydration.
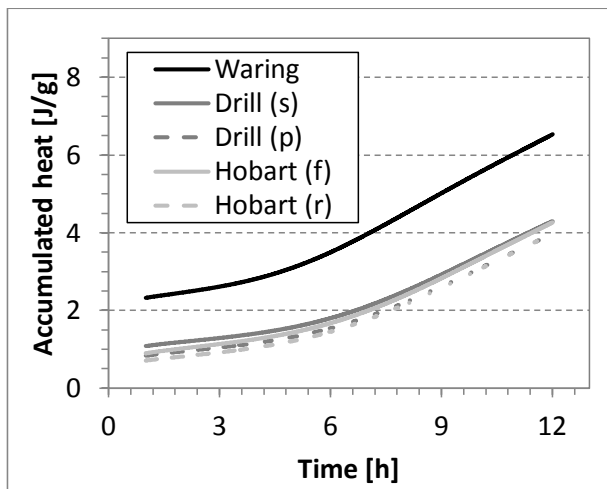

Figure 8 – Heat evolution of pastes introduced into the calorimeter at 10min interval after wetting prepared by different mixing methods

To better comprehend the flow resistance of the pastes, the heat rates of pastes prepared with the Hobart (round) and Waring placed into calorimeter after 10 and 30min were compared (Figure 9). For both pastes, a drop in the heat rate was observed when samples were placed later in the calorimeter at 30min. This can be attributed to the dissipation of heat from the pastes to the surrounding, thus accounting for the slight decrease in flow resistance as measured in the rheometer. It can further be observed that heat dissipation is greater for pastes prepared with Waring than Hobart, due to the higher temperature gradient between surrounding and paste of the former.
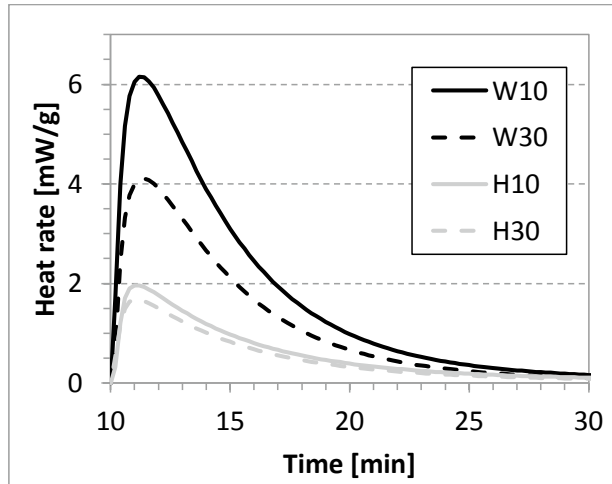
Figure 9 – Comparison of heat registered by calorimeter from paste prepared at 10 and 30min (W and H represents sample prepared by Waring and Hobart respectively, whereas 10 and 30 refer to the time interval after mixing before introducing sample into calorimeter)

4   CONCLUSION

When analysing the workability of matrix, it is important to maintain a good correlation between the actual shear in the concrete mix and that employed during investigation of the matrix system. Many parameters govern the influence of mixing on the workability of matrix, but two main factors are non-excessive temperature rise and air entrainment. The current state of art demonstrated that a moderate speed of $\sim 10^2$ rpm in the mixing of matrix is required for the good correlation to exist. Current mixing methods do exist, however, at a much higher cost which is generally unaffordable for routine work in small scale laboratories.

Here, we successfully present a new mixing setup which possess the desired mixing speed range of ~1850rpm, while at the same time is very affordable at a low price of ~3000NOK. The mixer is a simple drill setup fixed with a steel blade in an enclosed tube, making it also very user friendly. Mixing with this setup produced matrix with low or no air bubbles at all (as observed by naked eyes), stable temperature throughout mixing and the little effect it has on the overall hydration of the matrix. Due to these factors, the pastes prepared with the drill (setup) mixer showed the lowest flow resistance and was ideally the best setup up for mixing matrixes for better correlation to actual concrete systems.

In general, the mixer is designed to be applicable to a wider range of matrix, with variations type and amounts in the different components (fillers, superplasticizers dosage and type, etc). Therefore, as a next step, large scale testing will be performed utilizing this mixer setup on different matrixes. Thereafter, a correlation with the actual concrete systems will be done by conducting concrete tests.

ACKNOWLEDGEMENT

REFERENCES

[1]   *Helmuth, R.A.*, "Structure and rheology of fresh cement paste," in: Proc 7th International Congress on Chemistry of Cement, Paris, Vol. I.0, No. 16, 1980, pp. 16–30.

[2]   *Ferraris, C.F., Gaidis, J.M.*, "Connection between Rheology of Concrete and Rheology of Cement Paste," ACI Materials Journal, Vol. 88, No. 4, 1992, pp. 388–393.

[3]   *Tattersall, G.H., Banfill, P.F.G.*, "The Rheology of Fresh Concrete," Pitman Advanced Publishing, Boston, 1983.

[4]   *Mørtsell, E. Maage, M., Smeplass, S,* "A Particle Matrix Model for Prediction of Workability of Concrete," In Proceedings of the International Conference on Production Methods and Workability of Fresh Concrete. Glasgow, Scotland 1995.

[5]   *Smeplass, S. and Mørtsell, E.*, "The Particle Matrix Model Applied on SCC," In Proceedings of the Second International Symposium on Self-Compacting Concrete, Tokyo, Japan, 2001.

[6]   Mørtsell E., Modelling the effect of concrete part materials on concrete consistency, Dr.ing Dissertation 1996:12 Norw.Univ.Sc.&Tech (1996) 310 p. (In Norw.)

[7]   *Powers T.C.*, "Properties of Fresh Concrete," Wiley, New York, 1968.

[8]   *Juilland,* P*., Kumar, A., Gallucci, E., Flatt, R.J., Scrivener, K.L.*, "Effect of mixing on the early hydration of alite and OPC systems," Cement and Concrete Research, Vol. 42, 2012, pp. 1175–1188.

[9]   *Ferraris, C.F.*, "Concrete Mixing Methods and Concrete Mixers: State of the Art," Journal of Research of the National Institute of Standards and Technology, Vol. 106, No. 2, 2001, pp. 391–399.

[10]   *Tang, F.J., Bhattacharja, S.*, "Development of an early stiffening test," Report RP46, Portland Cement Association, Skokie, IL, 1997.

[11]   *Williams, D.A., Saak, A.W., Jennings, H.M.,* "The influence of mixing on the rheology of fresh cement paste", Cement and Concrete Research, Vol. 29, 1999, pp. 1491–1496.

[12]   ASTM C1738-11, Standard Practice for High-shear mixing of hydraulic Cement pastes

[13]   Mezger, T.G., "The Rheology Handbook: For users of rotational and oscillatory rheometers", Ed. Ulrich Zoll, Hannoprint, 2002. ISBN: 3-87870-745-2

The Development of an Experimental Program through Design of Experiments and FEM Analysis: A Preliminary Study
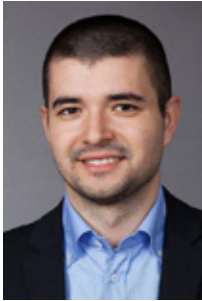
Cosmin Popescu
M.Sc., Ph.D. Student
NORUT, Rombaksveien E-6 47, N-8517 Narvik, Norway
Department of Infrastructure Structures and Materials
E-mail: cosmin.popescu@norut.no

Gabriel Sas
Ph.D., Assistant Lecturer
Luleå University of Technology, Department of Structural Engineering
SE – 971 87 Luleå, Sweden
E-mail: gabriel.sas@ltu.se
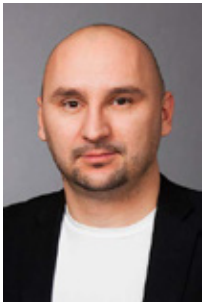
ABSTRACT

This paper presents an experimental test setup which allows investigation of the structural behaviour for axially loaded concrete walls with openings. The test matrix was developed with the help of design of experiments technique. A two-level factorial experiment has been designed resulting in a total of nine wall specimens. Previous research has shown that the ultimate capacity of concrete walls is dependent on the boundary conditions. Therefore, a new test-rig was proposed and designed to work according to the imposed conditions. Nonlinear simulations calibrated on a previous experimental program were used to obtain the reaction forces.

Key words: Concrete walls, openings, design of experiments, FEM, strengthening, test setup

1.   INTRODUCTION

In Europe the majority of concrete structures were built before 1970 [1]. These structures are continuously degrading and the need of repair increases exponentially. This increase is closely connected to worldwide population growth, so that new structures are being built and existing structures still need to be used. Replacement is a typical solution for old structures or structures that do not fulfil anymore their intended purpose, however this process requires extended financial effort and is not environmentally friendly.

The following are the main reasons for the need of repair, rehabilitation and strengthening of existing RC structures:

- New design standards are imposed so that the demands of the society regarding structural safety, exploitation and aesthetics can be accommodated
- Changes in use or imposed loading
- Structures are continuously ageing due to material degradation and external environment
- Construction errors are still encountered due to human error

- Conscious human intervention to provide new functionality to a structure requires removing structural elements or creating new openings
- Special events such as accidental explosions and natural disasters

The current project deals with the common situation when new openings are required in existing reinforced concrete (RC) walls due to changing the functionality of the building. In recent years there has been increasing interest in creating large spaces by connecting adjacent rooms through a newly created opening in an existing solid wall. The creation of these openings in walls will change the stress distribution and adversely influence the behaviour of the wall, [2, 3], thus a strengthening of the structure is imposed to recover the initial structural capacity.

There are two traditional methods for strengthening RC walls with openings: (1) creating a frame around the opening using RC/steel frame systems, and (2) increasing the cross section thickness. These methods will increase the weight of the strengthened elements and may create major discomfort by drastically limiting the use of structure during repairs. A better alternative is the use of fiber reinforced polymers (FRP) as externally bonded reinforcement, method that has received worldwide acceptance during the last two decades [4, 5]. This technique implies that thin sheets or plates are bonded to the surface of the structure through an adhesive, so that a composite material is formed. Successful applications of FRP to strengthen openings in structural elements were achieved by several researchers [3, 6, 7].

The research performed on RC walls with openings [8-11] focused on elements designed as if the opening has been initially planned, whereas RC wall panels with cut-out openings is still unexplored. The case when axially loaded RC walls are strengthened by FRP components is still at an incipient level; to the best knowledge of the authors only one study, [3], was performed so far. Mohammed et al. [3] found that the presence of the opening in a solid one-way panel lead to disturbance zones. The discontinuities causing high stresses will force the cracks firstly occur at the corners due to insufficient internal reinforcement. It was concluded that applying FRP around the opening in different patterns, the capacity could be improved by reducing the principal stresses acting on the upper corners of the opening.

A research program is undergoing at Luleå University of Technology where a number of concrete walls with different parameters will be tested. This paper presents the process of defining an experimental program able to describe the structural behaviour of FRP-strengthened walls with cut-out openings. The experimental research found in the available literature was carried out on limited number of tests using customized test-setups because of lack of standardized procedures for testing walls and walls with openings. Therefore, the aim of this study is to investigate how an experimental program can be defined comprehensively using statistical tools and numerical modelling. The type of elements and test procedure, are identical with the ones studied by Lee [12].

The following two objectives were set: (1) determine the number of the specimens to be tested using design of experiments (DOE) technique and (2) propose a new test-rig for laboratory testing based on an accurate finite element modelling (FEM) and comparison with experimental results presented by Lee [12].

2.   DESIGN OF EXPERIMENTS

2.1   Theory

A methodology for designing experiments was first proposed by Fischer [13] and is referred in the literature as design of experiments (DOE). The method uses statistical tools to analyse data and predict the system performance [14]. DeCoursey [15] showed that one-factor-at-a-time design would not give precise information about the interaction, and the results from that plan of experimentation might be misleading. Thus, a better alternative is to conduct tests by combining different levels of the factors, which is called a factorial design. By choosing a number of parameters and a fixed number of levels, experiments should be performed with all possible combinations. The entire process for a successful design of experiments is shown in Figure 1.
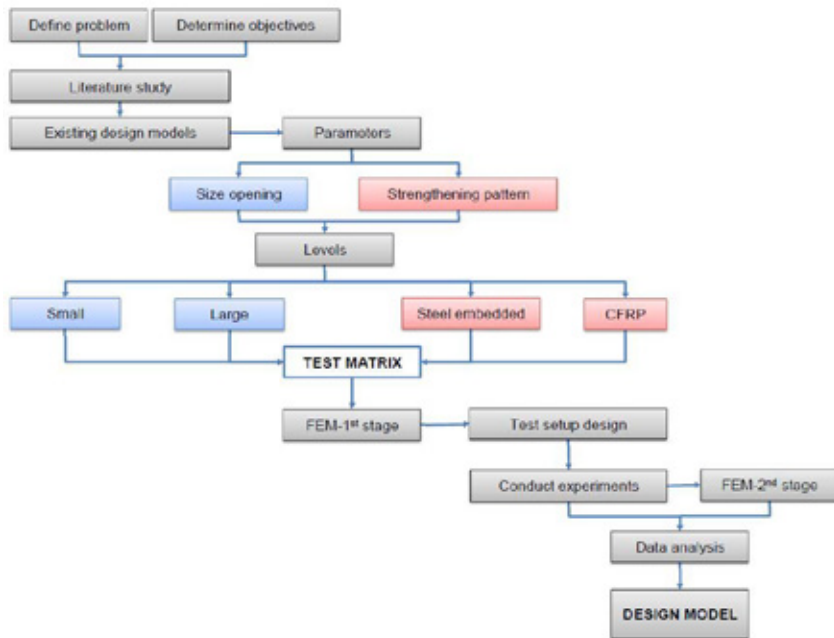

Figure 1 – Development of a design of experiment application

2.2   Proposed experimental program

The parameters that can have a high influence on the axial load capacity of RC walls with openings were identified by studying different models available in the literature. Several models for predicting the axial capacity of RC walls with openings were identified. Among these, the latest formula (Eq. 1) proposed by Doh and Fragomeni [8] was found to give satisfactory results [16]. In equation (1), N_u represents the axial capacity of an identical panel without openings, k_1 and k_2 are constants derived using a standard regression analysis and the factor χ incorporate the effect of the size and location of the opening in the wall.

$$N_{uo} = (k_1 - k_2\chi) N_u \tag{1}$$

Parameters like eccentricity, side supports, slenderness, aspect ratio and reinforcement ratio have also influence on the ultimate axial strength of a solid RC wall. These parameters have been studied in the past [17-20], thus being out of scope for this experimental program. According to the theory behind factorial design, past experience should contribute in choosing the right parameters to be varied at maximum of two levels. Based on the results from the first stage of experiments (see Figure 1), further tests can be designed logically and may well involve more than two levels for some parameters. Box et al. [21] introduced "the 25% rule" in which not more than one quarter of the budget should be spent in an initial design. Based on the first observations one can run countless experiments for different levels by using computer modelling.

The first set of analyses examines the impact of two parameters: (1) openings size and (2) strengthening pattern. For the first parameter small (S) and large (L) opening will be set as the min/max level and for the second one: (a) steel reinforcement bars embedded into concrete and placed around corners at 45° as it has been initially designed (st) and (b) externally bonded (EB) and near surface mounted (NSM) FRP reinforcement (frp). Consequently, this will require 2^2 different experiments for a complete factorial design. The two levels of these two parameters are presented in Table 1. Besides these tests another three specimens (i.e. wall with and without cut-out openings) used as references will be tested until failure to assess the effectiveness of strengthening alternative. An important factor in experiments, namely replication, would be kept at low level since large elements like walls involve many resources. That means only two identical specimens from those strengthened with FRP will be cast and for the rest of them only one specimen. The tests designed based on the DOE technique are shown in Figure 2.

Table 1 – Level of parameters

Designation	1st parameter [*opening size*]	2nd parameter [*strengthening pattern*]	Description	No. of tests
WSO-st	S	St	Small opening strengthened with steel reinforcement	1
WSO-frp	S	Frp	Small opening strengthened with FRP	2
WLO-st	L	St	Large opening strengthened with steel reinforcement	1
WLO-frp	L	Frp	Large opening strengthened with FRP	2
WSO	S	-	Weakened by small opening	1
WLO	L	-	Weakened by large opening	1
RCW	-	-	Solid slab (without opening)	1

Nine half scale specimens L=1800 mm (length), H=1350 mm (height) and t=60 mm (thickness) resulted from this plan of experimentation having an aspect ratio (H/L), slenderness ratio (H/t) and thickness ratio (L/t) of 0.75, 22.5 and 30, respectively. The cut-outs will represent a door opening centrally placed with 450x1050 mm and 900x1050 mm dimensions for small and large opening, respectively. A concrete with a maximum aggregate size of 16 mm and a C25/30 concrete strength class is used to cast the specimens. The walls are regarded as plain concrete walls in EN 1992-1-1 [22], however, a minimum amount of steel reinforcement are used for durability purposes and to avoid cracks due to creep and shrinkage. The steel ratio was set to 0.3% centrally placed in one layer. An amount of reinforcement equivalent to that interrupted by an opening has to be added at 45° around corners for those elements intended to be strengthened with embedded steel reinforcement. For specimens FRP-strengthened, NSM bars at 45° will be mounted around corners and EBR sheets surrounding the cut-out opening.
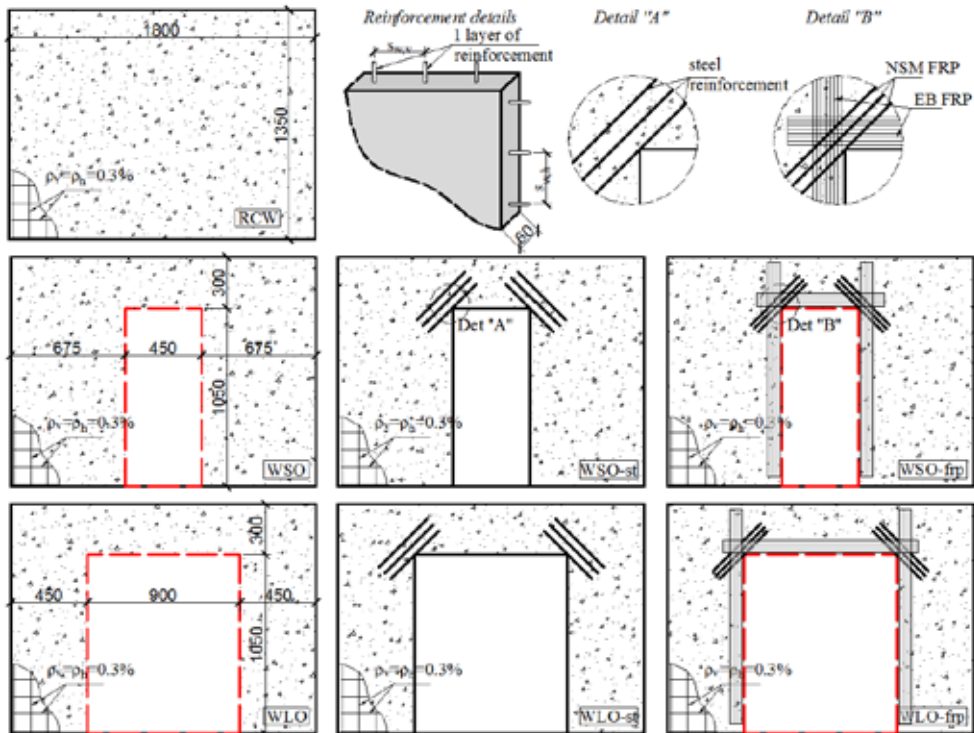
Figure 2 – Details of the specimens

Finally, as soon as the data from the experiments is collected, statistical techniques are used to analyse the data. With the use of computer programs, e.g. MiniTab. [23], the interaction between different parameters and the level for which a parameter plays a significant role could be determined. Moreover, the software is able to plot a model equation that can describe the response of the system.

3.   BENCHMARK STUDY

3.1   Summary of the tests performed by Lee [12]

Lee [12] preformed an experimental study on the behaviour of RC walls with openings. The study consisted of forty seven half-scale panels tested in one-way and two-way action. The tested walls had different opening configurations and slenderness ratios and subjected to a uniformly distributed load acting with an eccentricity of one sixth of the wall thickness. The specimens were loaded in increments of 14.7 kN until failure. Ultimate load, deflections and crack pattern were recorded and will be used to compare them with results from the numerical analysis.

Two wall specimens were chosen to be modelled and calibrate the FE-model against them. The window-type openings were symmetrically placed in both one-way (O45W1C1.4) and two-way

(T45W1C1.4) action walls. The wall specimens were reinforced with a single layer of steel bars centrally placed, satisfying the minimum requirements in the AS3600 [24]. The vertical and horizontal reinforcement ratios, ρ_v and ρ_h, were 0.31% with the minimum tensile strength of 500 MPa. To prevent early cracking around openings, three diagonal bars were placed in each corner. The average concrete compressive strengths, f_{cm}, have been determined based on concrete cylinder tests. For O45W1C1.4 wall, the average compressive strength was 32 MPa while for T45W1C1.4 the average compressive strength was 45.5 MPa, determined at day of testing.

The general dimensions of the wall specimen and reinforcement layout are shown Figure 3a. The thickness of the tested element was 40 mm thus, the specimen having both slenderness and thickness ratio equal to 35. These dimensions are identical for both walls, the only difference being in the support conditions, i.e. fixed on two opposite sides (one-way) or on all sides (two way).
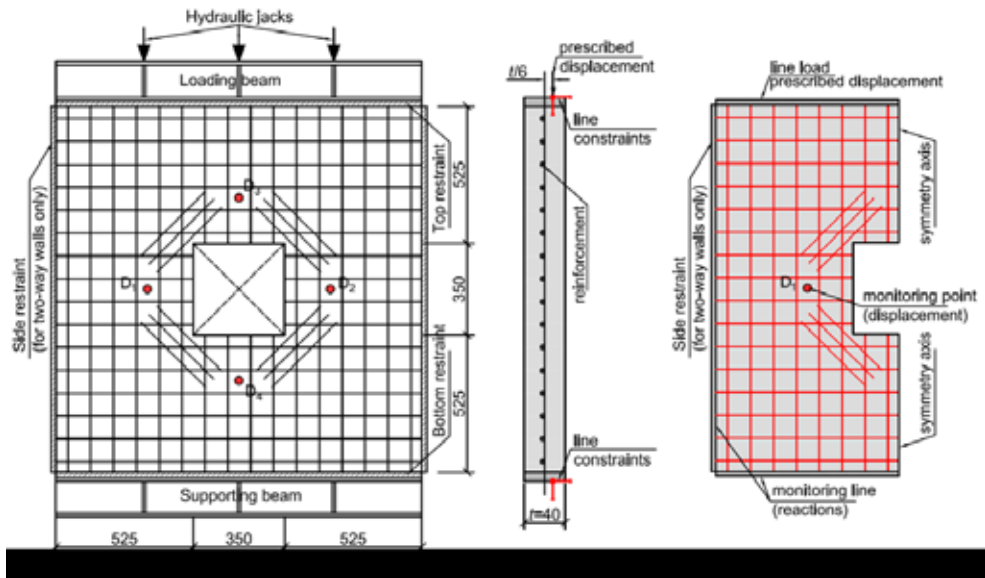

Figure 3 – Details of the test specimen: a) test setup adapted from Lee [12] and b) simplified numerical model

3.2   FE – model

A three-dimensional nonlinear FE-model has been created using ATENA-Science [25] software in order to capture the behaviour of axially loaded RC walls. An iterative solution procedure based on the Newton-Raphson method was adopted in the FEM simulation.

3.3 Material's constitutive laws

Concrete
The material-model used is a fracture-plastic model that combines constitutive models for tensile (fracture) and compressive behaviour (plastic) [26]. Orthotropic smeared crack model based on Rankine tensile criterion is used for concrete cracking while for concrete crushing the yield surface proposed by Menetrey and Willam [27] was employed. The fracture and plastic models are combined together using the strain decomposition method first introduced by De Borst [28] through a return mapping algorithm. The response of the un-cracked material is assumed to be linear-elastic up to peak values of stress in tension, f_t, with E_c the initial elastic modulus of concrete. At this state, the corresponding strain is $\varepsilon_0 = f_t / E_c$. After the tension strength was reached, the stress-strain law of concrete in tension follows a descending branch known as tension softening. The tension softening curve drop exponentially to zero if no tension stiffening effects would be considered, as it is considered in the present case-study.

The tension after cracking is represented by a fictitious crack model based on a crack-opening law and fracture energy in combination with the crack band approach (Figure 4). In the present study fixed crack model was chosen although the software offers the choice of rotated crack model also. The function of crack opening was proposed by Reinhardt et al. [29] and given by Eq. 2:

$$\sigma_t = f_t \left\{ \left[1 + \left(c_1 \frac{w}{w_c} \right)^3 \right] \exp\left(-c_2 \frac{w}{w_c} \right) - \frac{w}{w_c} \left(1 + c_1^3 \right) \exp\left(-c_2 \right) \right\} \tag{2}$$

where, w is the crack opening, w_c is the crack opening at the complete release of stress, σ is the normal stress in the crack, $c_1=3$ and $c_2=6.93$ are material constants valid for normal-weight concrete.
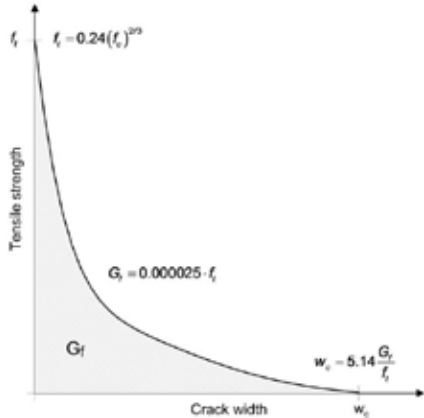

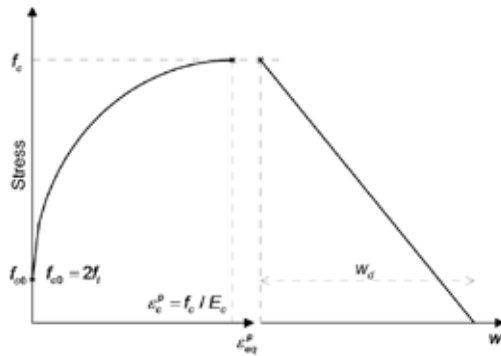*Figure 4 – Exponential crack opening law*

Figure 5 – Hardening/softening laws for concrete in compression

The shape function of the concrete in compression is based on work of van Mier [30]. The hardening law for concrete in compression is elliptical (Eq. 3) and based on strains. The softening law in compression is linearly descending with the end point of the curve defined by

means of the plastic displacement w_d, to avoid mesh dependency. The plastic displacement was set to $w_d=0.5mm$ as suggested from experiments of van Mier [30].

$$\sigma_c = f_{c0} + (f_c - f_{c0})\sqrt{1 - \left(\frac{\varepsilon_c - \varepsilon_c^p}{\varepsilon_c}\right)^2} \tag{3}$$

where, f_{c0} is the onset of nonlinear behaviour, f_c is the compressive strength of concrete, ε_c^p is the plastic strain at compressive strength.

The constitutive model for concrete requires as input important data such as the modulus of elasticity E_c, the tensile strength f_t, and fracture energy G_f. The values from Table 2, evaluated based on the average compression strength f_{cm}, were used in the numerical analysis.

Table 2 – Properties of the concrete material used in FEM analysis

Parameter	Equation	Reference
Elastic modulus [MPa]	$E_c = (6000 - 15.5 f_c)\sqrt{f_c}$	[31]
Tensile strength [MPa]	$f_t = 0.24 f_c^{2/3}$	[31]
Fracture energy (MN/m)	$G_f = 0.000025 f_t$	[32]

Reinforcement
The reinforcement was modelled as discrete bars using 2D isoparametric truss elements perfectly bonded to the concrete body. The elastic-perfectly plastic (i.e without hardening) behaviour was considered in the analysis with a default value for steel elasticity modulus of $E_s = 200$ GPa.

3.4   Geometry and boundary conditions

To take advantage of the symmetry of the walls and save processing time, only one half of each model was modelled as shown in Figure 3b. In order to avoid numerical problems due to high stresses concentrations, linear elastic steel plates were added to the model between element edges and the loading points. The load was applied as imposed deformations along the top of the specimens to assure a uniformly distributed load. A load eccentricity of $t/6$ that would cause an out-of-plane deflection of the wall was included in the analysis.

Displacements were monitored at the same locations where the LVDTs were installed on the tested walls. The ultimate capacity of the specimen was computed by monitoring the line reactions at the bottom of the specimen.

3.5   Element size and mesh sensitivity analysis

Different element types were investigated in order to find suitable elements to simulate the behaviour of slender RC walls with openings. ATENA software offers the possibility to model this problem using shell or solid elements. The concrete element was modelled by 8-nodes brick elements. A mesh sensitivity analysis was undertaken on the control specimens for three different sizes of the finite element per thickness, i.e. 15 mm, 10 mm and 5 mm, respectively.

The element size considered was 10 mm since it provided good results in terms of accuracy and computational time.

4.   FE – MODEL VALIDATION

The experimental and numerical load–displacement responses are compared to validate the accuracy of the model proposed and are shown in Figure 6. The ratio between ultimate capacity of experimental and numerical analysis are also shown in Figure 6. Moreover, the crack pattern and the failure mode observed in tests were compared with the one obtained from FEM and shows a good correlation as can be seen from Figure 7 and Figure 8.
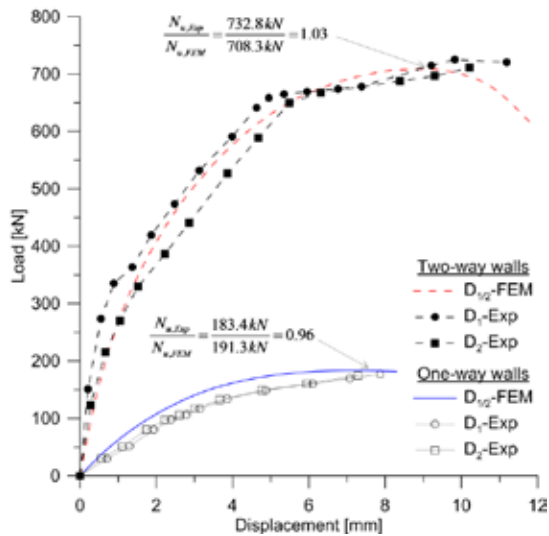

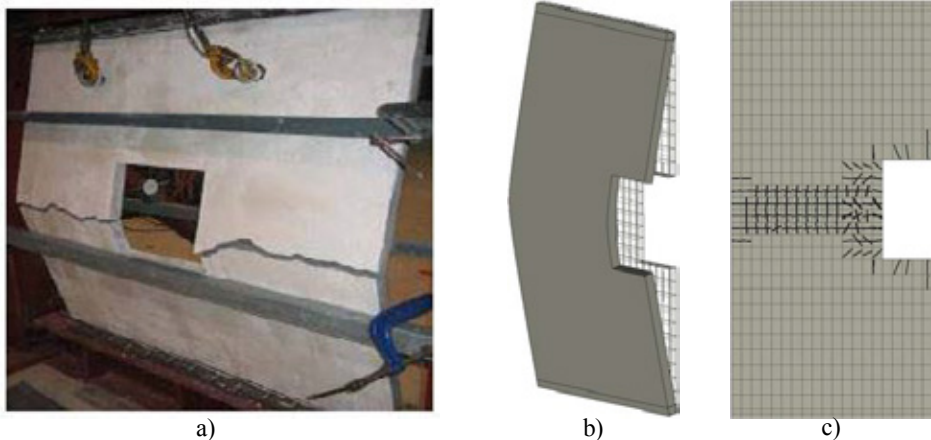*Figure 6 – Load-displacement response: experimental vs. FEM*

Figure 7 – Crack pattern and failure mode for one-way walls: a) experimental [12]; b) deformed shape - FEM; c) crack pattern - FEM

5.   TEST-RIG DESIGN FOR RC WALLS

5.1   Design principles

In practice, the gravitationally loaded walls behave under one-way or two-way action. Walls restrained along top and bottom edges of the wall are denoted as one-way action panels. These panels are developing a single out-of-plane curvature parallel with the load direction and are usually encountered in prefabricated tilt-up concrete structures. Panels restrained along three or all sides are denoted as two-way action panels. The walls in this case deflect in double curvature, in both horizontal and vertical directions, and are usually encountered in monolithic concrete structures. Since the two-way walls are the most encountered in practice and are studied to the same extent as one-way walls, in this study was decided to go further and develop a test-rig who can replicate the boundary conditions met in reality for this kind of walls.

The following assumptions were used for designing the test-rig:

(a) the test-rig has to simulate hinged connections at the boundaries of the specimen;
(b) sufficient rigidity of the lateral edges is needed to prevent any out-of-plane deformations;
(c) the walls are loaded gravitationally with a small eccentricity (one sixth of the wall thickness) to simulate the effect of imperfections;
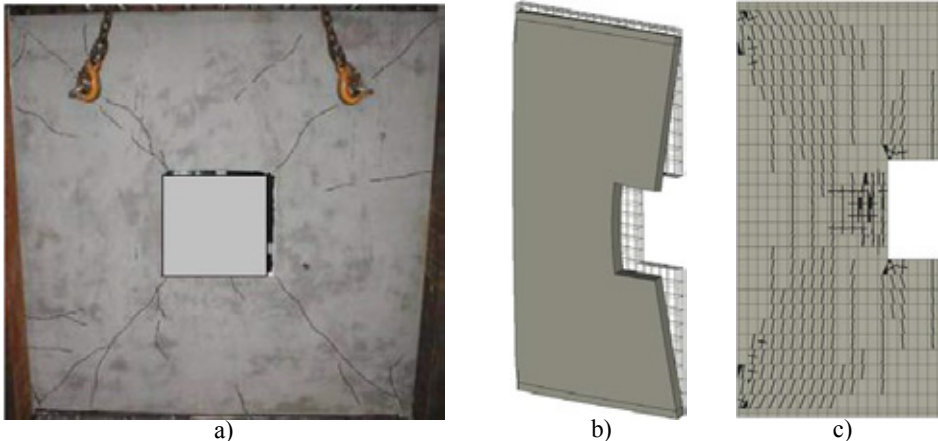(d) the design was carried out for the strongest element, i.e. RCW (solid wall).

Figure 8 – Crack pattern and failure mode for two-way walls: a) experimental [12]; b) deformed shape - FEM; c) crack pattern - FEM

5.2   Load reactions and element's design

Considering the good agreement with the experimental results, the FEM model proposed was used to predict the ultimate capacity of the strongest wall, i.e. RCW wall from the matrix proposed (see Figure 2). The ultimate capacity obtained from FEM analysis was 1797 kN. This value was used to find out the required number of the hydraulic actuators. The concentrated force from the actuators was considered to be redistributed through the loading beam with a slope of 1:1 in order to obtain a uniformly distributed load along the wall length. Four hydraulic actuators of 600 kN each were necessary to be above the force obtained from FEM.

By loading to failure the solid wall, the reaction forces acting on the members who simulate the boundary conditions of the specimen were also monitored in FEM model. The reactions at the bottom of the specimen were constant along its length and were used to design the supporting beam. The beam was designed as continuously supported on a strong floor. Reactions along lateral edges of the specimen were used in designing the lateral bracing system of the test rig. Besides some high values at the end of the wall, constant forces acting on the members restraining the specimen from out-of-plane deflections were observed. These reactions were used as input for the simple static system created (see Figure 9) in which both stresses and displacements were checked. All reactions obtained from FEM analysis were multiplied by a factor of 1.4 to cover the difference between the ultimate capacity of the solid wall and the available pressure given by the actuators (see Figure 10).

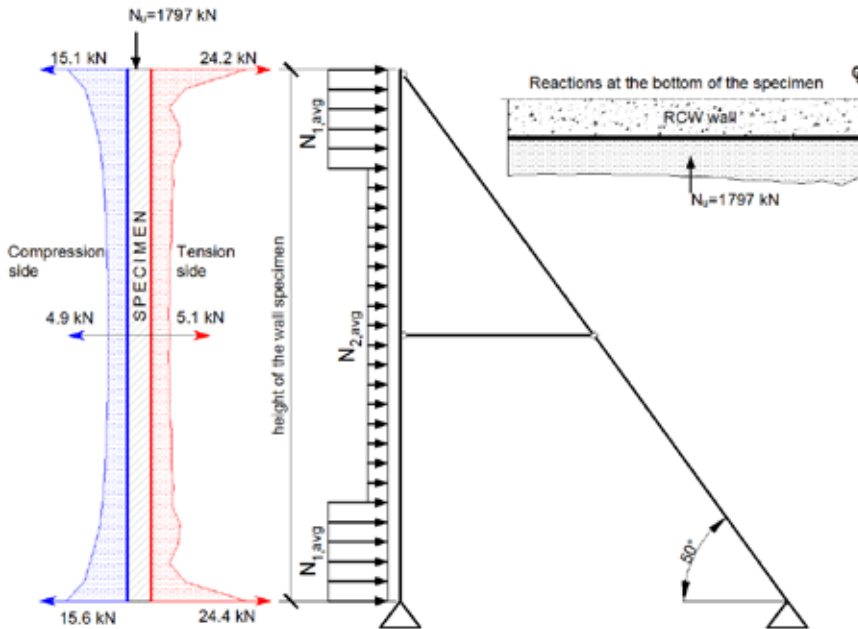*Figure 9 – Load reactions acting on the test rig and its static system*

Figure 10 shows the general view of the test-rig with all details. The hinge at the top support is created by the steel rod placed on a thick steel plate along the element edges. In this way the desired eccentricity can also be precisely applied. The wall specimens were restrained along their sides using either equal or unequal leg angles steel profiles.
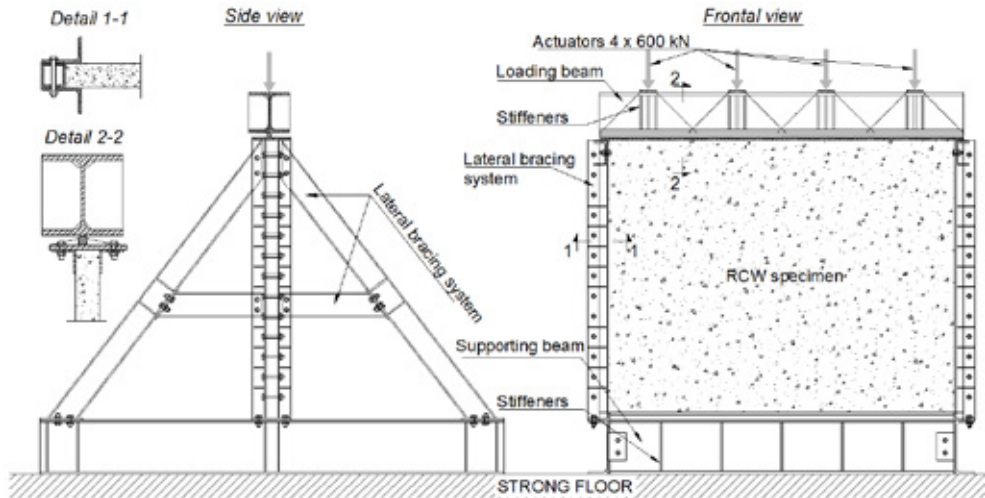
Figure 10 – General view of the test-rig proposed

6.   CONCLUSIONS

There are no standardized procedures for testing concrete walls; therefore each experimental programme requires customized design. The experimental program presented in this paper was conceived in accordance with DOE technique. This method has been demonstrated to be a reliable method for research investigations in areas like physics, chemistry or mechanical engineering. However, most of the problems encountered in structural engineering domain are dependent on certain variables; thus, the application of DOE could be useful in a broad range of testing situations.

Two-level factorial design was performed on walls with openings aiming to obtain the test matrix in order to study the influence of opening size and the effectiveness of the strengthening patterns. Two methods for strengthening of RC walls with openings have been proposed: (1) traditional by embedding steel reinforcement and (2) a modern technique using FRP materials.

The design of a new test-rig was presented and analysed through nonlinear simulations. The constitutive model used for concrete was able to predict the axial capacity of concrete walls with openings. Furthermore, the FEM model calibrated on a previous experimental program was used to model the strongest wall from the test matrix. Reaction forces obtained from this simulation were used to design the test-rig. The results from this experimental program will be presented in a future publication.

REFERENCES

1. Dol, K., Haffner, M., Housing Statistics in the European Union 2010. Delft University of Technology, Netherlands: OTB Research Institute for the Built Environment; 2010.
2. Demeter, I., Seismic retrofit of precast rc walls by externally bonded CFRP composites. Romania: PhD Thesis, Politehnica University of Timisoara; 2011.
3. Mohammed, B., Ean, L. W., Malek, M. A., "One way RC wall panels with openings strengthened with CFRP", *Construction and Building Materials*, Vol. 40, No. 2013, pp. 575-83.
4. Hollaway, L. C., "A review of the present and future utilisation of FRP composites in the civil infrastructure with reference to their important in-service properties", *Construction and Building Materials*, Vol. 24, No. 12, 2010, pp. 2419-45.
5. Täljsten, B., Thomas Blanksvärd, Sas, G., FRP strengthening of existing concrete structures. Design guideline (in Swedish). Luleå, Sweden: Luleå University of Technology, Division of structural engineering,; 2012.
6. El Maaddawy, T., Sherif, S., "FRP composites for shear strengthening of reinforced concrete deep beams with openings", *Composite Structures*, Vol. 89, No. 1, 2009, pp. 60-9.
7. Floruţ, S.-C., Sas, G., Popescu, C., Stoian, V., "Tests on reinforced concrete slabs with cut-out openings strengthened with fibre-reinforced polymers", *Composites Part B: Engineering*, Vol. 66, No. 0, 2014, pp. 484-93.
8. Doh, J. H., Fragomeni, S., "Ultimate Load Formula for Reinforced Concrete Wall Panels with Openings", *Advances in Structural Engineering*, Vol. 9, No. 1, 2006, pp. 103-15.
9. Fragomeni, S., Doh, J. H., Lee, D. J., "Behavior of Axially Loaded Concrete Wall Panels with Openings: An Experimental Study", *Advances in Structural Engineering*, Vol. 15, No. 8, 2012, pp. 1345-58.
10. Guan, H., Cooper, C., Lee, D.-J., "Ultimate strength analysis of normal and high strength concrete wall panels with varying opening configurations", *Engineering Structures*, Vol. 32, No. 5, 2010, pp. 1341-55.
11. Saheb, S. M., Desayi, P., "Ultimate strength of RC wall panels with openings", *Journal of structural engineering*, Vol. 116, No. 6, 1990, pp. 1565-78.
12. Lee, D.-J., Experimental and theoretical study of normal and high strength concrete wall panels with openings. Australia: PhD Thesis, Griffith University; 2008.
13. Fischer, R. A., The design of experiments. Edinburgh, Scotland: Oliver and Boyd; 1935.
14. Wagner Jr, J. R., Mount III, E. M., Giles Jr, H. F. 25 - Design of Experiments. Extrusion (Second Edition). Oxford: William Andrew Publishing; 2014. p. 291-308.
15. DeCoursey, W. J., Statistics and probability for engineering applications with Microsoft Excel. Amsterdam; Boston: Newnes. : ebrary, Inc. Elsevier Science Publishers,; 2003.
16. Popescu, C., Sas, G., Täljsten, B., Blanksvärd, T., "A state of the art review on walls with openings strengthened by use of fiber reinforced polymers", *Proceedings of the 7th International Conference on FRP Composites in Civil Engineering* (CICE 2014). Vancouver, British Columbia, Canada: International Institute for FRP in Construction (IIFC); 2014.
17. Doh, J. H., Fragomeni, S., "Evaluation of Experimental Work on concrete walls in One-Way and Two-Way Action", *Australian journal of structural engineering*, Vol. 6, No. 1, 2005, pp. 37-52.
18. Fragomeni, S., Mendis, P., "Improved axial load formulae for normal and high strength reinforced concrete walls", *Australian Civil Engineering Transactions, Institution of Engineers*, Vol. 38, No. 2/3/4, 1996, pp. 71-81.

19. Pillai, S. U., Parthasarathy, C. V., "Ultimate strength and design of concrete walls", *Building and Environment*, Vol. 12, No. 1, 1977, pp. 25-9.
20. Saheb, S. M., Desayi, P., "Ultimate Strength of R.C. Wall Panels in Two-Way In-Plane Action", *Journal of structural engineering*, Vol. 116, No. 5, 1990, pp. 1384-402.
21. Box, G. E. P., Hunter, W. G., Hunter, J. S., Statistics for experimenters: An introduction to design, data analysis, and model building. New York: John Wiley & Sons; 1978.
22. EN 1992-1-1. Eurocode 2: Design of concrete structures - Part 1–1: General rules and rules for buildings. Brussels: COMITÉ EUROPÉEN DE NORMALISATION; 2004.
23. MiniTab. "MiniTab, Inc.", Vol. State College, PA.
24. AS3600. Concrete Structures. Sydney, Australia: Standards Australia; 2004.
25. ATENA. Advanced Tool for Engineering Nonlinear Analysis, Atena Studio, Cervenka Consulting Ltd., Prague, Czech Republic; 2014.
26. Cervenka, J., Papanikolaou, V. K., "Three dimensional combined fracture-plastic material model for concrete", *International Journal of Plasticity*, Vol. 24, No. 12, 2008, pp. 2192-220.
27. Menetrey, P., Willam, K. J., "Triaxial failure criterion for concrete and its generalization", *ACI Structural Journal*, Vol. 92, No. 3, 1995, pp. 311-8.
28. De Borst, R., Non-linear analysis of frictional materials [Ph.D. Thesis]: Delft University of Technology; 1986.
29. Reinhardt, H., Cornelissen, H., Hordijk, D., "Tensile Tests and Failure Analysis of Concrete", *Journal of structural engineering*, Vol. 112, No. 11, 1986, pp. 2462-77.
30. van Mier, J. M., "Multiaxial strain-softening of concrete", *Materials and Structures*, Vol. 19, No. 3, 1986, pp. 179-90.
31. CEB-FIP Model Code 1990: Design Code. Thomas Telford Ltd.; 1993.
32. Vos, E., "Influence of loading rate and radial pressure on bond in reinforced concrete. A numerical and experimental approach", Dissertation, Delft University Press, 1983

Stresses in water filled pools within nuclear facilities subjected to seismic loads

Cecilia Rydell
Lic. Eng., Ph.D. Student
Vattenfall AB
BU Operations Support
SE-169 92 Stockholm, Sweden
E-mail: cecilia.rydell@vattenfall.com

Tobias Gasch
MCs., Ph.D. Student
KTH Royal Institute of Technology
Division of Concrete Structures
SE-100 44 Stockholm, Sweden
E-mail: tobias.gasch@byv.kth.se

Daniel Eriksson
MSc.
Sweco Energuide
Hydro Power & Dams
SE-100 26 Stockholm, Sweden
E-mail: daniel.eriksson@sweco.se

Anders Ansell
Professor
KTH Royal Institute of Technology
Division of Concrete Structures
SE-100 44 Stockholm, Sweden
E-mail: anders.ansell@byv.kth.se

ABSTRACT

This paper presents a study on water filled pools within nuclear facilities subjected to seismic loads. The type of structure studied is an elevated rectangular concrete tank, supported by the reactor containment, which is a high cylindrical concrete structure. Seismic analysis is performed using finite element models, accounting for fluid-structure interaction (FSI) between the water and the concrete structure. The stresses in a concrete pool are calculated, also investigating the changes in stresses as additional cross-walls are added. The effects from earthquakes dominated by low and high frequencies are evaluated, representative for conditions at the West coast of North America and Northern Europe, respectively. It is shown that the coupled fluid-structure systems have more significant modes in the high frequency range compared to the models without water, that is, for frequencies at which the Northern European type earthquake has significant

energy compared to the Western North American earthquake. The seismic analyses show that the relative increase of hydrodynamic pressure is higher when the outer walls of the pool are stiffened due to the inclusion of additional cross-walls. With the inclusion of additional cross-walls, modes with lower natural frequencies, although still relatively high, become more important for the hydrodynamic pressure response. Leading to a higher stress response in the outer walls of the pool for models including the additional cross-walls compared to models without cross-walls. The study indicates that the effect from fluid-structure interaction is of great importance also for seismic loads with relatively high-frequency content.

1.   BACKGROUND

Nuclear facilities are probably the today existing infrastructure buildings with the highest safety levels with respect to severe dynamic events such as explosions, collisions and earthquakes. Dynamic evaluation of these large and complex buildings and structures require analyses with advanced numerical methods and must be based on the detailed knowledge of the structural properties as well as the load characteristics. At some regions the risk of earthquakes is great, and due to recurring seismic events there also exist knowledge about the characteristics of these events. However, the high level of safety kept in nuclear facilities worldwide makes it necessary to perform seismic analysis also for regions where the risk for major earthquakes is comparatively small, such as in northern Europe and, for example, Sweden. Here, dynamic, seismic analyses are based on standard design response spectra, compiled through seismic hazard analysis and processing of empirical data from a more seismic region of the world, in this case Japan, to correspond to Swedish conditions [1]. Often, the characteristics of earthquakes vary for different regions, e.g. due to the stiffness of the bedrock etc., and depending on region, the dominant frequencies may differ and may have a higher or lower effect on each of the components or sub-systems that are parts of a nuclear facility.

These large and complex buildings include reactors and their containments but also systems for electricity generation and supportive infrastructure. Amongst the nuclear infrastructure systems are water filled pools, e.g., used for spent fuel and as condensation pools. Containers with large volumes of water affect the dynamic behaviour of the structures in several ways during an earthquake, which must be accounted for in a seismic analysis. The mass of the water will reduce the natural frequencies of the structure compared to a case with an unfilled container. The water also contributes with hydrostatic and hydrodynamic water pressure on the walls of the pools, which is caused by wave propagation in the fluid. Often, the containers have a free water surface and there will in such cases also be propagation of free surface waves that causes sloshing effects. A case where a deforming solid structure interacts with an internal or surrounding fluid is usually categorized as a fluid-structure interaction (FSI) problem. In numerical analyses there are several different methods to account for the FSI, depending on the need for included details, computational efficiency and accuracy.

The phenomena of fluid-structure interaction for liquid-filled containers have been extensively studied, but much of the focus in research has been on cylindrical liquid storage tanks, especially when it comes to elevated tanks. Already in 1931 Westergaard [2] developed an analytical method to account for the changes of water pressures on a dam during an earthquake. The dynamic behaviour of water tanks was later studied by Housner [3] and Epstein [4], who further developed the method in [3]. Faltinsen [5] presented an analytical linear solution to account for sloshing in a rectangular liquid storage tank when subjected to a horizontal base motion. More recent studies that deal with the dynamic behaviour of rectangular liquid containing tanks subjected to ground movements at their base include [6–11] among others. Studies on the seismic behaviour of elevated tanks have also been done, see e.g. [12–15]. Other recent investigations of FSI for concrete dams and large water reservoirs are found in [16–18] and for nuclear facilities in [19–20]. The present paper investigates the dynamic behaviour of an elevated rectangular concrete water pool within a nuclear facility, an elevated pool structure that is relatively scarce in the published literature. Analyses are performed for two types of seismic loads with substantially different frequency content and the influence of pool partition walls is evaluated. Only the impulsive motion of the liquid is accounted for in the analysis, that is, the effect of gravity waves on the free water surface is not included, but the existence of a free water surface is accounted for by prescribing zero pressure on the free surface. This simplification affects the kinematic behaviour of the free surface but it is assumed that it does not affect the overall structural behaviour, which is of main interest in this study.

2.   SEISMIC EXITATION

The analyses are performed using direct time integration, which also will be possible to use for future, non-linear models. The seismic ground acceleration time histories applied as boundary conditions at the base of the modelled structure. Two types of seismic input are considered, a large earthquake with mainly low frequency content and a smaller earthquake with relatively high frequencies, of the type prescribed in the Swedish design guideline [1]. The first set (x, y and z directions) of time histories consists of records from the El Centro earthquake, which is often used to exemplify earthquakes typical for the US west coast, see e.g. [21]. This earthquake occurred in May 1940 close to the border between USA and Mexico, with relatively large amplitudes and a registered moment magnitude of 6.9. The second set of time histories corresponds to a typical design earthquake defined in the guideline for Swedish conditions [1], with relatively small amplitudes and containing higher dominant frequencies.

2.1 Earthquake time histories

A ground acceleration time history for the El Centro earthquake is shown in Figure 1a, with duration of approximately 50 seconds and a maximum acceleration of 0.35 g for this North-South horizontal component. The full set of seismic accelerations also consists of a vertical and an East-West horizontal component. The time histories, obtained from [22], are 53.78 seconds long, with 2690 time points spaced at $\Delta t = 0.01$ seconds. A time history for the Swedish design ground acceleration used in this study [23] is shown in Figure 1b. It reaches 0.15 g and has a much shorter duration than the El Centro earthquake, only about 7 seconds, which here is represented by a 10 second sequence of 2001 time points spaced at $\Delta t = 0.005$ seconds. Also in

this case two horizontal and one vertical component is defined, which are statistically independent. These time histories are generated to match the 10-5 Swedish design response spectra for 5% damping [1], following the provisions in ASCE 4-98 [24].

2.2 Earthquake frequency spectra

The frequency spectra for the two earthquakes used in the analyses are compared in Figure 2 for all three components, one vertical and two horizontal. To note is that the Swedish design response spectra have no frequency content above 50 Hz, being the zero period acceleration frequency. For the horizontal components it can be seen that the El Centro time histories have most energy content for frequencies below 5 Hz while the Swedish design histories are dominated by frequencies between 8 and 20 Hz. For the vertical component the energy content is more similar between the earthquakes although the El Centro time history still is dominated by the lower frequencies and the Swedish by the higher frequencies. Of special interest in the following analyses is how these differences in the frequency content affect the stresses of the type of water filled pool studied. The characteristics of the two earthquakes differ due to, for example, magnitude of earthquake, distance to fault and geological conditions. How the frequency-content of the earthquake affects the structural response has earlier also been studied for piping systems in nuclear facilities [25].
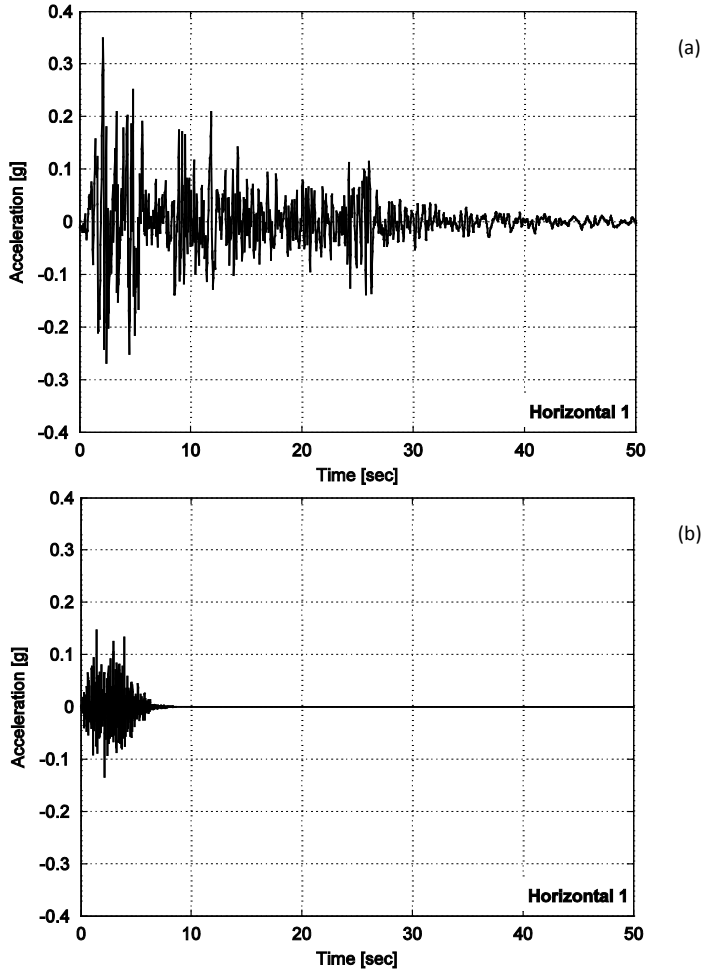
Figure 1 – Ground movement time history, horizontal component 1 (N-S) of the El Centro earthquake (a) and horizontal component 1 of the Swedish design earthquake (b).
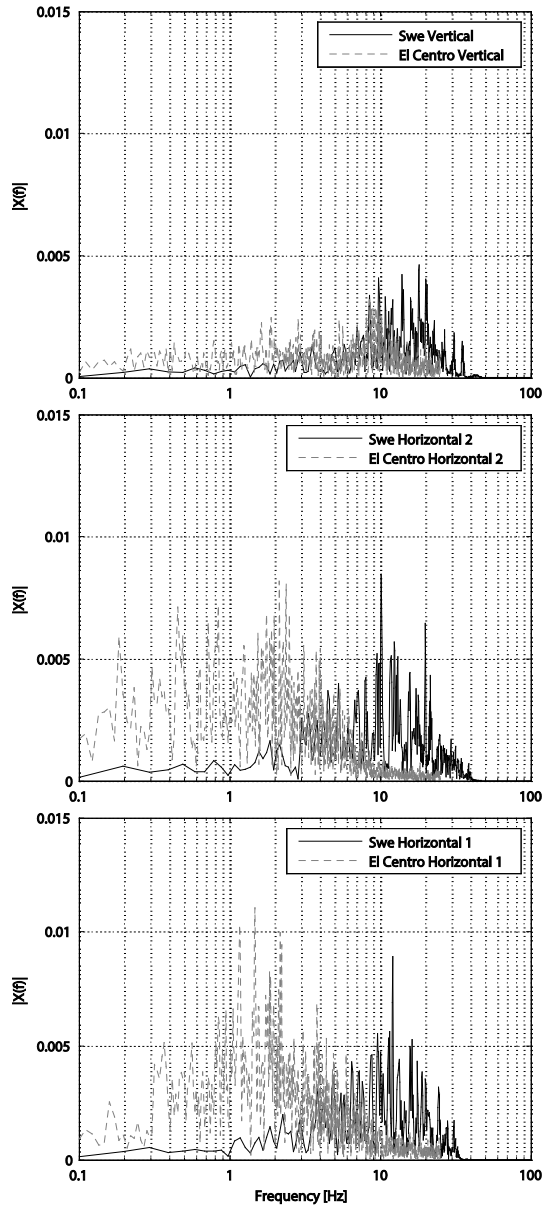
Figure 2 – Ground movement frequency spectra for the three components of the El Centro and the Swedish design earthquakes.

3.   STUDIED WATER FILLED POOL

The structure studied is a typical water filled pool, located within the reactor containment building of a Swedish boiling water reactor founded on rock [19]. The concrete pool has a free water surface and is elevated 40 m above the ground level. It is supported by the concrete containment for the reactor and its dynamic response to seismic loads will thus also depend on the elastic properties and mass of this structure. The model of the studied water container is given a simplified geometry compared to the real structure, but the overall dimensions and properties are chosen to accurately describe the dynamic behaviour of the pool, the water content and the concrete structure of the supporting containment.

3.1 Geometry

The geometry of the reactor containment with the water pool and an elastic supporting concrete containment is shown in Figure 3. The concrete water pool has an outer rectangular 42×9 m^2 cross section, with a height of 13 m and a wall thickness of 1.1 m. For the analysis the water surface is assumed to be at a level 1 m below the upper edge of the pool. A case with partition walls is also studied, the partition walls being placed 9 m from the outer short walls and with a thickness of 1 m, see Figure 5. The direction of the first horizontal acceleration component given in Figure 2 is assumed to be aligned with the longest sides of the pool while the second component consequently follows the direction of the shorter sides. In the real structure, the 40 m high supporting concrete structure is circular with an outer diameter of 24.2 m and a wall thickness of 1.6 m, also containing horizontal and vertical pre-stressing tendons to resist internal pressures. Here, this structure has been modelled as a beam with a pipe cross section and with the pre-stressing effect omitted in the elastic analyses carried out. This approximation is motivated since the pre-stressing tendons have little influence on the dynamic properties of the structure, such as the natural frequencies and the response from seismic loading. The pre-stressing do, however, lead to crack reduction, thus contributing to the accuracy of the assumed elastic behaviour.
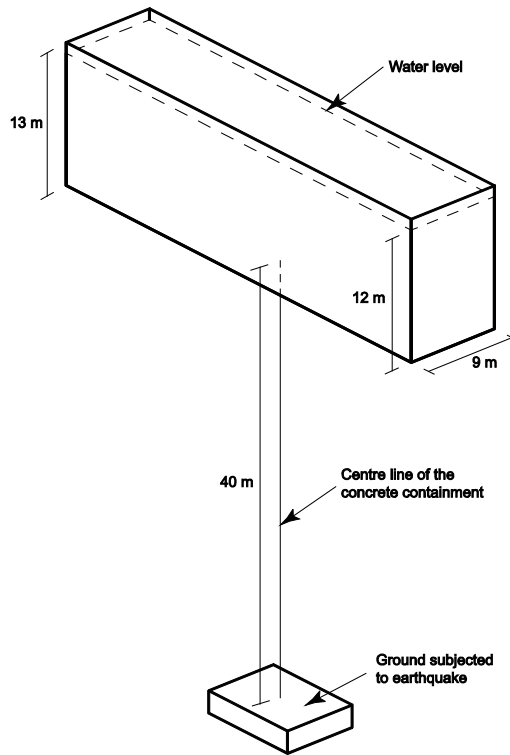
Figure 3 – Geometry of the reactor containment model used in the analyses.

3.2 Materials and damping

As explained in the previous section, the pre-stressing tendons of the containment are not included in the model and this is also the case with all other reinforcement in the concrete structures. Thus, these are given linear elastic material properties, with a density of 2400 kg/m³, an elastic modulus of 30 GPa and a Poisson's ratio that is 0.2. The only other material defined for the model is water, which is given standard properties, i.e., a density of 1000 kg/m³ and a bulk modulus of 2.2 GPa. Of great importance in a seismic analysis is the accuracy of the damping properties assigned to the structure. Damping values suitable for seismic design of nuclear power plants are given in the American Regulatory Guide 1.61 [26], which is also followed in e.g. Sweden. In this case the damping ratio for the concrete structures is assumed to be 3%, also accounting for the pre-stressing effect. The water is modelled without considering damping. For a direct time integration finite element (FE) analysis the damping must be explicitly modelled using dashpots or defined at material level as e.g. Rayleigh damping, which is chosen in this case. The damping ratio is thus given by:

$$\xi = \frac{\alpha}{2\omega} + \frac{\beta\omega}{2} \tag{1}$$

where $\omega = 2\pi f$ is the circular frequency and α and β the Rayleigh damping factors, see e.g. [21]. The damping factors for the concrete are here chosen as $\alpha = 0.95744$ and $\beta = 0.00030315$, which gives the frequency dependence shown in Figure 4. The factors have been chosen so that the damping ratio is less than 3% in the frequency interval $3 \leq f \leq 30$ Hz.

3.3 Mesh and modelling techniques

A finite element model is implemented using the FE simulation software Abaqus 6.12-1 [27] with the materials assumed to be in the elastic range through the earthquake. The model and mesh are shown in Figure 5 and consist of three types of elements for the pool, the water and the supporting containment. In Figure 5 the partition walls are also included. The walls of the pool are built up with 4-noded shell elements with full numerical integration using an average element length of 1 m, which proved to give accurate results. For the water, 8-noded acoustic elements with full numerical integration are used, also in this case with an element length of 1 m. The concrete containment is modelled with 10 beam elements with a pipe cross section, each 4 m long. Elements based on Timoshenko beam theory is used in order to describe transverse shear deformations in the relatively large cross section of the original structure. This beam is connected to the bottom of the pool using rigid links distributed over an area that correspond to the diameter of the containment. The seismic load is applied as acceleration time histories in three orthogonal directions at the lower end of the beam, keeping the rotational degrees of freedom restrained.
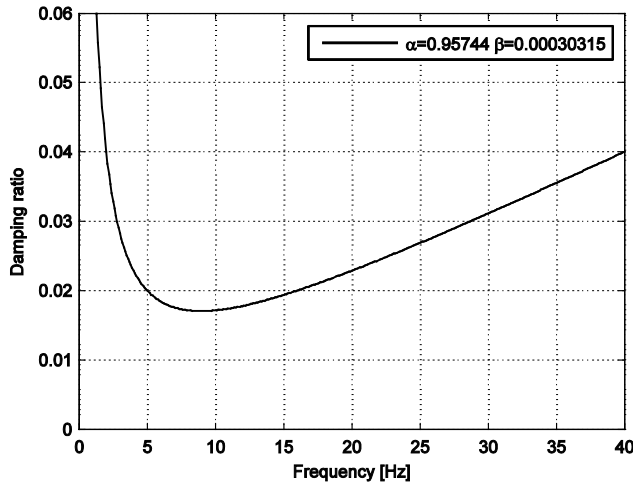

Figure 4 – Rayleigh damping for the structural parts in the FE-model.

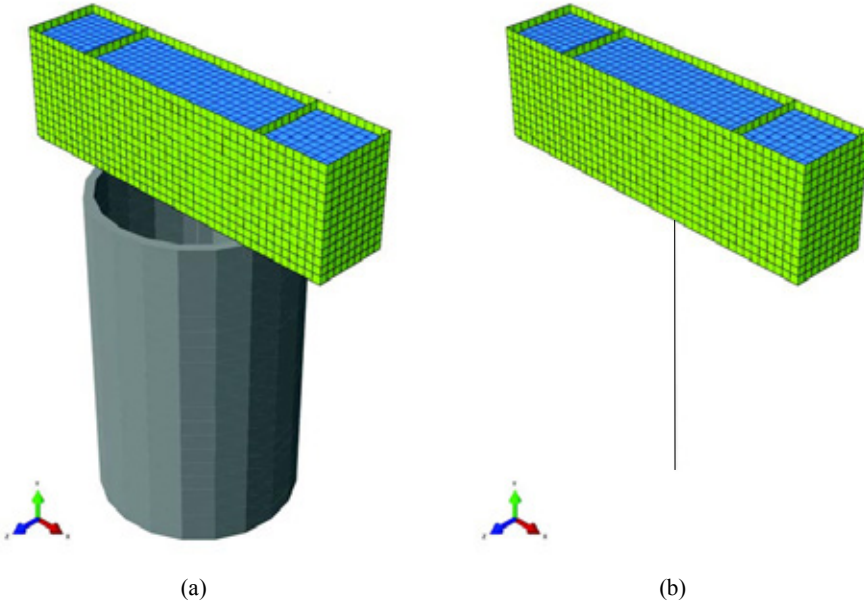(a)   (b)

Figure 5 – Model with a rendered version of the beam element representing the concrete containment (a) and mesh of the concrete containment with water (b). Here, the partition walls are also shown.

3.4 Fluid-structure interaction

The effect from the fluid-structure interaction between the water and the pool is described by the use of a linear acoustic wave formulation for the water, with the fluid pressure as the independent variable, see [19]. The equation of acoustic wave propagation is derived from the theory of fluid dynamics, with assumptions made regarding the acoustic medium that simplifies the equations, see e.g. [28]. The equations describing the conservation of momentum and the conservation of mass, respectively, given that the fluid is homogeneous and isotropic, its viscosity is neglected, the flow is irrational and the amplitude of the acoustic disturbance is small and the wave propagation process is adiabatic and reversible, are here:

$$\rho_f \frac{\partial \dot{\mathbf{u}}}{\partial t} + \nabla p = 0 \tag{2}$$

and:

$$\frac{\partial p}{\partial t} + K_f \nabla \dot{\mathbf{u}} = 0 \tag{3}$$

where ρ_f is the fluid density, $\dot{\mathbf{u}}$ is the fluid particle velocity, t is the time, p is the excess pressure in the fluid and K_f the bulk modulus of the fluid:

$$K_f = \rho_f c_f^2 \tag{4}$$

where c_f is the wave speed. Combining Eqs. (2) and (3) gives the acoustic wave equation with the fluid pressure as the independent variable:

$$\frac{\partial^2 p}{\partial t^2} - c_f^2 \nabla^2 p = 0 \tag{5}$$

To solve for the natural frequencies and corresponding mode shapes, the eigenvalue problem, as defined in Abaqus [27], is:

$$\begin{bmatrix} \mathbf{K}_s & \mathbf{S}_{fs}^T \\ 0 & \mathbf{K}_f \end{bmatrix} \begin{Bmatrix} \mathbf{u} \\ \mathbf{p} \end{Bmatrix} + \omega^2 \begin{bmatrix} \mathbf{M}_s & 0 \\ -\mathbf{S}_{fs} & \mathbf{M}_f \end{bmatrix} \begin{Bmatrix} \mathbf{u} \\ \mathbf{p} \end{Bmatrix} = 0 \tag{6}$$

where $\mathbf{K}_s$, $\mathbf{K}_f$, $\mathbf{M}_s$ and $\mathbf{M}_f$ are the stiffness and mass matrices of the structure and the fluid, respectively, $\mathbf{u}$ is the displacement vector, $\mathbf{p}$ the pressure vector and ω is the (circular) natural frequency of vibration. The term S_{fs} is a coupling matrix between the acoustic and the structural domains at the acoustic-structural interface. On this interface the fluid and the structure have the same displacement normal to the boundary, while the tangential displacements are uncoupled. The acoustic wave formulation in Abaqus does not include body forces. Thus the hydrostatic pressure has to be defined explicitly as a pressure load on the structure. The acoustic elements only have one degree of freedom, being the pressure, and no translational degrees of freedom. For all acoustic nodes, except at the fluid boundaries, the FE mesh is stationary. At the interface between the water and the structure, the nodes of the acoustic elements are rigidly connected to the structure using tie constraints, and at the free water surface a boundary condition prescribing zero pressure is applied. The response to applied seismic loads is calculated using an implicit time integration scheme, see Abaqus [27].

4. NUMERICAL RESULTS

Numerical analyses were first performed to calculate the natural frequencies and modes for the water pool, then to determine the structural response due to the seismic loads, i.e., the two previously described earthquakes. Of special interest, is the effect from inclusion of partition walls. The use of two earthquake loads with different characteristics is done in order to study if a higher frequency content will lead to contribution from modes that increase the stresses.

4.1 Natural frequency analysis

Results from the free vibration analysis of the structure are presented in Table 1, where natural frequencies corresponding to the ten first vibration modes (eigenmodes) are given. These are calculated with and without the stiffening effects from the partition walls, and for comparison results for an empty pool are also included. The variation of accumulated effective mass is shown in Figure 6, for the case with empty and water filled pool, respectively, and without and with partition walls, respectively. When comparing the four cases (a-d) a difference in accumulated mass for a given frequency (or mode number) thus indicate a difference in free vibration mode. The case with water filled pool is calculated with a coupled acoustic-structural model according to Equation 6. The accumulated acoustic effective mass is also shown for each eigenmode. Normally, the higher the acoustic effective mass, the more significant the mode is in accurately representing the hydrodynamic pressure. The figure shows the accumulated effective mass for every natural frequency, and indirectly its corresponding mode number.
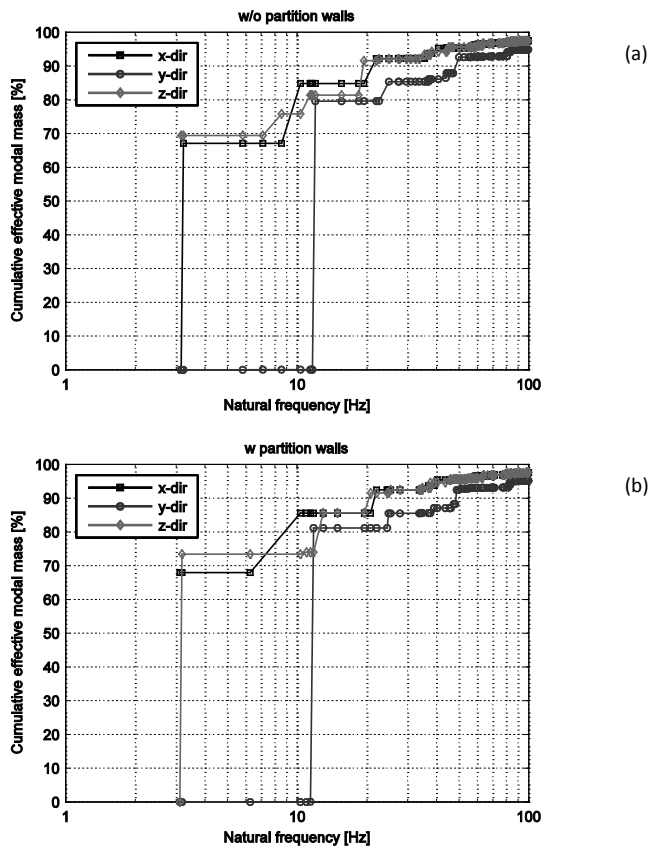
Figure 6 – Accumulated effective mass, for the case with structure only (a) (b) and for the case with water filled pool (c) (d). For models without and with partition walls, respectively (continues).
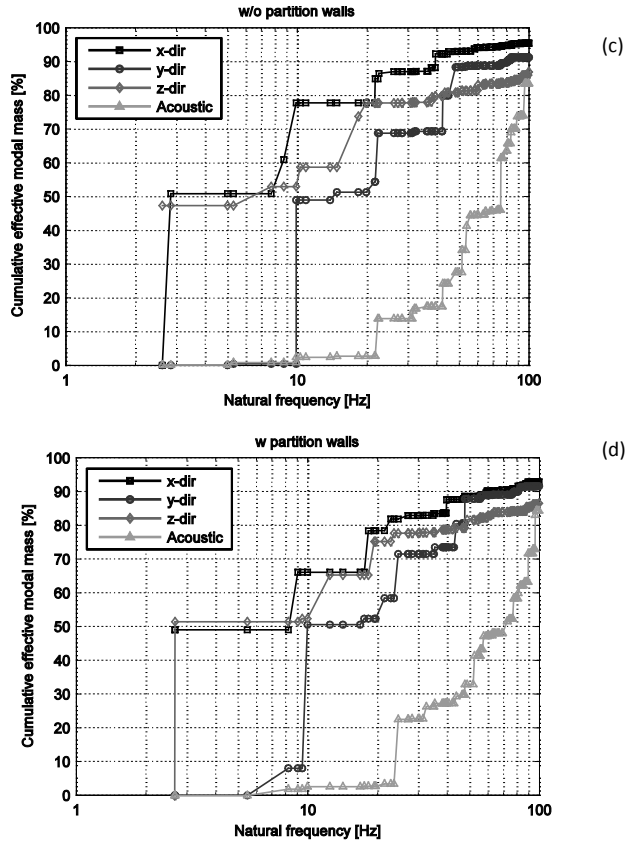
Figure 6 – Continued.

Table 1 – The ten first natural frequencies for the structural system with and without water.

Mode no.	Without partition walls:		With partition walls:	
	Structure only (Hz)	Structure and water (Hz)	Structure only (Hz)	Structure and water (Hz)
1	3.15	2.61	3.11	2.66
2	3.22	2.84	3.18	2.67
3	5.82	4.99	6.26	5.47
4	7.10	5.29	10.32	8.24
5	8.56	7.70	10.98	9.05
6	10.33	8.74	11.43	9.46
7	11.39	9.87	11.77	9.96
8	11.55	9.87	12.97	12.45
9	11.64	10.29	14.95	14.17
10	11.97	10.88	19.53	16.82

4.2 Earthquake excitation analyses

Results from the earthquake excitation time-history analyses are presented in Figures 7–10. To investigate the stress state in the pool walls, the maximum principal stress is chosen as a measure since this gives the maximum tensile stress component, which is important for concrete structures. The envelopes of the minimum and the maximum values of the maximum principal stress for each node over the height of the pool walls are shown in Figures 7–8. The stresses are for sections at, or close to, the mid-side of the pool walls and are extracted for the outer side of the pool walls. Results obtained with and without the partition walls are compared, due to the Swedish design earthquake and the El Centro earthquake, respectively. For reference, the stress response due to static analysis, including hydrostatic pressure, is also given. To compare the dynamic stress response for a model including water to that for a model without water, the stress ratio of the largest maximum principal stresses over the height of the pool walls are given in Figure 9, for sections at mid-side of the walls. Stress ratios are given for both earthquakes considered and for the cases with and without partition walls. To show how the hydrodynamic water pressure against the pool walls varies with the depth of water, the ratio of hydrodynamic pressure to hydrostatic pressure is plotted in Figure 10, for the mid-side of the long and the short wall, respectively. The figure shows the response due to the Swedish design earthquake and to the El Centro earthquake. Results obtained with and without the partition walls are compared. The hydrostatic water pressure ranges from 0 kPa at the surface to approximately 120 kPa at the bottom.
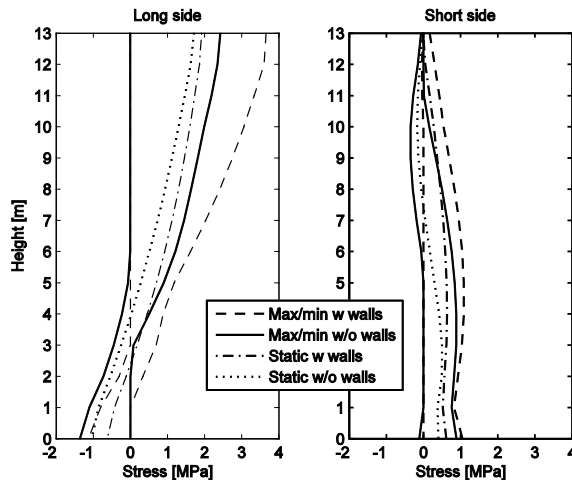
Figure 7 – Envelope of the maximum principal stresses on the outer surface of the pool, over the height of the long and the short wall, for a model with and without partition walls, respectively. For the Swedish design earthquake.
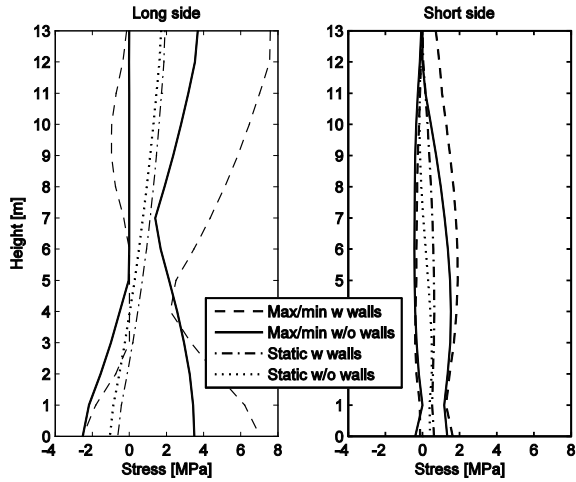
Figure 8 – Envelope of the maximum principal stresses on the outer surface of the pool, over the height of the long and the short wall, for a model with and without partition walls, respectively. For the El Centro earthquake.

Figure 9 – Maximum distributed dynamic tensile stress on the outer surface of the long and the short wall, normalized with respect to stress without water, for models with and without partition walls, respectively. Results calculated for the Swedish design earthquake and the El Centro earthquake.

Figure 10 – Maximum distributed hydrodynamic pressure against the long and the short wall, normalized with respect to the hydrostatic pressure for models with and without partition walls, respectively. Results calculated for the Swedish design earthquake and the El Centro earthquake

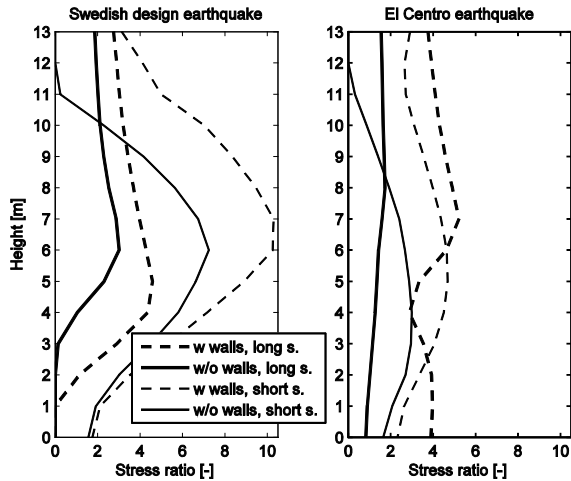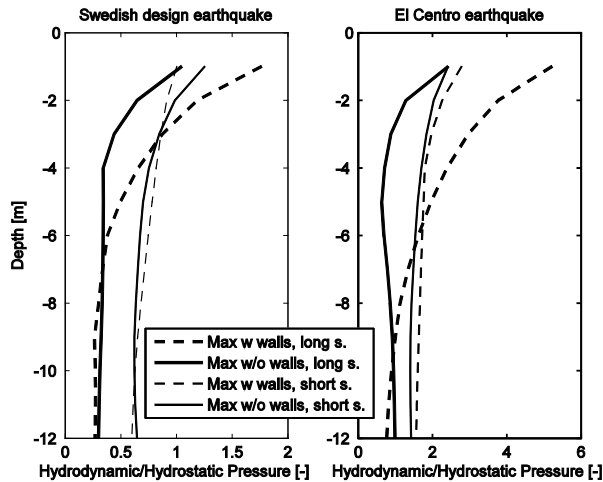## 5. CONCLUSIONS

Including the water of the pool generally lowers the natural frequencies, but as can be seen from Figure 6, the effective masses are also lowered. Hence, higher modes contribute significantly to the response for models including water. That is, modes having natural frequencies at which the Swedish design earthquake has significant energy compared to the El Centro earthquake, see Figure 2. The El Centro earthquake has its dominant energy content for the horizontal directions for frequencies below 5 Hz. This might explain the higher relative increase of dynamic stress when water is included for the Swedish design earthquake compared to the El Centro earthquake, as seen in Figure 9. To note is that the first two vibration modes change positions when partition walls are included. For the coupled fluid-structure models, it is first for modes with natural frequencies above approximately 8 Hz that the acoustic effective mass indicates that the modes are important in accurately representing the hydrodynamic pressure. From the figure it can also be seen that the accumulated acoustic effective mass rises faster for the model with included partition walls compared to the model without. That is, modes with lower natural frequencies, although still relatively high, become more important for the hydrodynamic pressure response. This might explain the larger peak maximum principal stress distribution for the model including partition walls compared to the model without partition walls, as can be seen in Figure 7 and 8. To note is that the water does affect the modes with lower frequencies as well and there is an acoustic component present for most modes. Further, it is important to note that the individual time histories do not possess the frequency enveloping characteristics of seismic design response spectra, and thus the response will depend strongly on the specific frequency content of the individual time histories used in the analyses. To draw more general conclusions, further analyses with different seismic input would need to be performed.

The relative increase of the hydrodynamic pressure to the hydrostatic pressure is higher when the outer walls are stiffened due to the inclusion of partition walls, as can be seen in Figure 10. The effect can be seen for the long outer walls of the pool when the partition walls are added. It can also be seen that the partition walls do not particularly affect the hydrodynamic pressure variation against the short outer walls of the pool. The natural frequencies of gravity surface waves (convective pressure term) tend to be low, in this case in the range 0.1–0.3 Hz depending on direction and water volume considered. The effect of the gravity surface waves is therefore expected to be more important when the seismic load has a dominant low-frequency content that coincides with the frequencies of the fundamental convective modes of the fluid, than when the seismic load has a relatively high-frequency content, e.g., as the Swedish design earthquake. The coupled fluid-structure system has on the other hand significant impulsive modes in the high-frequency range, hence the impulsive pressure term is expected to be more important for seismic loads with a relatively high-frequency content. To note is that the effects of gravity surface waves are not accounted for in this study, and future works would need to investigate if this assumption is adequate for this type of structure. A drawback with the acoustic wave formulation in Abaqus is that it does not include body forces. Other formulations do exist in other general finite element software products, see [19], and may be more suitable for dynamic fluid-structure interaction problems where the fluid has a relatively high density.

The study indicates that the effect of accounting for fluid-structure interaction is of great importance also for seismic high-frequency loads. Although the seismic high-frequency load may not significantly affect the structure itself when water is not included, the stress increase in the structure may be significant when fluid-structure interaction is accounted for, see Figure 9. However, the results indicate that the relative increase is larger for the Swedish design earthquake than the El Centro earthquake, for the evaluated parameter.

ACKNOWLEDGEMENTS

REFERENCES

1. Characterization of seismic ground motions for probabilistic safety analysis of nuclear facilities in Sweden, SKI Technical Report 92:3. Stockholm: National Nuclear Power Inspectorate; 1992.
2. Westergaard HM. Water pressures on dams during earthquakes. T-ASCE 1931;98:418–433.
3. Housner GW. The dynamic behaviour of water tanks, Bull Seismol Soc Am 1963;53:381–387.
4. Epstein HI. Seismic design of liquid-storage tanks. J Struct Div-ASCE 1976;102:1659–1673.

5. Faltinsen OM. A numerical non-linear method of sloshing in tanks with two-dimensional flow. J Ship Res 1978;22:193–202.

6. Kianoush MR, Chen JZ. Effect of vertical acceleration on response of concrete rectangular liquid storage tanks. Eng Struct 2006;28:704–715.

7. Ghaemmaghami AR, Kianoush MR. Effect of wall flexibility on dynamic response of concrete rectangular liquid storage tanks under horizontal and vertical ground motions. J Struct Eng-ASCE 2010;136:441–451.

8. Kianoush MR, Ghaemmaghami AR. The effect of earthquake frequency content on the seismic behaviour of concrete rectangular liquid tanks using the finite element method incorporating soil-structure interaction. Eng Struct 2011;33:2186–2200.

9. Hashemi S, Saadatpour MM, Kianoush MR. Dynamic behaviour of flexible rectangular fluid containers. Thin Wall Struct 2013;66:23–38.

10. Livaoglu R. Investigation of seismic behaviour of fluid-rectangular tank-soil/foundation systems in frequency domain. Soil Dyn Earthq Eng 2008;28:132–146.

11. Virella JC, Prato CA, Godoy LA. Linear and nonlinear 2D finite element analysis of sloshing modes and pressures in rectangular tanks subject to horizontal harmonic motions. J Sound Vib 2008;312:442–460.

12. Livaoglu R, Dogangün A. Simplified seismic analysis procedures for elevated tanks considering fluid-structure-soil interaction. J Fluid Struct 2006;22:421–439.

13. Dutta SC, Dutta S, Roy R. Dynamic behaviour of R/C elevated tanks with soil-structure interaction. Eng Struct 2009;31:2617–2629.

14. Moslemi M, Kianoush MR, Pogorzelski W. Seismic response of liquid-filled elevated tanks. Eng Struct 2011;33:2074–2084.

15. Shakib H, Omidinasab F. Effect of earthquake characteristics on seismic performance of RC elevated water tanks considering fluid level within the vessels. Arab J Sci Eng 2001;36:227–243.

16. Malm R, Rito Pi C, Hassanzadeh M, Rydell C, Gasch T. Fluid structure interaction. arch dam-reservoir at seismic loading, In: XII ICOLD Benchmark Workshop on Numerical Analysis of Dams. Graz: Icold; 2013.

17. Malm R, Gasch T. Finite element analyses of an arch dam subjected to seismic loads and hydrodynamic forces. In: XXII Concrete Research Symposium. Reykjavik: Nordic Concrete Association; 2014.

18. Hellgren R. Influence of fluid structure interaction on a concrete dam during seismic excitation – Parametric analyses of an arch dam-reservoir-foundation system, Master thesis. Stockholm: KTH Royal Institute of Technology; 2014.

19. Gasch T, Facciolo L, Eriksson D, Rydell C, Malm R. Seismic analyses of nuclear facilities with interaction between structure and water - Comparison between methods to account for Fluid-Structure-Interaction (FSI), Elforsk report 13:79. Stockholm: Elforsk; 2013.

20. Rydell C, Gasch T, Facciolo L, Eriksson D, Malm R. Interaction between structure and water in seismic analyses of nuclear facilities. In: Transactions, SMiRT-22. San Francisco: Smirt; 2013.

21. Clough RW, Penzien J. Dynamics of structures, 3rd edn. Berkley: Computers & Structures Inc.; 2003.

22. http://www.vibrationdata.com/elcentro.htm. Accessed in March 2014.

23. Suite of ASCE 4-98 Compliant Time-Histories to Swedish 5% Spectra. Buxton High Peak: CREA Consultants; 2007.

24. Seismic analysis of safety-related nuclear structures and commentary, ASCE Standard 4-98. Reston: American Society of Civil Engineers; 1998.

25. Rydell C, Malm R, Ansell A. Piping system subjected to seismic hard rock high frequencies. Submitted to Nuclear Engineering and Design in April 2014.

26. Damping values for seismic design of nuclear power plants, Regulatory Guide 1.61. Washington: U.S. Nuclear Regulatory Commission; 2007.

27. Abaqus 6.12 Online documentation. Providence: Dassault Systèmes Simulia Corp; 2012.

28. Reynolds DD. Engineering principles of acoustics – noise and vibration control. Boston: Allyn and Bacon; 1981.

Instrumentation and Full-Scale Test of a Post-Tensioned Concrete Bridge

Niklas Bagge
M.Sc., Ph.D. student
Luleå University of Technology
SE-972 87 Luleå
E-mail: niklas.bagge@ltu.se

Jonny Nilimaa
M.Sc., Tech. Lic., Ph.D. student
Luleå University of Technology
SE-972 87 Luleå
E-mail: jonny.nilimaa@ltu.se

Thomas Blanksvärd
M.Sc., Ph.D., Ass. Professor
Luleå University of Technology
SE-972 87 Luleå
E-mail: thomas.blanksvard@ltu.se

Lennart Elfgren
M.Sc., Ph.D., Emer. Professor
Luleå University of Technology
SE-972 87 Luleå
E-mail: lennart.elfgren@ltu.se

ABSTRACT

To meet new demands, existing bridges might be in need for repair, upgrading or replacement. To assist such efforts a 55-year-old post-tensioned concrete bridge has been comprehensively tested to calibrate methods for assessing bridges more robustly. The programme included strengthening, with two systems based on carbon fibre reinforced polymers (CFRPs), failure loading of the bridge's girders and slab, and determination of post-tension cables' condition and the material behaviour. The complete test programme and related instrumentation are summarised, and some general results are presented. The measurements address several current uncertainties, thereby providing foundations for both assessing existing bridges' condition more accurately and future research.

Key words: Assessment, bridges, carbon fibre reinforced polymer, concrete, destructive test, ductility, flexure, full-scale test, monitoring, near-surface mounted reinforcement, non-destructive test, prestressed laminates, post-tension, punching, robustness, shear, strengthening, structural behaviour.

1 INTRODUCTION

In order to meet current and future demands for sustainability and structural resistance, existing bridges might be in need for repair, upgrading or replacement. For instance, responses to a questionnaire by infrastructure managers in 12 European countries, acquired and analysed in the *MAINLINE* project, indicated a need for strengthening 1500 bridges, replacing 4500 bridges and replacing 3000 bridge decks in Europe during the coming decade [1]. The Swedish Government Proposal 2012/13:25 recommended an investment of SEK 522 billion (EUR 60.4 billion) from 2014 to 2025, to meet transport infrastructure requirements in Sweden [2]. With adjustment for inflation this represents a 20 % increase relative to the previous investment level, as detailed in Prop. 2008/09:35 [3], indicating a need for substantial actions to maintain robust and sustainable infrastructure. Due to budgetary constraints and the major social, economic and environmental benefits of avoiding demolition and reconstructing existing bridges [4], they should be repaired and strengthened rather than replaced in cases where this is cost-effectively feasible [5]. Thus, advanced methods should be used for accurately assessing bridges' condition [6], and identifying the optimal operations to maintain, strengthen or replace them, from a perspective based on life-cycle cost minimisation [7].

To obtain reliable assessments of existing bridges, which are crucial for rigorous life-cycle cost analysis, it is essential to address current uncertainties regarding key variables, such as structural and loading parameters and possible deterioration mechanisms [8]. In the past decade monitoring concepts have been developed to update models for bridge assessment, reducing the uncertainties, based on empirical data [9]. Moreover, proof loading has been suggested [10], and subsequently implemented for reinforced concrete structures in ACI Standard 437.2-13 [11], as an approach to verify the reliability of relevant models and reduce uncertainties regarding the true condition of existing bridges. Thus, testing and monitoring of bridges at service-load levels is an accepted and well-known approach for assessment.

Detailed, large-scale laboratory tests of bridges and their materials have been reported, e.g. [12] and [13]. Destructive investigations of prestressed concrete [14], post-tensioned concrete [15-16] and non-prestressed reinforced concrete bridges [17-22] have also been described. However, such studies have generally focused on specific components or elements, for instance, the bridge slab [15]. Few complete full-scale bridges have been tested to failure in order to improve understanding of their true structural behaviour, and rigorously calibrate methods and models. Hence, more comprehensive empirical information on the behaviour of concrete bridges, especially of prestressed and post-tensioned concrete, as they approach failure, and cost-effective methods to avoid risks of failure, is required.

Thus, in the study presented here a 55-year-old post-tensioned concrete bridge was thoroughly instrumented (with up to 141 sensors) and tested to failure. The aims were to calibrate and refine methods and models for assessing existing reinforced concrete bridges, and to assess the utility of methods using carbon fibre reinforced polymers (CFRPs) for upgrading reinforced concrete structures [23]. Since there have been few full-scale tests on post-tensioned bridges, a particular focus was on assessment of the post-tensioned system. The complete test and measuring programme is described here, and selected general results to provide insights about the tests. More detailed results will be presented later.

2 THE KIRUNA BRIDGE

2.1 General description

The Kiruna Bridge, located in Kiruna, Sweden, was a viaduct across the European route E10 and the railway yard close to the town's central station (Figure 1). It was constructed in 1959 as part of the road connecting the city centre and the mining area owned by LKAB. The sub-level caving method for extracting the ore causes subsidence. Thus to ensure the continuing utility of the Kiruna Bridge, in 2006 LKAB initiated geodetic position measurements of the bridge supports. In 2008 Luleå University of Technology (LTU) started to monitor the bridge continuously [24]. Due to ongoing subsidence, LKAB decided to permanently close the bridge in October 2013 for demolition in September 2014, providing an opportunity for LTU to test it to failure in May-August 2014.

Figure 1 – Photograph of the Kiruna Bridge from the north-east, showing the slag heap from the LKAB iron ore mine in the background (2014-06-25).

2.2 Geometry

The bridge was a 121.5 m continuous post-tensioned concrete girder bridge with five spans: 18.00, 20.50, 29.35, 27.15 and 26.50 m long (Figure 2). According to construction drawings both the longitudinal girders and bridge slab in the western part (84.2 m) were supposed to be curved with a radius of 500 m. However, inspection of the actual geometry showed that the slab's girders consisted of straight segments with discontinuities at the supports. Moreover, there were 5.0 % and 2.5 % inclinations in the longitudinal and transverse directions, respectively.

Longitudinal movements of the bridge were allowed at the eastern abutment by three rolling bearings (support 6 in Figure 2), but not the western abutment (support 1). Devices were installed at the bases of the intermediate supports 2-5, each consisting of three columns, in 2010 to enable vertical adjustment of the supports to counter uneven settlement of the basements.

The superstructure consisted of three parallel, 1923 mm in height, longitudinal girders connected with a slab on top (Figure 3). Including the edge beams the cross-section was 15.60 m
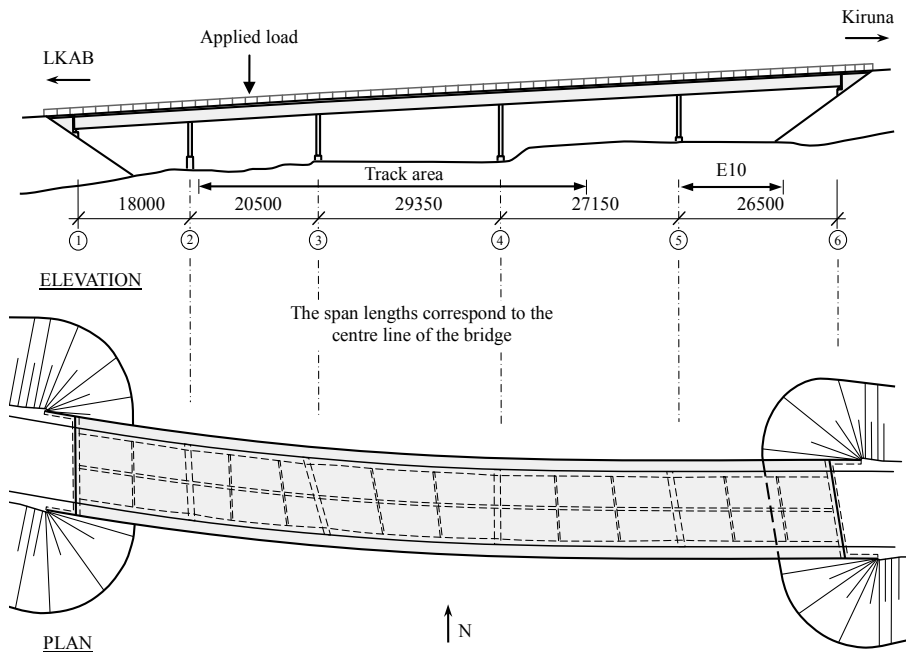
Figure 2 – Geometry of the Kiruna Bridge and location of the load application in the test programme.
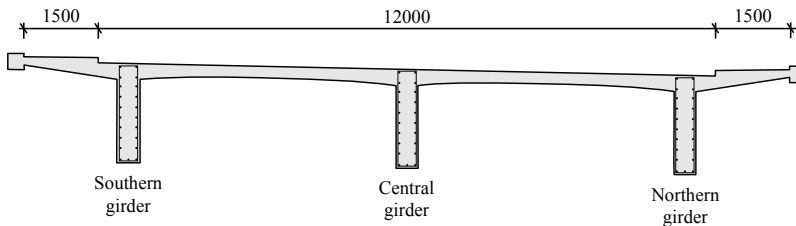
Figure 3 – Cross-section of the Kiruna Bridge.

wide, and the free distance between the girders was 5.00 m. In the spans the girders were 410 mm wide, gradually increasing to 650 mm 4.00 m from the intermediate supports and widened to 550 mm at anchorage locations of the post-tensioned cables, two fifths of the span lengths west of support 3 and three tenths of the span length east of support 4. The bridge slab was 300 mm thick at the girder-slab intersection and 220 mm 1.00 m beside to the girders.

The Kiruna Bridge was post-tensioned in two stages with the BBRV system. In the first stage, six cables per girder were post-tensioned in each end of the central segment. In the second stage, four and six cables per girder were post-tensioned from the free end of the western and eastern segments, respectively. Each cable was composed of 32 wires with a 6 mm diameter.

The girders were each reinforced with three 16 mm diameter bars at the bottom, and 10 mm diameter bars at the sides with either 150 mm spacing for the central girder or 200 mm for the others. The vertical reinforcement also consisted of 10 mm diameter steel bars with 150 mm spacing. The concrete cover was 30 mm thick, except for the 16 mm diameter reinforcement bars, for which the horizontal concrete cover was 32 mm thick.

Before the tests the pavement on the slab was removed from the road crossing the bridge. The bridge was originally designed according to *Provisional Regulations of the Royal Civil Engineering Board* issued in 1955 [25].

2.3   Material

According to construction drawings the concrete quality in the substructure and the superstructure was K 300 and K 400, respectively, while the reinforcing steel quality was generally Ks 40, except in the bridge slab (Ks 60). The steel quality for the post-tensioned reinforcing BBRV reinforcing system was denoted St 145/170. The bridge was constructed in accordance with the *National Steel Regulation* [26] and *National Concrete Regulation* [27], issued in 1938 and 1949, respectively.

3   TEST PROCEDURE

3.1   General description

An experimental programme was designed to assess the behaviour and load-carrying capacity of the bridge using both non-destructive and destructive test procedures. For safety reasons, related to continuing use of the European route E10 during the tests, the experimental programme was developed for loading in span 2-3, with associated monitoring in spans 1-4 (Figure 2). The experimental programme can be summarised by the following, chronological steps:

1. Non-destructive determination of residual post-tensioned forces in cables in span 2-3 (May 27-28, 2014).
2. Preloading Test Schedule 1, of unstrengthened bridge girders, including destructive determination of residual post-tensioned forces in cables in span 2-3 (June 15-16, 2014).
3. Preloading Test Schedule 2, of strengthened bridge girders (June 25, 2014).
4. Failure test of the bridge girders (June 26, 2014).
5. Failure test of the bridge slab (June 27, 2014).
6. Complementary non-destructive determination of residual post-tensioned forces in cables in midspans 1-4 (June 27 and August 25, 2014).
7. Material tests of concrete, reinforcing steel and post-tensioned steel.
8. Condition assessment of post-tensioned cables.

Steps 1-6 were carried out at the Kiruna Bridge, with the test dates in parenthesis. However, steps 7-8 are planned to take place in the Complab laboratory at LTU after demolition of the bridge.

3.2   Strengthening

The experimental programme included tests of two separate systems for strengthening concrete structures using carbon fibre reinforcing polymers, which were attached to the lower sides of the central and southern girders in span 2-3 (see Figure 4 and Figure 10). However, the northern girder remained unstrengthened.

A system of three near-surface mounted (NSM) 10x10 mm^2 CFRP rods was installed in the concrete cover of the central girder [6, 28]. The bar lengths were limited to 10.00 m, due to transportation constraints, thus several overlaps (1.00 m) were required to apply the strengthening over the entire span length. A set of full-length CFRP rods was installed centrically in span 2-3, with sets of 5.80 and 5.74 m CFRP rods on the western and eastern sides, respectively

To strengthen the southern girder, a system of three 1.4x80 mm^2 prestressed CFRP laminates was applied to the blasted concrete surface [29-30]. The lengths of the middle and outer laminates were 14.17 and 18.91 m, respectively, in order to provide space for the anchorage device at each end. Each laminate was tensioned to 100 kN at the eastern end, controlled with a load cell, as the force was applied using a manually operated hydraulic jack. The force was gradually transferred to the concrete by the anchorage device. In this manner no force is expected to be transferred at the end, while it is fully transferred after 1.20 m. The anchorage devices were attached to the bridge until disassembly after Preloading Test Schedule 2. This experimental programme was the first reported full-scale installation and test of the strengthening method using prestressed laminates with these innovative anchor devices.

For the CFRP rods and laminates, denoted StoFRP Bar IM 10 C and, StoFRP Plate IM 80 C respectively, the mean modulus of elasticity and tensile strength were 210 GPa (200 GPa) and 3300 MPa (2900 MPa), respectively, with mean values specified in parenthesis. Epoxi StoPox SK41, a commercially available and CE-approved thixotropic epoxy adhesive, was used to bond both strengthening systems.
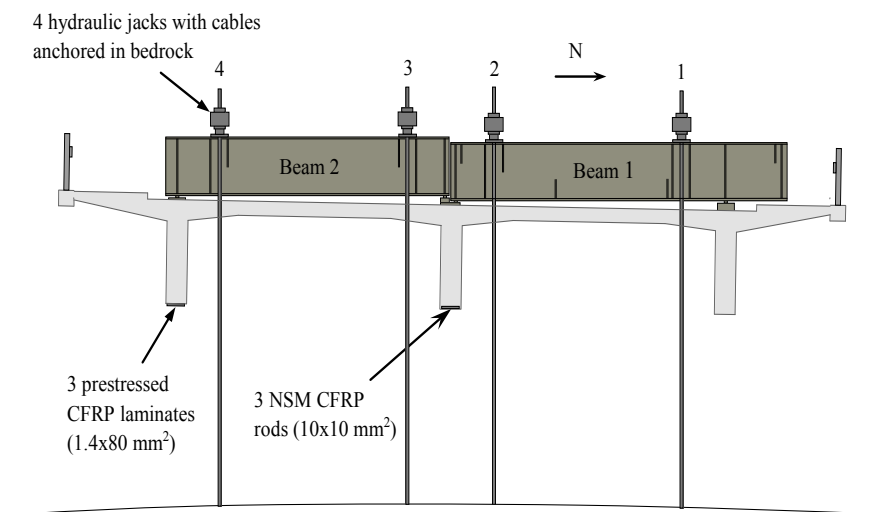

Figure 4 – Arrangement for loading the bridge girders in midspan 2-3.

3.3 Preloading

In span 2-3 two welded steel beams (outer dimensions 700x1180x5660 and 700x1180x6940 mm^3) were arranged horizontally to apply loads in the midspans of each girder, see Figure 2 and Figure 4. They consisted of a double web (thickness 15 mm) with flanges (thickness 30 mm) and were of the steel grade S355J0. The beams were supported by steel load distribution plates (steel grade S275JR), with areas of 700x700 mm^2 and total thicknesses ranging from 20 to 265 mm, due to the inclination of the bridge slab. A horizontal concrete surface was also cast locally under the plates. The bridge was loaded using four hydraulic jacks with cables, threaded through drilled holes in the bridge slab, anchored over a length of 14.60 m in the bedrock, as illustrated in Figure 4. The distances from the centre of the jacks and cables to the centre of the support of the transverse steel beam were 885 mm. The capacity of the jacks was approximately 7.0 MN, with a 150 mm stroke length. The piston cross-section area was 1282 cm^2 for jacks 1, 3 and 4, and 1284 cm^2 for jack 2. Each cable consisted of 31 wires with 15.7 mm diameter.

The bridge was preloaded by applying two schedules of incrementally increasing loads using the four jacks to both strengthened and unstrengthened girders in midspan 2-3, as listed in Table 1 and illustrated in Figure 4. The schedules were designed to reach the cracking load of the girders, as predicted by preliminary nonlinear finite element analysis. Before the force-controlled loading to a specified level, given by the actual load case, the bridge was unloaded. To ensure no drift in the measurements and stable loading, peak pressure was maintained for load cases 7, 9, 13 and 29. Load cases 15-18 in Schedule 1 were designed to determine the remaining forces in the post-tensioned cables (see Section 3.6).

3.4 Bridge girder failure test

Preloading was followed by a test to failure of the strengthened girders, according to the setup described in the previous section. Each girder was equally loaded to 12.0 MN in total (the approximate load-carrying capacity predicted by preliminary nonlinear finite element analysis): 4.0 MN delivered by the outer jacks and 2.0 MN by the inner jacks. The pressure in jack 4 was subsequently increased to failure of the southern girder and then the pressure in jacks 2 and 3 was increased to failure of the central girder, while the settings of the other jacks remained unchanged so they provided approximately constant loads. The jacks' grip positions were changed as necessary to accommodate deflections exceeding the stroke length.

3.5 Bridge slab failure test

The bridge slab in midspan 2-3 was tested to failure using an arrangement similar to load model 2 (LM 2) described in Eurocode 1 [31], with its centre located 880 mm from the outer side of the northern girder (Figure 5). By rotating steel beam 1 (Figure 4 and Figure 5), hydraulic jack 1 was reused to apply load on the slab, through two 350x600x100 mm^3 steel plates spaced 2.00 m apart. A horizontal concrete surface was also cast locally under the plates. Due to the widening of the bridge girders at the anchorages of the post-tensioned cables, the distances from the centres of the western and eastern load distribution plates to the inner sides of the girders were 470 and 330 mm, respectively. As in the previous tests, the loading was force-controlled.

3.6   **Assessment of post-tensioned cables**

The residual force in the post-tensioned cables was non-destructively determined by monitoring strains at the lower surface of each girder resulting from gradually cutting the concrete with a saw on both sides of a strain sensor [32] placed one-tenth of the span length west of midspan 2-3, before the bridge and slab failure tests. After the failure tests, the procedure was also applied to each girder in midspan 1-2, the northern girder in midspan 2-3 and the central and southern girders in midspan 3-4. In order to keep the reinforcing steel intact, the arrangements of sensors

Table 1 – Load cases for preloading the unstrengthened and strengthened bridge girders in midspan 2-3.

Load case	Jack 1 kN	Jack 2 kN	Jack 3 kN	Jack 4 kN
1[1,2]	500	250	250	500
2[1,2]	500	500	-	-
3[1,2]	-	-	500	500
4[1,2]	1000	1000	-	-
5[1,2]	-	-	1000	1000
6[1,2]	1500	1500	-	-
7[1,2]	1500	1500	-	-
8[1,2]	-	-	1500	1500
9[1,2]	-	-	1500	1500
10[1,2]	500	250	250	500
11[1,2]	1000	500	500	1000
12[1,2]	1500	750	750	1500
13[1,2]	1500	750	750	1500
14[1,2]	2000	1000	1000	2000
15[1,2]	2000	1000	1000	2000
16[1,2]	2000	1000	1000	2000
17[1]	2000	1000	1000	2000
18[1]	2000	1000	1000	2000
19[1]	500	500	-	-
20[1]	-	-	500	500
21[1]	1000	1000	-	-
22[1]	-	-	1000	1000
23[1]	1500	1500	-	-
24[1]	-	-	1500	1500
25[1]	500	250	250	500
26[1,2]	1000	500	500	1000
27[1,2]	1500	750	750	1500
28[2]	2000	1000	1000	2000
29[2]	2000	1000	1000	2000

[1] Load case for preloading the unstrengthened girder

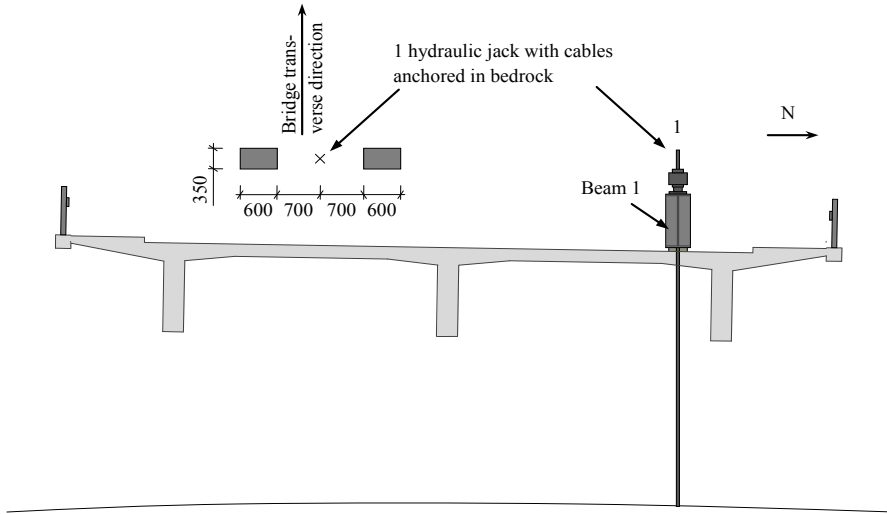[2] Load case for preloading the strengthened girder

Figure 5 – Arrangement for loading the bridge slab in span 2-3.

and saw cutting lines were designed to avoid cutting either the stirrups or longitudinal reinforcing steel. The cutting proceeded to an approximate depth of 35 mm, or the actual depth of the longitudinal reinforcing steel. All the non-destructive tests were carried out without applying external loads.

As part of Preloading Test Schedule 1, the cracking moment test [33] was applied to calibrate the non-destructive test method. During load cases 1-14 cracks formed, and instruments described in the next section were used to monitor the behaviour of selected cracks and adjacent areas between load cases 14 and 15. Thus, the remaining force in the post-tensioned cables can be determined from data acquired from load cases 15-18, based on the sequence of reopening of the cracks.

Further laboratory assessments of the condition of both the cables and their grouting are planned.

3.7 Material tests

To determine characteristics of the bridge's materials, tests of the concrete, reinforcing steel and post-tensioned steel are also planned. Thus, before the tests described here at least six concrete cylinders were drilled out from the superstructure in both midspans 1-2 and 3-4, and each of the columns at support 4. In addition, during demolition of the bridge several 10, 16 and 25 mm diameter steel bars, and a specimen of the post-tensioned cables, were obtained for uniaxial tensile tests.

4 INSTRUMENTATION

4.1 General description

To evaluate the bridge's behaviour a comprehensive measuring programme was designed. This section summarises the instrumentation used to measure changes in monitored variables during the bridge girder and slab tests and the non-destructive tests with no external load. In addition, measurements during strengthening were carried out according to the description in previous section.

Before initiating any experimental investigation existing cracks in the entire span 2-3 and the half-spans 1-2 and 3-4 adjacent to the loaded span were mapped. The focus was on cracks in the girders, the crossing beams and the slab at the loading point. In order to follow the formation of cracks, the mapping was repeated after each test sequence. The cracks were mapped manually and their widths were not measured, apart from several cracks specified in the measuring programme.

In addition to the monitoring during bridge loading, long-term measurements were carried out during the nights before Preloading Test Schedules 1-2 and the failure test of the girders. The durations of the monitoring on these occasions were 22398, 21613 and 45558 s, respectively, and the same instrumentation was used as in the followed bridge loading, excluding manual measurements. Moreover, the bridge was examined when the anchorage device for the prestressed CFRP laminates was disassembled.

Most measurements of the bridge were generally acquired at a sampling frequency 5 Hz, except for the long-term measurements (1 Hz).

4.2 Girder test

A battery of instruments was installed before the tests of the longitudinal bridge girders to obtain as comprehensive measurements as possible, within budgetary constraints, of the resulting forces, displacements, curvatures, strains and temperatures. These measurements were complemented by monitoring using several video and still cameras. Data were acquired from all the instrumentation described in this section during the full programme of tests of the bridge girders unless otherwise stated.

Force
The applied load on the structure was measured by monitoring the oil pressure in each hydraulic jack (1-4), illustrated in Figure 4, using UNIK 5000 sensors (GE Measuring and Control; A5075-TB-A1-CA-H1-PA), which have a measuring range between 0 and 600 bar.

Displacement
Displacements of the bridge were measured using the following instruments. Draw-wire displacement sensors (MICRO-EPSILON; WDS-500(1000)-P60-CR-P) were installed to measure deflections at positions 1-10 and 13-15 (Figure 6): in midspan 2-3 on the lower sides of the girders, and lower sides of the crossing beams 500 mm from the outer columns (positions 4-5 and 9-10). All these sensors had a measuring length of 500 mm except those used at positions 6-8 (1000 mm). Twisted lines connected each sensor to a reference point on the ground or the basement.
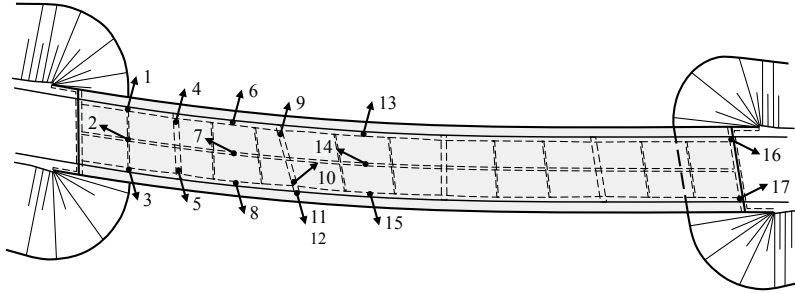
Figure 6 – Positions of bridge displacement sensors.

At positions 11 and 12 both the longitudinal and transverse displacement were monitored using Noptel PSM-200 sensor. The reference point for the horizontal displacement of the bridge slab at the centre line of support 3 was 150 mm perpendicularly away from the southern side of the basement. A transmitter was installed on the basement and a receiver on the lower side of the bridge slab, oriented vertically to the transmitter. The Noptel PSM-200 sensors were only active during the failure test of the bridge girders.In addition, the displacement of the basements' upper side at support 2-3 was manually measured during the girder failure test, 500 mm against the centre of the bridge in transverse direction, in relation to positions 4-5 and 9-10, and the reference point was an unaffected point beside the bridge. For safety reasons, the incremental monitoring proceeded until a certain load was reached, 9.0 MN in total.

At positions 16-17 (Figure 6) longitudinal displacements of the upper part of the rolling bearings, i.e. the lower side of the girders, was measured using linear displacement sensors (Micro-Measurements; HS 100) with a 102 mm measurement range, and positions in the abutment as reference points.

In Preloading Test Schedule 1, load cases 15-27, the width of one crack in the centre of the lower side of each girder (110, 910 and 1380 mm east of midspan for the northern, central and southern girders, respectively) was measured, using crack opening displacement sensors (EPSILON; 3541-010-150-ST) with the measuring range of 10 mm. Data were also acquired from the sensor on the girder strengthened with laminates during Preloading Test Schedule 2 and the bridge girder failure test.

Curvature
The curvature at support 2, support 3 and midspan 2-3 was measured over distances of 4.82, 5.08 and 5.00 m, respectively, using rigs composed of steel beams, supported at the ends, and five linear displacement sensors with 800 mm spacing based. At the supports the rigs were located on the bridge slab, while the midspan rig was located under the girder. Due to the discontinuities at the supports, i.e. changes in directions of the girder, and straightness of the curvature rigs, the instrumentation was installed along the line of the central girder in span 2-3. The sensors were HS 100, HS 50 and HS 25 instruments (Micro-Measurements) with measurement ranges of 102, 51.5 and 26 mm, respectively, set at the positions increasingly distant from the centre of the rigs.

Strain

Strain gauges supplied by Kyowa were installed on the longitudinal and vertical reinforcing steel bars, CFRP rods and laminates, and the concrete surfaces of both the columns at supports 2-3 and next to some major cracks during Preloading Test Schedule 1, load cases 15-27. All of these gauges had 120 ohm resistance, and those installed on the longitudinal reinforcing steel, stirrups or CFRPs and concrete had measuring lengths of 10, 5 and 60 mm, respectively (KFG-10-120-C1-11L1M3R, KFG-5-120-C1-11L1M3R, KC-60-120-A1-11L1M3R). In total, 35 strain gauges were systematically arranged on the longitudinal reinforcing steel bars: at sections A-K in Figure 7 and cross-section positions 1-12 in Figure 8, 1879 mm from the centre lines of the supports on each side (B and J), and 1433 and 2226 mm from each side of midspan 2-3. The locations of the sections were at angles of 45° to the centre line of the supports and 60° and 45°, respectively, to the load distribution plates. On the reinforcement bars they were installed in the corners of the closed stirrups (Figure 8) except at positions 2, 5, 8 and 11, where they were located 1248 mm from the lower side of the girders. All the strain gauges, apart from those in the bridge slab, were placed on the side of the girders.

The locations of the sensors for each section and cross-section position, are specified in Table 2. Due to the greater width of the girder in sections G-H and the corresponding increase in concrete cover strain gauges 25-28 were not used in the final measuring programme. Care was taken to avoid damaging the girder in any way that could potentially affect the quality of the
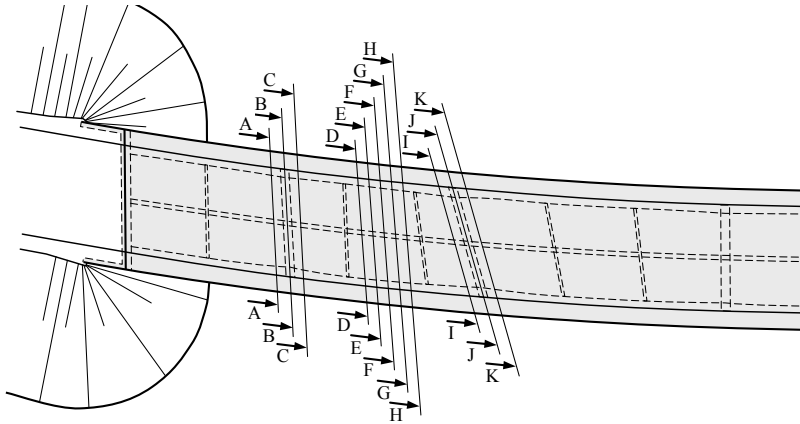

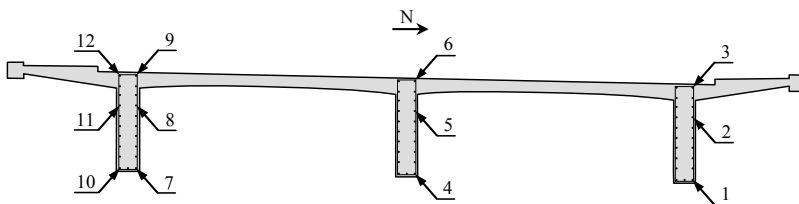Figure 7 – Positions of strain gauges on longitudinal reinforcing steel.

Figure 8 – Cross-section positions of strain gauges on longitudinal reinforcing steel.

Table 2 – Positions of strain measurements on longitudinal reinforcing steel.

No.	Position[1]	No.	Position[1]	No.	Position[1]
1	A6	14	E4	27	H4
2	A12	15	E7	28	H7
3	B1	16	F1	29	I6
4	B2	17	F2	30	I12
5	B3	18	F3	31	J1
6	B6	19	F4	32	J2
7	B10	20	F5	33	J3
8	B11	21	F6	34	J6
9	B12	22	F7	35	J10
10	C6	23	F8	36	J11
11	C12	24	F9	37	J12
12	D4	25	G4	38	K6
13	D7	26	G7	39	K12

[1] Section A-K in Figure 7 and cross-section position 1-12 in Figure 8

strengthening.

As illustrated in Figure 9, strain gauges were also installed in three lines on the vertical reinforcing steel on the northern side of the southern girder in span 2-3, at 900 mm spacing starting from the edge of the loading plate. Thus strain gauges 6-9 were located 1250 mm from the central point of the load application. Vertical distances from the bottom side of the girders to the sensors were 148, 548, 948 and 1348 mm, respectively.

In addition, an ARAMIS system in 5M configuration was used to optically record deformations of the surface on the southern girder on the opposite side to the instrumentation of the vertical reinforcing steel, and accompanying software was utilised to analyse the strains. The optical monitoring was based on a grid, centred 2.0 m west of midspan 2-3, from the bottom of the
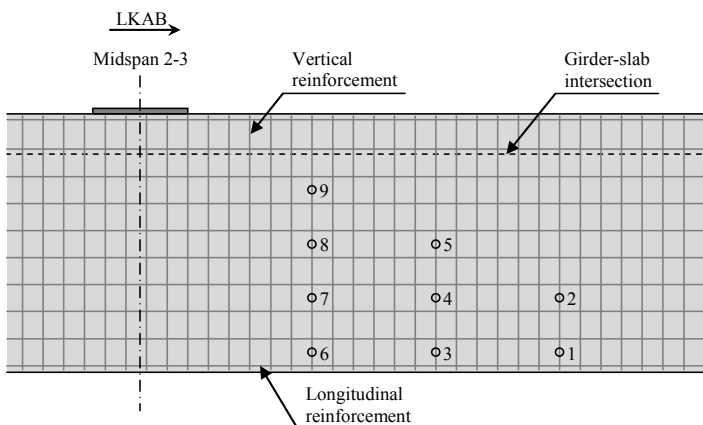

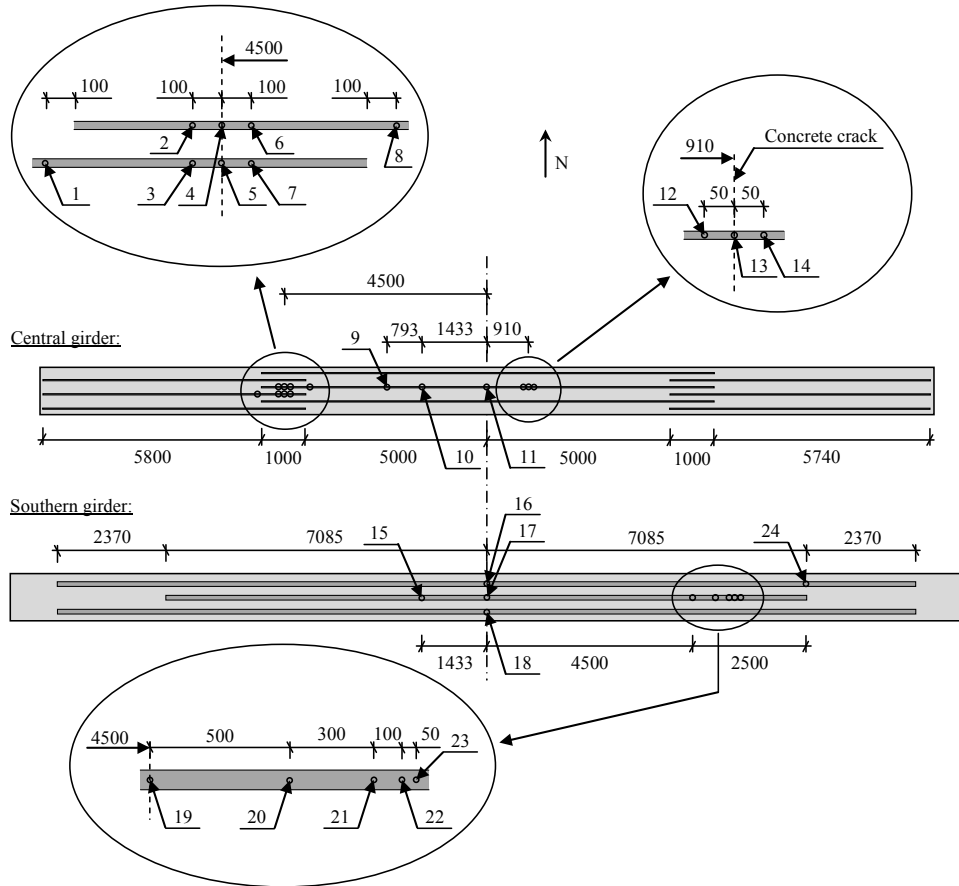*Figure 9 – Positions of strain gauges on vertical reinforcing steel.*

Figure 10 – Geometry of bridge strengthening systems in span 2-3 and positions of the strain gauges on the NSM CFRP rods and prestressed CFRP laminates.

girder. Thus, strain gauges 3-4 according to Figure 9, on the opposite side of the girder, were located within the monitored area, which theoretically covered 1050x880 mm.

In total 14 strain gauges were installed on the NSM CFRP rods and 10 on the prestressed CFRP laminates (Figure 10): gauges 1-8 recorded the strain at the western edge of the NSM strengthening; 9, 10 and 15 were located in the sections equipped with strain gauges on longitudinal reinforcing steel; 11 and 16-18 at midspan 2-3; 14-16 at major concrete cracks and 19-24 next to the anchorage of the laminates.

To obtain the reaction forces in the columns adjacent to the load application in midspan 2-3, i.e. supports 2 and 3, the concrete strains were measured by installing a sensor 800 mm above the bottom in the centre of each side of each column. Before the bridge tests, the methodology of using strain gauges to determine the reaction forces was validated using load cells, while

preloading the column with hydraulic jacks and utilising the column's vertical adjustment device.

On each side of the cracks instrumented by crack opening displacement (COD) sensors as described above, the concrete strains were measured. Like the COD sensors, the strain gauges were located in the centre of the lower side of the girders. These sensors were only active in Preloading Test Schedule 1, load cases 15-27.

Temperature
During the experiments temperatures were measured at several locations in midspan 2-3 (Figure 11), using type T (04 N/N-24-TT) temperature wires inserted into holes to specified depths in relation to the concrete surface: 30 mm for positions 1, 3 and 6; 60 mm for positions 2 and 7; 50 mm for positions 4 and 8; and 80 mm for position 5.
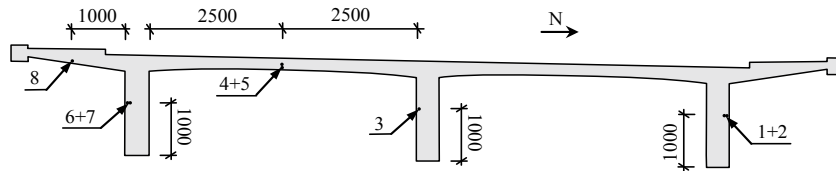

Figure 11 – Positions of temperature wires in the concrete at midspan 2-3.

4.3   Slab test

Relevant instrumentation that was still intact after the girder failure tests, and complementary instrumentation, was used to monitor the behaviour of the bridge during the following bridge slab failure test. The sensors still active during this test were:

- the oil pressure sensor for hydraulic jack 1, as shown in Figure 4 and Figure 5,
- draw-wire sensors 4-7 and 14-15, as shown in Figure 6;
- strain gauges 1-39 as specified in Table 2, excluding gauges 12, 17 and 24-28, which were not used for various reasons;
- strain gauges 1-9 as shown in Figure 9, except gauge 8, which was out of order;
- strain gauges 1-24 installed on the columns at supports 2 and 3;
- temperature wires 1-8, as shown in Figure 11.

Displacement
The above instrumentation was complemented with four draw-wire sensors, with similar specifications to the sensors utilised in previous tests. Two were located on the lower surface of the slab, at the centre of the load applications, to measure deflections, and two on the lower side of the northern longitudinal girder, in both cases 2.00 m on either side from midspan 2-3.

Curvature
To monitor curvature in the slab test the rigs used in the girder tests at supports 2 and 3 were installed on the top surface of the slab, parallel to the steel beam used for load application, 500 and 1000 mm southern to the centre of the loading plates. The midpoint of this instrumentation coincided with midspan 2-3.

4.4   Non-destructive test

Three strain gauges of the same type as previously specified for monitoring the concrete were used in the non-destructive tests to determine the residual forces in the post-tension cables, located in a line in the centre of the lower sides of each girder in span 2-3. In order to provide enough space to avoid damaging the sensors while cutting the concrete, the centre-centre distance was 120 mm, since the total length of the strain gauges was 74 mm with a 60 mm measuring length.

5   RESULTS

5.1   General description

In the experimental programme for the girder tests the bridge was instrumented with sensors at up to 141 positions in total, excluding the surface measurement using ARAMIS, and 93 sensors were used in the bridge slab failure test. General observations regarding the test procedures and the observed load-carrying capacity of the bridge are presented in this section.

5.2   Girder test

The loads applied in the preloading schedules and loading the bridge to failure, according to the recorded pressures in the hydraulic jacks, are illustrated in Figure 12 to Figure 14, which show that the preloading followed the schedules listed in Table 1, with minor deviations due to difficulties in manually controlling the oil pressure. In Preloading Test Schedule 1 (Figure 12) the complementary instrumentation used to determine the remaining forces in post-tensioned cables was installed after approximately 7400 s. The time spent installing it (about 5.5 hours including associated operations) is not shown in the graph, but no corrections have been applied to the force-time courses shown in Figure 13.
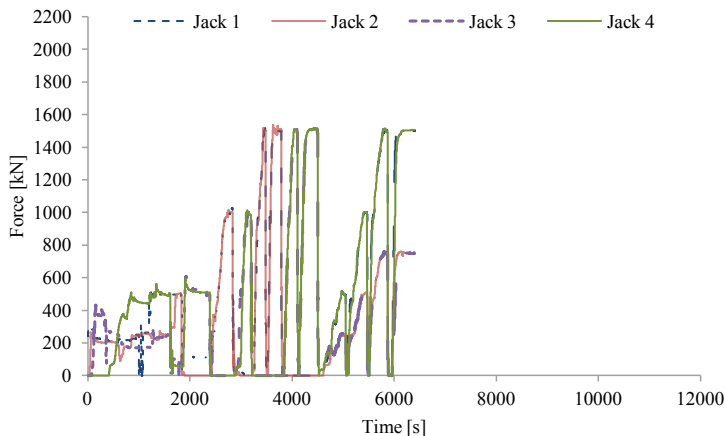

Figure 12 – Observed loadings during Preloading Test Schedule 1, unstrengthened girder.
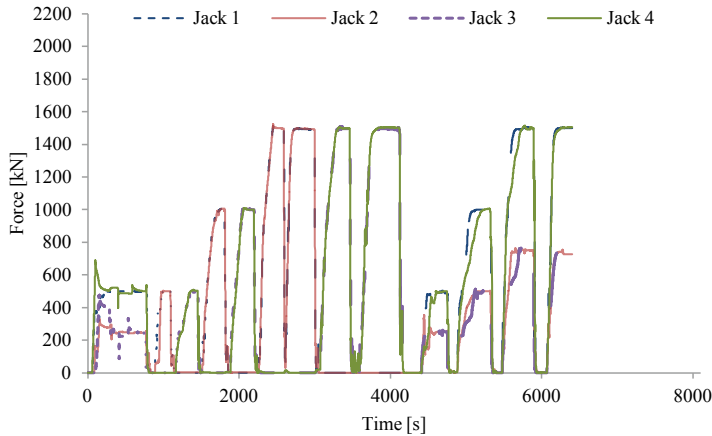
Figure 13 – Observed loadings during Preloading Test Schedule 2, strengthened girders.
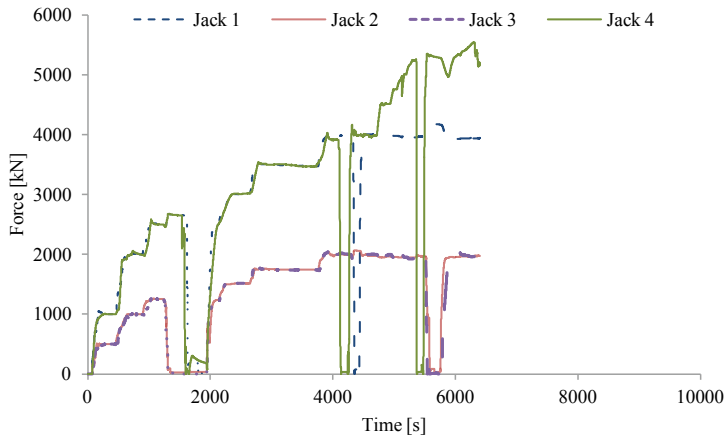
Figure 14 – Observed loadings during the bridge girders failure test.

In order to manually follow the basement settlements of the bridge safely, the loading was carried out stepwise up to a certain level, see Figure 14. Another reason for the irregularity in the loading procedure was the limited stroke length of the hydraulic jacks, which required the grip position to be changed several times to accommodate longer deflections of the bridge.

After applying a total load of 12.0 MN (4.0 MN for each girder), the pressure in jack 4 was increased to reach failure of the southern gird§er, while the pressure in the other jacks remained nearly constant. However, the pressure in jacks 1 and 4 slightly decreased as the central girder was loaded to failure using jacks 2-3, in responses related to the deformations of the bridge.

Deflections of the bridge are illustrated by the load-displacement curve in Figure 15, showing the relationship between the total load and midspan deflection of the central girder. Figure 15

also presents the behaviour according to finite element analysis with 2D and 3D idealisation in the software ATENA and ABAQUS, respectively. Unfortunately, draw-wire sensor 8 (Figure 6), was damaged during the test, so the midspan deflection of the southern girder is not available for the entire test. The highest loads the longitudinal southern and central girders were subjected to induced deflections of 136 and 159 mm, respectively (Figure 15). However, the bridge loading was further continued. The shapes of the girders after the test are shown in the photograph in Figure 16. The peak load at loading the southern girder to failure was 13.4 MN (5.5 MN in jack 1) and 12.7 MN for the central girder (6.1 MN in total in jacks 2-3).

5.3   **Slab test**

The data acquired from the specified test setup indicate that the load-carrying capacity of the bridge slab was 3.32 MN. Thus, the load transferred in each loading plate was 1.66 MN. The slab failed only at the western load distribution plate, displaying very brittle behaviour with no
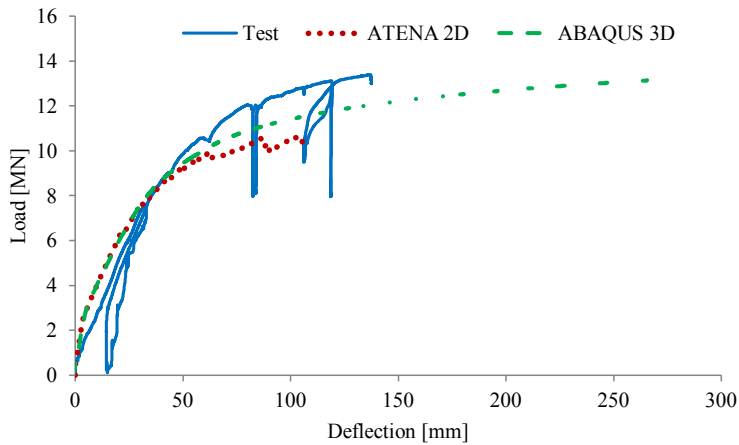

Figure 15 – Load-displacement relationship during the bridge girder failure test.

Figure 16 – Photograph of the bridge girders after failure, view from the south (2014-08-26).

Figure 17 – Photograph of the bridge slab failure, view from south (2014-06-27).

appreciable indication of the failure. In Figure 17 the final shape of the bridge slab is presented from underneath the bridge. Due to the arrangement of the test setup and type of failure it was not possible to further load the slab to achieve failure at the eastern load distribution plate.

6   CONCLUSIONS

Closure of the Kiruna Bridge provided a rare opportunity for LTU to monitor a post-tensioned concrete bridge during tests to failure using a wide array of instruments, from May to August 2014. The primary aim was to acquire relevant data for calibration and development of methods for assessing prestressed and post-tensioned concrete structures. The results acquired during the investigations reported in this paper suggest that the following parameters warrant further attention:

- Robustness, ductility and bridge behaviour;
- Shear resistance at ultimate limit state;
- The utility, behaviour and contributions to increases in capacity of strengthening methods using CFRPs;
- Punching resistance of bridge slabs;
- Condition of post-tensioned steel cables and non-destructive determination of residual forces;
- Reliability-based analysis of reinforced concrete structures;
- Finite element model updating.

Detailed analyses of these parameters would greatly facilitate improvements in models for assessing existing concrete structures and thus savings of costs, for bridge owners and managers.

7   ACKNOWLEDGEMENT

8   REFERENCES

1. MAINLINE Consortium, "Benchmark of new technologies to extend the life of elderly rail infrastructure," Deliverable 1.1, 2013, 77 pp. (Available at: http://www.mainline-project.eu).
2. Reinfeldt, F., Elmsäter-Svärd, C., "Government proposition 2012/13:25: Investments for a strong and sustainable transportation system [Regeringens proposition 2012/13:25: Investeringar för en starkt och hållbart transportsystem]," Prop. 2012/13:25, Ministry of Enterprise, Energy and Communications, Stockholm, Sweden, 2012, 220 pp. (In Swedish).
3. Reinfeldt, F., Torstensson, Å., "Government proposition 2008/09:35: Future travel and transport – infrastructure for sustainable growth [Regeringens proposition 2008/09:35: Framtidens resor och transporter – infrastruktur för hållbar tillväxt]," Prop. 2008/09:35, Ministry of Enterprise, Energy and Communications, Stockholm, Sweden, 2008, 232 pp. (In Swedish).
4. Power, A., "Does demolition or refurbishment of old and inefficient homes help to increase our environmental, social and economic viability?" *Energy Policy*, Vol 36, No 12, January 2008, 4487-4501 pp.
5. MAINLINE Consortium, "Assessment methods for elderly rail infrastructure," Deliverable 1.2, 2013, 112 pp. (Available at: www.mainline-project.eu).
6. Sustainable Bridges, "Repair & strengthening of railway bridges: Literature and research report: Extended summary SB6.2," SB6.2, Luleå, Sweden, 2007, 807 pp. Available at: www.sustainablebridges.net).
7. Jalayer, F., Asprone, D., Prota, A., Manfredi, G., "Multi-hazard upgrade decision making for critical infrastructure based on life-cycle cost criteria," *Earthquake Engineering and Structural Dynamics*, Vol 40, January 2011, 1163-1179 pp.
8. Frangopol, D.M., "Life-cycle performance, management, and optimisation of structural systems under uncertainty: accomplishments and challenges," *Structure and Infrastructure Engineering*, Vol 7, No 6, June 2011, 389-413 pp.
9. Frangopol, D.M., Strauss, A., Kim, S., "Bridge reliability assessment based on monitoring," *Journal of Bridge Engineering*, Vol 13, No 3, May 2008, 258-270 pp.
10. Faber, M.H., Val, D.M., Stewart, M.G., "Proof load testing for bridge assessment and upgrading," *Engineering Structures*, Vol 22, No 12, December 2000, 1677-1689 pp.
11. ACI, "Code requirements for load testing of existing concrete structures (ACI 437.2-13) and commentary," ACI 437.2-13, Farmington Hills, Michigan, USA, 2014, pp. 25.
12. Amir, S., "Compressive membrane action in prestressed concrete deck slabs," Doctoral Thesis, Delft University of Technology, Delft, Netherlands, 2014, pp. 314.
13. Nilimaa, J., "Upgrading concrete bridges: Post-tensioning for higher loads," Licentiate Thesis, Luleå University of Technology, Luleå, Sweden, 2013, pp. 302.
14. McClure, R.M., West, H.H., "Full-scale testing of a prestressed concrete segmental bridge," *Canadian Journal of Civil Engineering*, Vol 11, No 3, September 1984, 505-515 pp.
15. Schmidt, J.W., Hansen, S.G., Barbosa, R.A., Henriksen, A., "Novel shear capacity testing of ASR damaged full scale concrete bridge," *Engineering Structures*, Vol 79, November 2014, 365-374 pp.
16. Oh, B., Kim, K., Lew, Y., "Ultimate load behavior of post-tensioned prestressed concrete girder bridge through in-place failure test," *ACI Structural Journal*, Vol 99, No 2, March 2002, 172-180 pp.
17. Jorgensen, J.L., Larson, W., "Field testing of a reinforced concrete highway bridge to collapse," *Transportation Research Record*, Vol 607, September 1976, 66-71 pp.

18. Scanlon, A., Mikhailovsky, L., "Full-scale load test of three-span concrete highway bridge," *Canadian Journal of Civil Engineering*, Vol 14, No 1, February 1987, 19-23 pp.

19. Miller, R.A., Aktan, A.E., Shahrooz, B.M., "Destructive testing of decommissioned concrete slab bridge," *Journal of Structural Engineering*, Vol 120, No, 7, July 1994, 2176–2198 pp.

20. Ross, J.H., "Evaluating ultimate bridge capacity through destructive testing of decommissioned bridges," Master's Thesis, University of Delaware, Delaware, Delaware, USA, 2007.

21. Zhang, J.Q., Ren, H.W., Yu, B., "Failure testing of a full-scale reinforced concrete T-girder bridge," *Advanced Material Research*, Vol 243-249, May 2011, 1767-1773 pp.

22. Puurula, A.M., Enochsson, O., Sas, G., Blanksvärd, T., Ohlsson, U., Bernspång, L., Täljsten, B., Elfgren, L., "Loading to failure and 3D nonlinear FE modelling of a strengthened RC bridge," *Structure and Infrastructure Engineering*, September 2013, 1-14 pp.

23. Bagge, N., "Assessment of concrete bridges: Models and tests for refined capacity estimates," Licentiate Thesis, Luleå Univeristy of Technology, Luleå, Sweden, 2014, pp. 132.

24. Enochsson, O., Sabourova, N., Emborg, M., Elfgren, L., "Gruvvägsbron in Kiruna – Deformation capacity [Gruvvägsbron i Kiruna – Deformationskapacitet]," Division of Structural Engineering, Luleå University of Technology, Luleå, Sweden, 2011, 107 pp. (In Swedish).

25. The Royal Civil Engineering Board, "Provisional regulations of loads and allowed stresses etc. of structures for road and street bridges [Provisoriska föreskrifter för belastningar och tillåtna påkänningar m.m. för konstruktioner till väg- och gatubroar],", Stockholm, Sweden, 1955 , 15 pp. (In Swedish).

26. The Royal Civil Engineering Board, "Standards for steel structures (Steel regulations) [Normalbestämmelser för järnkonstruktioner till byggnadsverk (järnbestämmelser)]," SOU 1938:37, Stockholm, Sweden, 1938, 88 pp. (In Swedish).

27. The Royal Civil Engineering Board, "National concrete regulations – Part 1: The material section [Statliga betongbestämmelser – Del 1: Materialdelen]," SOU 1949:64, Stockholm, Sweden, 1950, 84 pp. (In Swedish).

28. Sustainable Bridges, "Field Tests: Örnsköldsvik Bridge – Full scale testing, Vitmossen: Strengthening of the subsoil, Frövi Bridge – Strengthening & monitoring: SB6.3," SB6.3, Luleå, Sweden, 2007, 181 pp. Available at: www.sustainablebridges.net).

29. Al-Emrani, M., Kliger, R., Haghani, R., "Method for applying a reinforced composite material to a structural member," US 8349109 B2, 2013, 10 pp.

30. Kliger, R., Haghani, R., Mara, V., Mathern, A., "Strengthening of concrete bridge over the river Nossan: New pre-stressing method – evaluation and development," SBUF, ID: 12919, Gothenburg, Sweden, 2014, 33 pp.

31. CEN, "Eurocode 1: Actions on structures – Part 2: Traffic loads on bridges," SS-EN 1991-2:2003, Brussels, Belgium, 2003, 176 pp.

32. Kukay, B., Barr, P.J., Halling, M.W., Womack, K., "Determination of the residual prestress force of in-service girders using non-destructive testing," *Structures Congress 2010*, Orlando, Florida, USA, May 2010, pp. 709-716.

33. Osborn, G.P., Barr, P.J., Petty, D.A., Halling, M.W., Brackus, T.R., "Residual prestress forces and shear capacity of salvaged prestressed concrete bridge girders," *Journal of Bridge Engineering*, Vol 17, No. 2, March 2012, pp. 302-309.

Particle Packing for Concrete Mix Design: Models vs. Reality

Yahya Ghasemi
PhD-student
Div. Structural and Construction Engineering, Luleå University of Technology
S-971 87 Luleå
yahya.ghasemi@ltu.se

Mats Emborg
Professor LTU/Head of R&D Betongindustri AB
971 87 Luleå, Sweden./Betongindustri AB, 100 74 Stockholm, Sweden
mats.emborg@betongindustri .se
mats.emborg@ltu.se

ABSTRACT

The packing density of aggregates is of great importance in concrete mix design as obtaining a higher packing density leads to less usage of cement paste which has technical, environmental and economic benefits. It is thus of interest to model particle packing correctly. Hence, in this study, packing densities of seven mixes of aggregate were attained in the laboratory using the loose packing method and were compared to values suggested by three models: 4C, Compressible Packing Model and Modified Toufar Model. Modified Toufar showed 1.7% mean difference from the laboratory values while CPM and 4C had mean differences of 1.8% and 1.9% respectively. In addition, it was found that some of the models are preferable in certain mixtures.

Keywords: Aggregates, Loose Packing, Mix Design, CPM, 4C, Modified Toufar

1. INTRODUCTION

Aggregate is a major component of the concrete, occupying 60% to 80% of its total volume. Increasing the amount of aggregates corresponds to less usage of cement in the concrete which has several beneficial effects, e.g. reduction in the cost of producing concrete, decrease in most of the durability problems of hardened concrete, reducing shrinkage and cracking, etc.

In addition, reduction in usage of cement leads to a decrease in pollution caused by its production. The cement industry produces about 5% of global man-made CO_2 emissions; the amount of CO_2 emitted by the cement industry can be as high as 900 kg of CO_2 for every 1000 kg of cement produced [1]. It should be noted that the cement industry worldwide and especially in Scandinavia and Europe takes its responsibility and strong efforts are taken to reduce the CO_2 emissions at production. Some companies have formulated a zero-vision [2] and others are engaged in carbon capturing of emitted gas see [3] describing a Heidelberg Cement supported project. Also, concrete producers are now striving to reduce the amount of clinker and thus CO_2 by replacements such as fly ash, blast furnace slag, lime stone filler etc.

The packing density concept can be used as a part of concrete mix design with the aim of minimizing the inter-particle voids between the constituents of concrete in order to reduce the paste demand. Packing density is the ratio of the volume of solids to the bulk volume of the solid particles [4, 5]. The date for one of the first articles on particle packing goes as far as 1892 [6] further researches were conducted mainly concentrating on designing an ideal aggregate size distribution curve [7, 8]. In 1929 the first analytical packing model was designed to predict the void ratio of a mixture of two particle groups [9]. Since then, plenty of researches were conducted on the subject resulting in development of several analytical models and computer-aided mix design software.

Particle packing models can be used as a tool to determine the optimum combination of aggregate mix constitutes that will provide a maximum packing density and minimize the remaining voids. Although it has been recognized nowadays that the binder phase can also be graded just as the aggregate phase for the purpose of achieving tight particle packing or minimum void, research results have shown that improvements achieved in the reduction of void ratio are far greater with the aggregate phase than with the binder phase [10].

The aim of this paper is to examine the reliability and accuracy of analytical particle packing models by comparing the suggested values by the models to actual aggregate packing values obtained in the laboratory. For this purpose, three of more common packing models –Modified Toufar, 4C and CPM- were studied. The results from this type of study can assist the development of future mix design philosophies.

The study only dealt with the precision of packing models considering solely dry aggregates.

2. PARTICLE PACKING MODELS

As mentioned above, it is of extreme importance to minimize voids for optimising concrete mixes. In order to fulfil this requirement it is vital to select an acceptably accurate packing model to estimate the packing density. A number of particle packing models were developed over the past 80 years. However, some of them were proved to be unsuitable for concrete mix

constituent proportioning [11, 12]. Among the remaining models, three of more common ones were chosen and are described briefly in the following sections.

2.1. Modified Toufar

According to Toufar et al. [13] the packing density depends on the diameter ratio of the two particle class that are to be mixed. It is assumed that each of fine particles is placed between exactly four of the course particles. The Toufar model was later modified by Golterman et al. [14] since it was shown that the original model predicts that the packing density of a sample of coarse particles does not increase when a small amount of fine particles is added to the coarse particles, which is in contrast with reality.

The required input data for Modified Toufar model includes packing density φ and characteristic diameter d_{char} of each material that is used in the combination. Modified Toufar model can be used for estimating packing density of a multicomponent system. However, calculation of multi-component mixtures based on this procedure tends to underestimate the packing density [15]. On the other hand Modified Toufar model is fairly easy to use and can be implemented in a spreadsheet with a little effort.

2.2. 4C Model

4C is a computer program developed by Danish Technological Institute and is based on the Linear Packing Density Model (LPDM). The Linear Packing Density Model can be used to optimize the grading curve of a concrete mixture. The key elements of the LPDM used to determine packing density are:

i. Calibrate the eigenpacking density a_i of each constituent material
ii. Calculate a_i of combination for each clustered size class d_i
iii. Calculate y_i (volume) of combination for each clustered size class d_i
iv. Claculate the total packing density

The Linear Packing Density Model can predict the packing density for several particle classes, which makes the model suitable for real concrete mixtures [10]. The accuracy of the model depends on interaction formulas which are relations derived from the packing density of two-component mixtures [16, 17]. 4C packing model uses μ-value as an interaction factor which indicates possible maximum ratio (size) between small and large particles without the smaller particle interfering with the packing of the larger particles. For the purpose of this study three values of μ were compared to actual data obtained from laboratory tests. It should be mentioned that μ is an empirical value and needs to be calibrated based on the laboratory data.

2.3. Compressible Packing Model (CPM)

The CPM is a refined version of a previous model (LPDM) for grain mixtures [18]. The Compressible Packing Model calculates packing density via the virtual compactness β_i instead of a_i (eigenpacking) and a compaction index K. Virtual packing density is defined as the maximum potential packing density of a mixture if the particles would have been placed one by one in such a way that they use the minimum amount of space.

Obviously, the virtual packing density is higher than the real packing density. The difference depends on the applied compaction energy. To drive the real packing density from virtual

density, compaction index K is used; the value of K depends on the compaction energy applied to the mixture. K index was suggested to have the value of 4.1, 4.5, 4.75 and 9 for loose packing, rodding, vibration and vibration+compression respectively. Figure 1 shows the effect of compaction index on packing density of a mixture based on CPM [18].

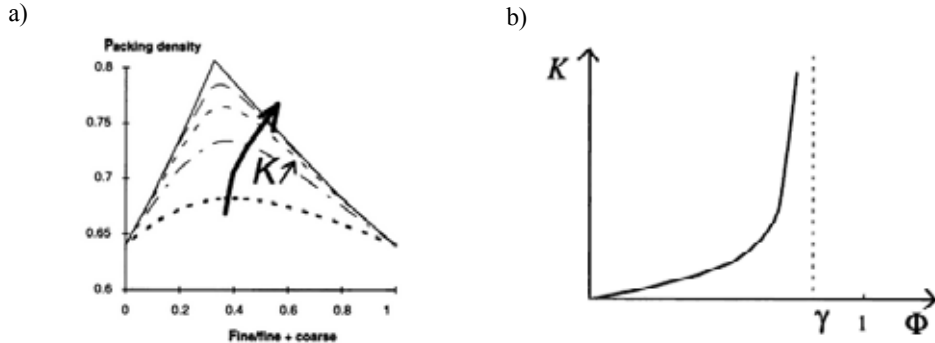a)   b)

Figure1: (a) Effect of K value on compaction where actual packing densities of two classes assumed to be constant. (b) Variation of K vs. packing density [18].

LPDM can be considered as a special case of CPM for which the compaction index K tends to infinity.

Another difference between 4C and CPM is in the way that models handle the interaction of packing densities of components in the mixture. While this is implanted in 4C by means of μ-value, CPM suggest calculating the effect by using mathematical formulas.

In order to use the CPM model, packing density of each fraction, mean diameter and K-value needs to be introduced to the model. CPM can be used to predict the packing density/void ratio for combination of any given number of fractions. However, comparing to the other two models CPM is more complex and requires more input data.

3.   MATERIALS AND METHODS

3.1.   Materials

Seven binary aggregate mixtures were made out of eight fractions of three quarries. The mixes were made in several steps by adding 10% to 20% of volume of fines to coarse material in each step for every binary mixture. Table 1 shows the consumables used in the experiments, Figure 2 illustrates the sieving curves for the materials and Table 2 shows the ingredients for the mixtures.

Table 1 – Aggregates used for the experiments

Quarry	Type	Fraction
Riksten	Natural	0 - 4 mm
		8 - 16mm
Riksten	Crushed	0 - 2 mm
		0 - 4 mm
		4 - 8 mm
		8 - 16 mm
Ledinge	Cubic crushed	0 - 4 mm
		8 - 16 mm
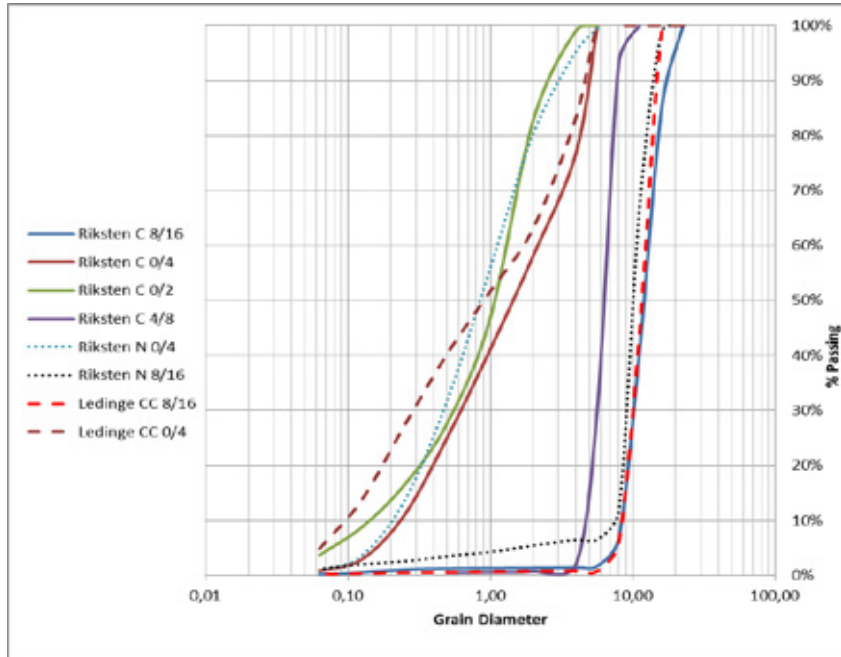
Figure 2 – aggregate sieving curves

Table 2 – Mixtures ingredients

Combo	Fine	Coarse	$d_{50(fine)}$ / $d_{50(coarse)}$*
Mix1	Riksten Crushed 0-4 mm	Riksten Crushed 8-16 mm	0.12
Mix2	Riksten Crushed 0-2 mm	Riksten Crushed 8-16 mm	0.09
Mix3	Riksten Crushed 4-8 mm	Riksten Crushed 8-16 mm	0.52
Mix4	Riksten Natural 0-4 mm	Riksten Natural 8-16 mm	0.08
Mix5	Ledinge Cubic Crushed 0-4 mm**	Ledinge Cubic Crushed 8-16 mm	0.07
Mix6	Ledinge Cubic Crushed 0-4 mm	Riksten Natural 8-16 mm	0.09
Mix7	Riksten Natural 0-4 mm	Ledinge Cubic Crushed 8-16 mm	0.07

* The ratio of mean diameter of fine aggregate class to mean diameter of coarse aggregate class.
**crushed aggregates formed in a crusher to a cubic shape so they become less angular.

3.2. Packing Method

The packing densities for each of listed materials and their mixtures were determined according to European standard EN-1097:3 [19] by means of pouring the aggregate in a standard cylinder

form the distance of maximum 50mm. The dry particle densities and the bulk densities were determined and their packing densities were calculated as the ratio of bulk density of the aggregate to the solid density of the dry aggregate particles. Table 3 shows packing density of aggregates.

Table 3 – Packing density of aggregates in un-compacted condition

Quarry	Fraction	Bulk density (kg/m³)	Particle density (kg/m³)	Packing density[*]
Riksten Natural	0-4 mm	1682	2645	0.636
	8-16 mm	1642	2645	0.621
Riksten Crushed	0-2 mm	1572	2674	0.588
	0-4 mm	1695	2674	0.634
	4-8 mm	1342	2674	0.502
	8-16 mm	1562	2674	0.584
Ledinge Cubic Crushed	0-4 mm	1863	3064	0.608
	8-16 mm	1657	3064	0.541

* Particle packing densities were corrected for cylinder wall effect.

4.   RESULTS

Figure 3 illustrates the results of packing densities obtained from the laboratory experiment versus Modified Toufar model, 4C and CPM. For the purpose of sensitivity analysis three different μ-values were introduced in 4C software as 0.07, 0.05 and 0.03. The models' estimation had a point to point deviation of 0.5 % to 5.8 % in packing density comparing to the laboratory data. The least error occurred in mixtures with higher mean diameter ratio between fine and coarse aggregate fractions. The maximum error took place in prediction of packing densities for mixtures combined of natural aggregate as coarse and cubic crushed material as fine.

Figure 4 shows the total comparison of differences between measured and calculated packing densities. Considering all the data obtained in the laboratory, Modified Toufar showed 1.7 % mean difference while the mean difference for CPM and 4C were 1.8 % and 1.9 % respectively. However, comparing each mixture leads to different values as some of the models are more suitable with specific mixtures; see Table 4 in Section 5.

For the purpose of unified comparison only results with assumption of μ-value = 0.07 was considered for 4C model as this number is suggested in 4C manual and furthermore, it is not possible to choose the best value of μ prior to conducting actual laboratory tests.
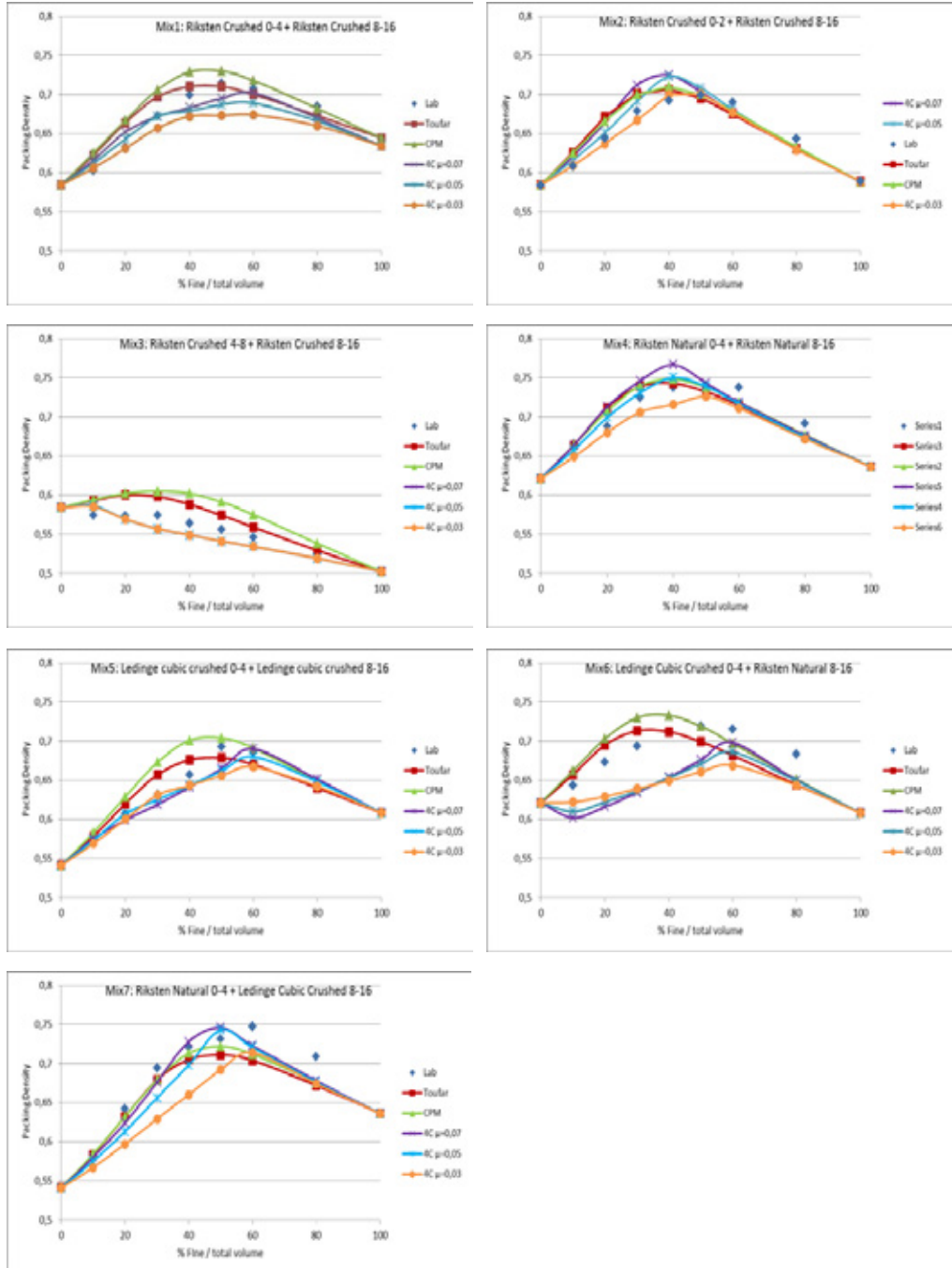
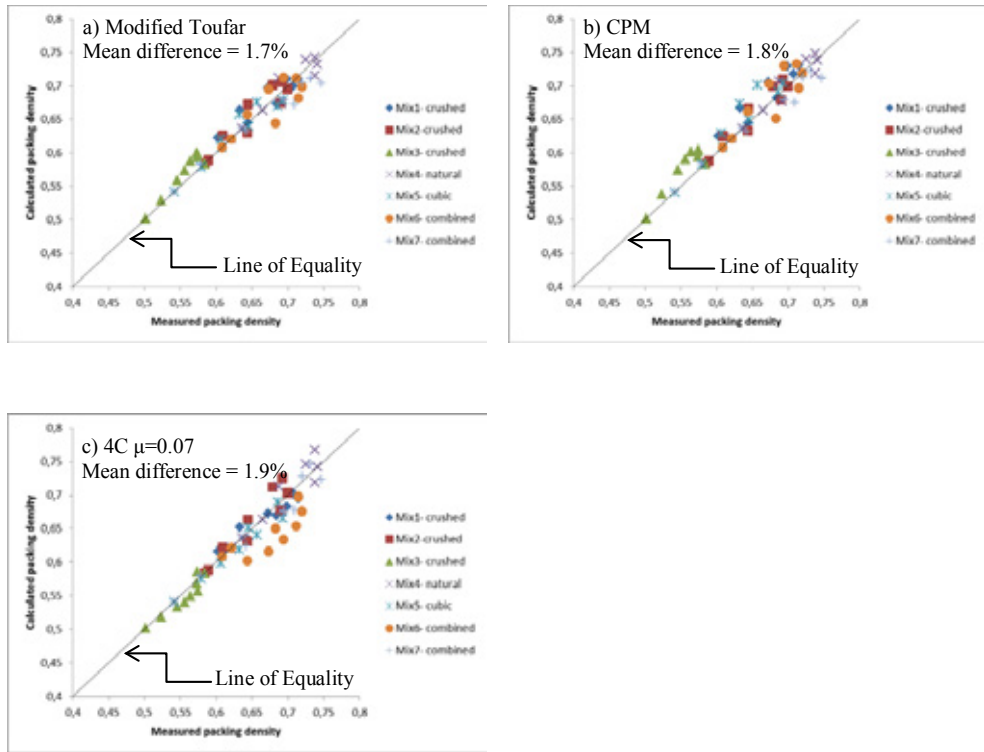*Figure 3 – Packing densities of binary mixes, models vs. lab data.*

Figure 4 – Comparison of difference between calculated and measured values

5. DISCUSSION AND CONCLUSION

There were some subtle differences between the models: Modified Toufar and CPM suggested more or less the same values of fine percentage corresponding to the packing density. However, CPM slightly overestimated packing values comparing to Modified Toufar model. This is in agreement with what was concluded earlier by Jones et al. [10]. Both CPM and Modified Toufar overestimated the packing density where volume of fines engaged in the mixture was less than 40% of the total volume. 4C tends to behave more inconsistently with variation of mixtures.

According to Figure 4, Modified Toufar's predictions show the least deviation from the measured packing densities (1.7%). However, it had been showed that the model's accuracy decreases as the number of ingredients in a mixture increases [15].

CPM was able to predict the packing density with a mean difference of 1.8%. CPM is more suitable for using with multicomponent mixtures as it was formulated in a way that theoretically it can predict packing density of any given number of fractions in one equation, the same cannot be said about Toufar as for Modified Toufar model, packing density of classes of aggregates need to be calculated in a binary system and then the result should be added to a third class and

so on. 4C is capable of calculating the packing density for a mixture with up to three constitutes. However, for a binary mixture, Toufar is preferable comparing to CPM and 4C as it has higher accuracy and is simpler to use.

It should be mentioned that, all of the models trends merge and became more in agreement with each other and the laboratory data on the finer side of the packing diagrams.

In order to compare the data in more detail, Table 4 is presented which shows the mean difference between the calculated data by each of three models and measured values for each mixture. It should be mentioned that for the calculation of mean difference, only the data corresponding to 40 % to 60 % of fine/ total volume of aggregate was taken into account. The reason for choosing the mentioned range is firstly, the maximum packing density usually occurs in this domain and secondly, it is more practical to have concrete recipes with 40 % to 60 % of fine / total volume of aggregate since using more than 60 % of fines will lead to a very viscous concrete with large demand for superplasticizer and less than 40% of fines results in "too stony" concrete.

Table 4 – Comparison of models suitability on each mixture

Combo	$d_{50(fine)}/$ $d_{50(coarse)}$	Mean difference			Suitability			
		M.Toufar	CPM	4C	High	Medium	Low	N/A
Mix1	0.12	0.78%	1.86%	1.37%	4C, Toufar	CPM	--	--
Mix2	0.09	1.12%	0.98%	1.64%	CPM, Toufar	4C	--	--
Mix3	0.52	1.83%	3.40%	1.40%	4C	Toufar	--	CPM
Mix4	0.08	1.24%	1.07%	1.67%	CPM, Toufar	4C	--	--
Mix5	0.07	1.62%	1.99%	1.62%	4C, Toufar	4C, Toufar, CPM	--	--
Mix6	0.09	1.80%	1.34%	3.94%	CPM	Toufar	--	4C
Mix7	0.07	2.65%	1.75%	1.52%	4C	CPM	Toufar	--

Note that in Table 4, suitability of the models was decided based on the mean difference from the laboratory data where high suitability was assigned to predictions with less than 1.5 % mean difference, medium was used for predictions with mean difference between 1.5 % to 2 % and low suitability for predictions with error higher than 2 % and finally, predictions with error higher than 3 % were considered as unsuitable. The criterion can be justified by the fact that trials in the lab consisted of up to 2% variation in the packing density due to changes of size distribution and randomness of aggregate shapes in the quarries.

Results from Table 4 imply that as the mean size ratio of fines over coarse material decreases the accuracy of CPM and Modified Toufar increase. Contrariwise, 4C is more suitable with higher mean size ratios. Note that Mix6 was consisting of cubic crushed materials as fine and natural aggregate as coarse; this led to incapability of 4C model to predict the packing density with good accuracy. Nevertheless, further work is necessary to examine the effect of changes in packing density of a mixture on workability of concrete so that a basis for acceptable error range of packing density/void ratio prediction of the models can be established.

AKNOWLEDGEMENT

REFERENCES

1. Mahasenan, N., Smith, S., Humphreys, K., & Kaya, Y. "The cement industry and global climate change: current and potential future cement industry CO2 emissions." *Greenhouse Gas Control Technologies-6th International Conference*, August 2003, Oxford: Pergamon ,pp. 995-1000

2. "Meeting the challenge through a zero vision" retrieved 10th Oct 2014 from: *http://www.hcne-sustainability.nu/en/node/2183*

3. "Carbon capture newsletter", 2014-2, retrieved 10th Oct 2014 from: *http://www.heidelbergcement.com/no/no/norcem/sustainability/Karbonfangst/Nyhetsbre v.htm*

4. Wong, H. H., & Kwan, A. K. "Packing density: a key concept for mix design of high performance concrete". *Proceedings of the materials science and technology in engineering conference*, HKIE materials division, Hong Kong, May 2005, pp. 1-15

5. Quiroga, P. N., & Fowler, D. W. "Guidelines for proportioning optimized concrete mixtures with high microfines". *International Center for Aggregates Research Report: 104-2*, 2004.

6. Feret, R. "Sur la compacité des mortiers hydrauliques". *Annales des Ponts et Chaussées. Vol. 4 (2e semestre)*, 1892,(pp. 5-16).(In French)

7. Fuller, W. B., & Thompson, S. E. "The laws of proportioning concrete". *Transactions of the American Society of Civil Engineers, 57(2),* 1907.

8. Andreasen, A. M., & Andersen, J. "Relation between grain size and interstitial space in products of unconsolidated granules." *Kolloid Z journal*, 50, 1930, pp. 217-218

9. Furnas, C. C. "Flow of gases through beds of broken solids" *(Vol. 300). US Govt. print. off.* 1929.

10. Jones, M. R., Zheng, L., & Newlands, M. D. "Comparison of particle packing models for proportioning concrete constituents for minimum voids ratio" *Journal of Material and Science,* Vol 35, June 2002, pp. 301-309

11. Dewar, J. "Computer modelling of concrete mixtures." *CRC Press*, 2002.

12. Johansen, V., & Andersen, P. J. " Particle packing and concrete properties", *Journal of Materials and Science of Concrete 2*. 1996, pp. 111-147

13. Toufar, W., Born, M., & Klose, E. "Contribution of optimisation of components of different density in polydispersed particles systems". *Freiberger Booklet A*, 1976, pp. 29-44

14. Goltermann, P., & Johansen, V. (1997). "Packing of aggregates: an alternative tool to determine the optimal aggregate mix" *ACI Materials Journal, 94(5).* 1997, pp. 435-443

15. Fennis, S. A. A. M."Design of ecological concrete by particle packing optimization" *Dissertation, Delft University of Technology.* 2011.

16. Stovall, T., Larrard, F. de and Buil, M. " Lineair Packing Density Model of Grain Mixtures" *Powder Technology, Vol. 48*, 1986, pp. 1-12

17. Larrard, F. de. "Concrete mixture proportioning: a scientific approach". *London: E & FN Spon*. 1999.

18. Glavind, M., Olsen, G. S., & Munch-Petersen, C. "Packing calculations and concrete mix design". *Nordic Concrete Research*, 13(2).1993.

19. Swedish Standards Institute, "Tests for mechanical and physical properties of aggregate – Part 3: Determination of loose bulk density and voids". *SS-EN-1097:3*. October 1998.

Plastic Shrinkage Cracking in Concrete: State of the Art

Faez Sayahi
Ph.D. Student
Div. of Structural Engineering
Luleå University of Technology, LTU
971 87 Luleå, Sweden.
faez.sayahi@ltu.se

Mats Emborg
Professor LTU/Head R&D Betongindustri AB
971 87 Luleå, Sweden. /Betongindustri AB, 100 74 Stockholm.
mats.emborg@betongindustri .se
mats.emborg@ltu.se

Hans Hedlund
Professor LTU/Skanska Teknik AB
971 87 Luleå, Sweden/Skanska AB, 405 18 Göteborg, Sweden
hans.hedlund@ltu.se
hans.hedlund@skanska.se

ABSTRACT

As plastic shrinkage cracking can dramatically reduce the durability of a concrete member and causes considerable repair costs annually, a comprehensive understanding of the mechanism of the phenomenon is essential to prevent these damages in future. In this paper, an overview is given on the mechanism of plastic shrinkage crack formation and the status of present technologies avoiding the cracking are reported through referring to previously conducted research and observations.

Keywords: Plastic Shrinkage, Cracking, Concrete, Evaporation, Capillary pressure.

1.   INTRODUCTION

Crack-free concrete structures are needed in order to ensure high level of durability and functionality, since cracks accelerate the ingress of harmful materials that might cause damage in future, e.g. corrosion of the reinforcement [1]. Plastic shrinkage cracking of concrete is often the first type of cracks occurring shortly (within the first few hours) after placing the concrete, even before initial setting [1-4]. As known also settlement cracks can occur very early. According to ACI 305R [5]: "Plastic shrinkage cracking is frequently associated with hot weather concreting in arid climates. It occurs in exposed concrete, primarily in flat work but also in beams and footings and may develop in other climates whenever the evaporation rate is greater than the rate at which the water rises to the surface of recently placed concrete by bleeding". It is thus understood that this type of cracking, mainly occurring on horizontal concrete elements with large surface to volume ratio (such as slabs, pavements, beams, etc.), can dramatically affect the aesthetics, durability and serviceability of the structure [6, 7].

The main reason behind plastic shrinkage cracking is considered to be rapid and excessive surface water evaporation of the concrete element in the plastic stage (freshly cast concrete) which in turn leads to the so-called plastic or capillary shrinkage [2-5, 8-17]. Consequently, many factors affect the likelihood of plastic shrinkage crack formation such as water-cement ratio, admixture, member size, fines content, concrete surface temperature and ambient conditions (i.e. relative humidity, air temperature and wind velocity). All these factors influence the water evaporation rate of the concrete which is considered, among others, as an indication of the possible beginning of the plastic shrinkage cracking [18]. As long as the evaporation rate is less than the bleeding rate, a thin water film covers the surface of the concrete. Soon after the disappearance of this thin water layer, capillary pressure inside the concrete increases, which results in the so called plastic shrinkage. It should be mentioned here that the bleeding can be very small or not existing at all for concretes of low water/cement ratio, e. g. those designed for fast drying through self-desiccation..

If the concrete member is restrained in any way (e.g. due to reinforcement, change of sectional depth, difference in shrinkage in different parts of the concrete, friction of the mould, etc.) , the developed shrinkage can cause tensile strain accumulation, starting from the concrete surface. When the tensile strain exceeds the tensile strain capacity of the concrete, which at early ages is very low, cracks start to form [19]. In many cases, plastic shrinkage cracks are so thin (sometimes invisible to an unaided eye) which can be overlooked or covered by the surface finishing [2]. However, later on phenomena such as external loading, thermal strain, or drying shrinkage can widen the crack which as mentioned earlier negatively influences the serviceability of the concrete structure.

Plastic shrinkage cracking, in general, is a complex combination of interdependent variables which can facilitate or prevent the phenomenon under different circumstances. Thus, studying plastic shrinkage cracking requires a high level of persistence and intense theoretical and experimental investigation.

In this paper, the phenomenon of plastic shrinkage cracking in concrete is investigated and an attempt is made to reach a comprehensive perspective of the formation process and mechanism. In addition several variables such as water/cement ratio, thickness of the concrete section, fines content, additives, and fibres are briefly described. This research is based on the achievements reported by several researchers around the world and aims to present a state of the art in order to

make plastic shrinkage cracking in concrete clearer and more understandable. The work intends to constitute a base of future research at Luleå University of Technology.

2.   MECHANISM OF PLASTIC SHRINKAGE CRACKING

In order to gain a general comprehension of the plastic shrinkage cracking phenomenon, initially, it is important to have a picture, as clear as possible, regarding the mechanism of plastic shrinkage crack formation. In Fig.1 (quoted from [6]), the process of plastic shrinkage crack formation is schematically explained. Based on the interaction between the plotted lines (factors), various milestones (i.e. drying time, air entry time, crack onset time, etc.) can be defined.

After placing the concrete in its mould, if not a high performance concrete or similar is used, a thin film of water covers the surface and an interconnected pore system, completely filled with water is formed [2]. Shortly later the drying time (TD) is reached when the water evaporation rate exceeds the bleeding rate of the concrete (see Fig.1). In this case the thin water film is disappeared due to evaporation and the water in the pore system starts to evaporate [20]. This moment is the onset of capillary pressure rise which converts it from a compressive pressure to a tensile pressure. The reason that capillary pressure is compressive before drying time is the existence of the internal water pressure in the concrete [20]. The capillary pressure keeps increasing until air breaks through the pore system, starting from the largest pores. This time is defined as the air entry time [17]. Consequently, the capillary pressure drops down suddenly and dramatically since the paste can no longer resist the tensile capillary pressure. Value of the capillary pressure at the air entry time is critical since the empty pores form weak points at the concrete surface which can be the origin of strain localization and cracking [2].

Based on the above, plastic shrinkage cracking is mainly related to the evaporation rate and bleeding rate of the concrete. These factors in addition to capillary pressure and tensile strain play the key role in the mechanism of plastic shrinkage cracking [2, 6, 18, 21]. These parameters are discussed briefly in the following sections.
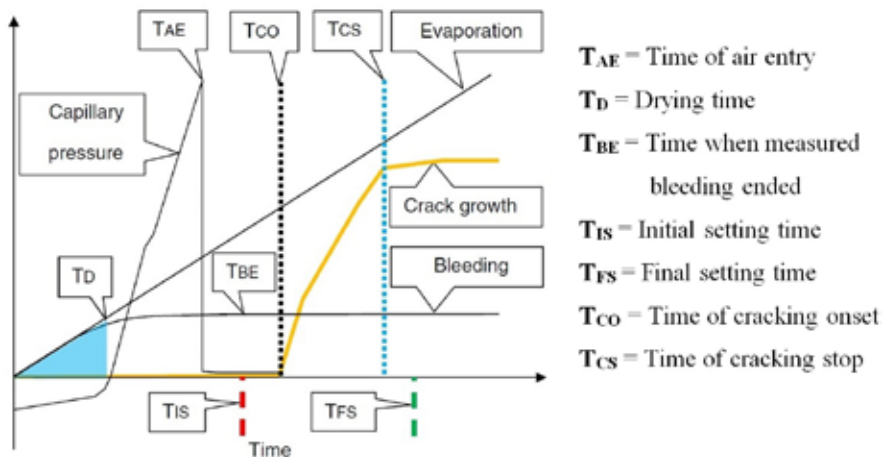

Figure 1 - Typical behaviour of plastic shrinkage crack [6]

3.   EVAPORATION

The evaporation is considered as an indicator for the probability of plastic shrinkage cracking onset in freshly placed concrete. For instance, according to ACI, precautions must be taken when the water evaporation rate is equal to or more than 1.0 kg/m^2/hr [5]. Nevertheless, some experimental results show that this value may be too high for some modern concrete compositions, i.e. plastic shrinkage cracking may occur at evaporation rate of 0.2 kg/m^2/hr under hot weather conditions [12].

Water evaporation in concrete occurs due to a) heat energy absorption into the water, e.g. air temperature, concrete temperature, solar radiation; b) low humidity, i.e. the ambient pressure is less than that in the water [18]. Accumulation of escaping water molecules above the water surface increases the humidity and consequently decreases the evaporation, especially when the concrete perimeter is closed. Thus, wind can accelerate the process as it removes the escaping water molecules.

As can be comprehended from the above, the environmental factors that can highly influence the water evaporation rate are air temperature, concrete (water surface) temperature, wind and humidity. These factors are used in the ACI nomograph for estimating rate of surface water evaporation in concrete (see Fig.2). The outcome of this nomograph is a value for the evaporation rate of the concrete, in which provides an indication of the possible onset of plastic shrinkage cracking [18]. This nomograph was first developed by Bloem in 1960 [22] who in turn used the numerical values presented in a table by Lerch in 1957 [3]. The values in the table were derived using a formula presented by Menzel in 1954, expressed as Eq.1 (only available in imperial unit system)[23]:

$$W = 0.44(e_0 - e_a)(0.253 + 0.096\ V) \tag{1}$$

where:
W = weight (lb) of water evaporated per square foot of surface per hour (lb/ft^2/hr),
e_0 = pressure of saturated vapour at the temperature of the evaporating surface, (psi)
e_a = vapour pressure of the ambient air, (psi)
V = Average horizontal air and wind speed measured at about 20 inches (500 mm) above the concrete surface, (mph).

In 1998, based on Menzel's formula, Uno [18] proposed a single operation equation to predict the water evaporation rate. The new formula does not use vapour pressure as input since a temperature-vapour pressure relationship has already been incorporated in the formula. The correlation coefficient of this relationship is 0.99 for the temperature range 15 to 35°C [18]. The formula is expressed as:

$$E = 5([T_c + 18]^{2.5} - r \,.\, [T_a + 18]^{2.5})(V + 4) \times 10^{-6} \tag{2}$$

where
E = water evaporation rate, (kg/m^2/h)
T_c = Concrete (water surface) temperature, (°C)
T_a = air temperature, (°C)
R = relative humidity, (%)
V = wind velocity, (km/hr).

This formula is widely used since the establishment. Comparison between Menzel and Uno's formula shows almost complete accordance in the results. In addition both formulas give almost similar evaporation rates to those extracted from the ACI nomograph. However, even if the water evaporation rate is accurately determined based on the above mentioned methods, still there is no guarantee that it can be applicable and reliable indicator of the cracking onset. That is due to the fact that, as mentioned earlier, the evaporation rate has to exceed the concrete bleed rate in order to cause plastic shrinkage [25].
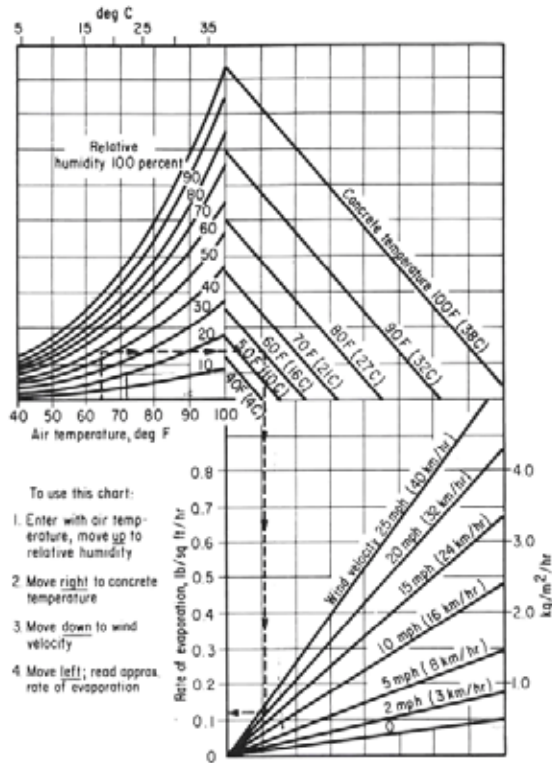

Figure 2 – ACI nomograph for estimating surface water evaporation rate of concrete i e. the "ACI Hot Weather Concreting Evaporation Nomograph" [5].

4.   BLEEDING

Bleeding is defined as the ascending of the mixing water to the concrete surface. Typically, it occurs as the result of settlement and consolidation of freshly placed concrete under the gravitational force [26]. It occurs due to the inability of the solid particles to retain the water during the settlement. There are two independent driving forces which cause bleeding in concrete: the gravity which settles the solid particles of the concrete mixture, and the capillary pressure (suction) which occurs after the thin water layer on the surface has disappeared [16]. Bleeding rate can be measured experimentally using some standard methods such as the Australian standard [27] or according to ASTM C232/C232M [28].

In general, bleeding depends on the water/cement ratio, particle size distribution, viscosity of the concrete and the rate of hydration [6]. In addition, the depth of the concrete member can influence the bleeding rate [2]. Bleeding typically stops when the hydration products are abundant enough to prevent any further concrete settlement, which is the description of the state at the initial setting time of the concrete [29].

The assumed range of bleeding rate for concrete has decreased during the past century. Until 1960, it ranged from 0.5 to 1.5 kg/m^2/h [16, 18]. However, in modern concretes, bleeding rate is considerably decreased to less than 1 kg/m^2/h [16]. The reason lies in the general desire of gaining less bleed rate in order to achieve higher mechanical properties and less permeability in the modern concretes through lowering w/c ratio and increasing fine cement, fly ash and silica fume content in the mixture. The final product then, is a concrete with extremely low or even zero bleeding rate [30].

Although a certain level of bleeding might be desirable in order to replace evaporated water and keep the surface wet, it should be noted that excessive bleeding in turn, may cause various damages as well. These damages include plastic settlement cracking, surface laitance formation, longer finishing time, strength decrease and lower bonding between the solid particles [12, 16].

5.   CAPILLARY PRESSURE

Capillary pressure (also referred to as matric suction, capillary tension or capillary suction) is as discussed earlier the origin of plastic shrinkage cracking. It is highly influenced by the water evaporation rate of the concrete. Therefore, capillary pressure can be considered as another indicator for the risk of shrinkage cracking onset.

5.1   Capillary pressure build-up mechanism

Plastic or capillary shrinkage is a result of a physical process which builds up negative pore pressure in the liquid phase of the cementitious material [2, 11]. As mentioned before, after casting the concrete, a thin plane film of water covers the surface of the concrete member and an interconnected pore system, completely filled with water is formed (Fig.3, Level A). As long as the evaporation rate is less than the bleeding rate, the surface remains covered by this thin water layer. However, the thickness of this layer decreases gradually, as a result of evaporation. Once the water layer disappears, the adhesive force and surface tension of water form menisci between the solid particles of the paste (Fig.3, Level B and Fig.4). These menisci cause negative pressure (tensile capillary pressure) in the concrete pore system. The description of this phenomenon lies in the Young-Laplace equation when the pores are assumed perpendicular to the concrete surface:

$$P = -\frac{2\gamma}{R} \cdot \cos\theta \qquad\qquad (3)$$

where
P= pressure in the pore liquid, (Pa)
R = radius of the meniscus, (m), see Fig.4
γ = surface tension of the pore liquid (0.073 N/m for water)
θ = wetting angle, (deg.).

Cementitious materials are considered as siliceous materials i.e. full wetting material. In such material the wetting angle is 0.

The negative capillary pressure, applies inward force on the solid particles at the concrete surface. As the evaporation continues, the radius of the menisci in the pore system gradually decreases (Fig.3, Level C). Consequently, the capillary pressure keeps rising, causing contraction of the material. So far the contraction induced volume change approximately equals the volume of the evaporated water [17].
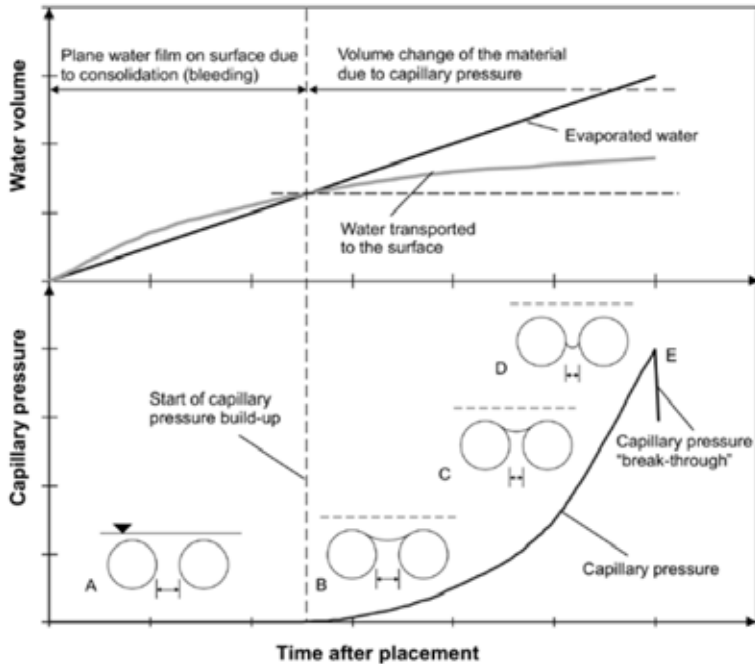

Figure 3 – Mechanism of capillary pressure build-up. The upper part of the figure shows evaporation and bleeding vs. time after placement (see also Fig. 1) [2].
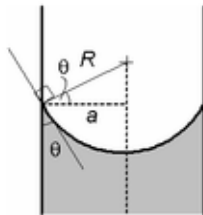

Figure 4 – Water meniscus in a pore.

As the capillary pressure increases, the radius of the meniscus decreases until it becomes equal to the minimum radius of the associated pore (Fig.3, Level D). The rise of the capillary pressure continues until at a certain value, the menisci break and let air penetrates the pore system (Fig.3, Level E). Once this happens, the capillary pressure dramatically drops down to almost zero i.e. it breaks down. The moment when capillary pressure breaks down and air penetrates into the pore system is called air-entry time.

It should be noted that due to the irregularity of particle arrangement in the concrete paste, air entry does not occur simultaneously in all pores [17]. In other words, air entry is rather a local event than a universal one. Therefore, different values for maximum capillary pressure may be measured in different parts of the concrete member. For example, Slowik [29] in 2008 performed an experiment on cement paste samples, using two pressure sensors in different locations. Each sensor measured different maximum capillary pressure (Fig.5). Thus, the maximum capillary pressure at a certain location does not represent the absolute maximum capillary pressure in the concrete. In addition, the capillary pressure may break down if the sensor tip penetrates an air bubble inside the concrete [17].
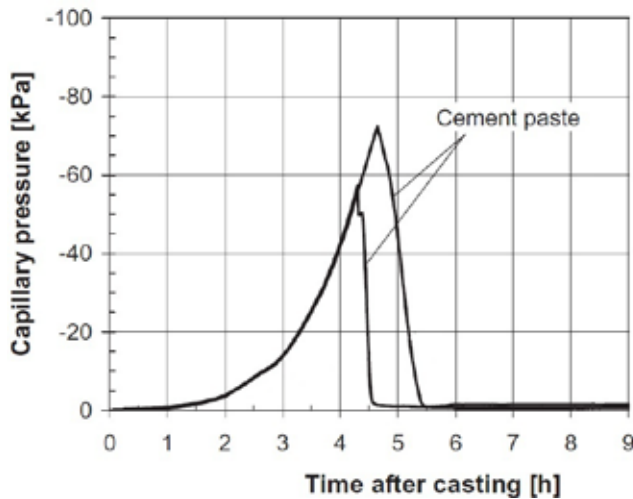

Figure 5 – Difference in maximum absolute capillary pressure in different locations [29].

Based on Carman [31], an equation was proposed by Powers [25] for determining maximum capillary tensile pressure in concrete, which was modified by Cohen [10]:

$$P = 1 \times 10^{-3} \frac{\gamma \cdot S}{w/c} \qquad (4)$$

where
P = capillary tensile pressure, (Pa)
γ = surface tension of the pore liquid (0.073 N/m for water)
S = mass specific surface area of cement, (m^2/kg)
w/c = water/cement ratio by mass, (-)
The constant 10^{-3} has the dimension mass density (kg/m^3).

According to Eq.4, capillary pressure (P) is directly proportional to γ and S, and inversely proportional to w/c ratio. It means that keeping other variables constant, concrete with higher w/c ratio and lower γ and S is less suspected to experience plastic shrinkage cracking [16].

Furthermore, based on Eq.4, assuming constant γ and w/c ratio, capillary pressure (P) is directly proportional to mass specific surface area of cement (S). In other word, maintaining all conditions similar, any difference in plastic shrinkage characteristics (i.e. strain and cracking) would be due to the difference in surface area or particle size of the solid material [10]. This was also observed in Eq.5 proposed by Pihlajavaara [32] to determine the capillary pressure in concrete with spherical non-porous solid aggregates:

$$P = 2.6 \times 10^{-7} \cdot \gamma \cdot S \cdot \rho \tag{5}$$

where
P= capillary tensile pressure, (Pa)
γ = surface tension of the pore liquid (0.073 N/m for water)
S = mass specific surface area of cement, (m^2/kg)
ρ = solid density of cement, (kg/m^3)
The constant 2.6×10^{-7} is dimensionless.

The maximum absolute capillary pressure, P, is considered critical since - after breaking down - creates weak points at the surface of the concrete. If the concrete is restrained, these weak spots, eventually, may be origins of strain localization and crack initiation along a line which connects them.

Based on the above mentioned facts, the capillary pressure in the concrete must kept less than the air entry value to prevent any strain localization and cracking onset. This typically takes place through preventing the surface water evaporation

5.2   Capillary pressure measurement

Capillary pressure in concrete is typically measured using pressure sensors such as those showed in Fig. 6. The tip of the sensor is filled with water which allows in-situ negative fluid pressure measurement. The tip of the sensor should penetrate the concrete by about 50 mm. In this case, the weight of the sensor is supported by the sensor tip. A recording device, then, collects all the data from the pressure sensors, which makes it possible to plot them versus time in a diagram. Both wired and wireless sensors are now available on the market.

6.   TENSILE STRAIN

As previously mentioned, increasing capillary pressure leads to plastic shrinkage in the concrete. If the concrete is restrained (e.g. due to reinforcement, change of sectional depth, difference in shrinkage in different parts of the concrete, friction of the mould, etc.), this plastic shrinkage causes mechanical tensile strain (i.e. if the plastic shrinkage can develop freely, it will not induce any cracking). On the other hand, experiments have shown that strain capacity reaches its lowest value around the initial setting time of the concrete (see Fig.7) [6]. Once the strain capacity is less than the mechanical tensile strain, the concrete starts to crack.
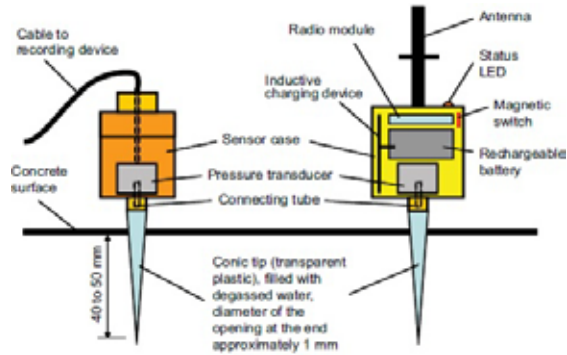
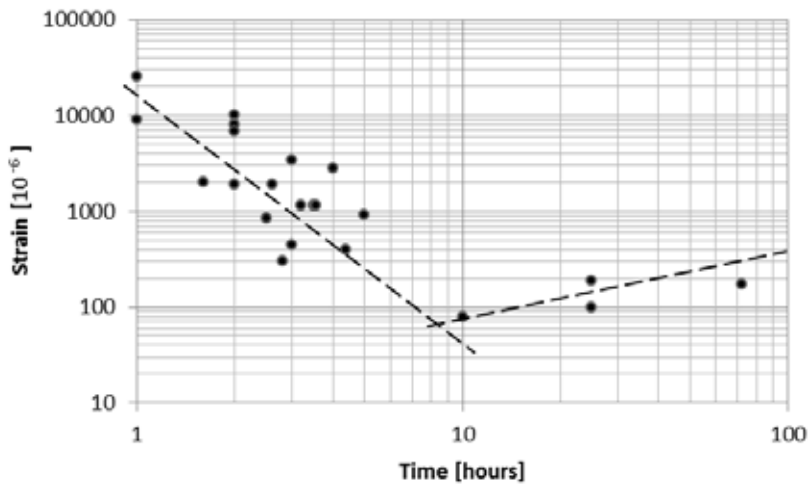Figure 6 – Wired and wireless pressure sensors [2]

Figure 7 – Tensile strain capacity of fresh concrete [6].

As it was mentioned in section 2, plastic shrinkage cracks, typically, are visible after the initial setting time of the concrete (see Fig.1), which confirms the above mentioned fact. Hence, plastic shrinkage induced tensile strain can be another indicator of the cracking risk.

Several researchers have taken this fact into account and developed models to estimate the plastic shrinkage cracking risk based on the tensile strain in the concrete. Boshoff [6] in 2013, proposed a so-called "PShC severity model" to predict the plastic shrinkage cracking degree:

$$PShC = ER \times t_{set} - W_{bl} \tag{6}$$

where
ER = evaporation rate, (kg/m^2/h)
t_{set} = the time between casting and the initial setting time, (hr)
W_{bl} = the total bleed water, (kg/m^2).

According to this model, the severity of plastic shrinkage cracking is dependent on the plastic shrinkage strain which is directly related to the rate of water evaporation, hardening time of the concrete (initial setting time) and bleeding characteristics [6]. In other word, it relates the severity of plastic shrinkage cracking to the amount of the evaporated water (total amount of evaporated water, minus the bleed water) from within the concrete, between the casting and initial setting time [6].

7.   MAIN FACTORS AFFECTING PLASTIC SHRINKAGE CRACKING

So far, the main parameters in the mechanism of plastic shrinkage formation, (i.e. evaporation rate, bleeding rate, capillary pressure and tensile strain) and the relation between them have been briefly described. Fig. 8 is an attempt so summarize the parameters mentioned and the way they are linked together. Nevertheless, there are many factors which can affect plastic shrinkage cracking. A deep comprehension of the way these factors influence the whole cracking process can lead to invention of new crack prevention methods. Some of these factors are briefly described in the following , including water/cement ratio, depth of the concrete section, additives, fines content, fibres and curing measures.

7.1   Water/cement Ratio

Water/cement ratio plays a key role in plastic shrinkage cracks formation. Higher w/c ratio means more bleeding water and vice versa. Thus, in case of high w/c ratio, it takes longer time for the surface water layer to disappear due to evaporation and consequently delays the capillary pressure build-up in the pore system.

It is known that a lower w/c ratio causes less bleeding water and thus increases the risk of cracking [33]. On the other hand w/c ratio has an inverse relation with the concrete strength as higher ratio causes lower concrete strength and vice versa. Research has shown that high-strength concrete mixtures (containing more cement) have low bleeding rate and subsequently higher risk of plastic shrinkage cracking [34]. Thus, optimizing the w/c ratio can be a method to avoid plastic shrinkage crack formation. If high-strength concrete is not necessary, it may be a good idea to use higher w/c ratio. However, it should be noted that very high w/c ratio can dramatically reduce the durability and serviceability of the concrete member.

7.2   Depth of the concrete section

A deeper concrete member typically experiences more settlement, since it contains more settling solid particles. Correspondingly, for higher w/c ratios, the bleeding capacity of the member is higher resulting in more bleed water accumulation on the surface. This means that the surface water layer evaporation takes longer time in comparison, causing delay in capillary pressure build-up. Consequently, it can be concluded that a deeper concrete section is less prone to plastic shrinkage cracking [8, 35]. However, due to the high degree of settlement, the concrete may be vulnerable to settlement cracking typically formed above the reinforcement bars, which may facilitate the ingress of chlorides and other harmful materials.
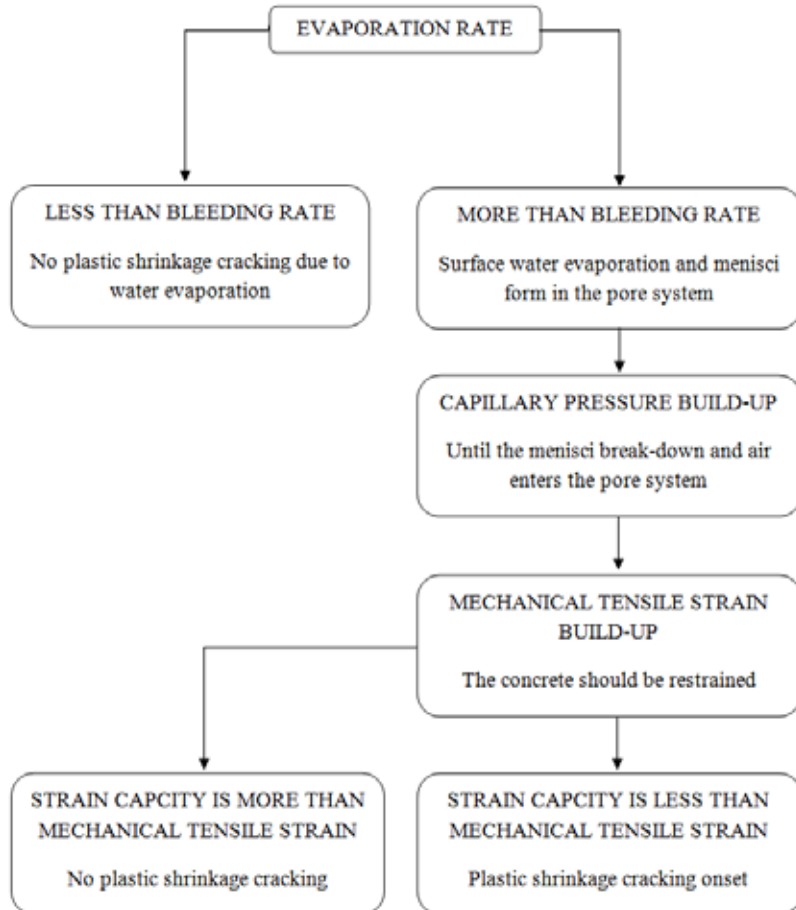
Figure 8 – Plastic shrinkage cracking flowchart.

7.3   Additives

Several research studies have been carried out to find new admixtures in order to reduce the plastic shrinkage of concrete. These admixtures show high practicality in reducing evaporation rate, settlement, negative capillary pressure and plastic shrinkage formation. For instance, it has been concluded that cellulose-based viscosity modifying agent (stabilizer) causes reduction of the evaporation rate [36].

Moreover, accelerators and retarders have a strong influence on plastic shrinkage cracking. Some experiments [20, 37] showed that accelerator admixtures cause higher plastic shrinkage and total crack area, while retarders act contrary. However, other experiments [15, 38] showed that excessive usage of retarder admixtures may increase the risk of plastic shrinkage cracking due to the slower strength gain of the concrete.

On the other hand, superplasticizers reduce the need for water in the concrete mixtures (less bleed water at the surface). This reduction of surface water may however not increase the risk of cracking, as the superplasticizer modifies the surface tension and prevent or delays the onset of plastic shrinkage crack formation [39].

7.4   Fibres

Fibres (steel and/or polypropylene) have often been recently used in concrete mixtures aiming at lowering the risk of plastic shrinkage cracking, through stitching the concrete surface particles together. For instance experimental results presented by Sivakumar and Santhanam [7] show that a combination of steel and polypropylene fibres (hybrid fibres), can reduce the width of the plastic shrinkage crack up to 55% in comparison to concrete mixture without fibres usage.

However, the only problem is that although the crack width was lower, parallel cracks were formed in the main crack's surroundings. This phenomenon can be due to the transfer of the shrinkage stresses, through the fibres, to the surrounding areas. The number of these parallel cracks could be reduced in case of steel fibre usage. The reason lies in more fibre availability in case of hybrid usage compared to the steel fibre system (due to the lower density of polypropylene fibre in comparison to steel fibres), which facilitates the shrinkage stress transfer. Nevertheless, hybrid fibres show a great enhancement in relation to reducing plastic shrinkage cracks [7].

7.5   Fines content

Fines (such as fly ash, silica fume, slag, etc.) induce greater surface area to adsorb water. Consequently, the water that is supposed to be transported to the concrete surface will be adsorbed on the fine particles, resulting in lower bleeding rate.

Cohen et al. [10] concluded that higher surface area of the particles leads to higher tensile capillary pressure and eventually higher probability of plastic shrinkage crack formation. Moreover, experiments performed by Esping et al. [15] showed that silica fume increases the crack tendency in the concrete. Thus, using high proportion of fine material in the concrete mixture is not favourable in relation to plastic shrinkage cracking.

7.6   Curing measures

Plastic shrinkage cracks can be avoided through several curing measures applied on the concrete after casting. Since the main reason behind this phenomenon is water evaporation, curing measures in general aim to eliminate or reduce the evaporation of the surface water. For example covering the concrete with plastic sheet, decreases the evaporation rate and consequently leads to a crack-free concrete [40]. In another case, experiments have shown that evaporation of the surface water can be suppressed through spraying aliphatic alcohols over the fresh concrete surface [41].

Moreover, in some cases curing the concrete takes place through replacing the evaporated surface water (rewetting). For example, fogging the freshly cast concrete surface, on one hand, reduces the evaporation rate through increasing the ambient relative humidity, and on the other hand, replaces some lost surface water due to evaporation [17].

In addition to the above, using a wind breaker to prevent or reduce the air flow over the concrete surface can be another way to reduce the evaporation of the surface water [18].

8.   CONCLUSION

Plastic shrinkage cracking is a complex interaction of several variables that may change in different circumstances. These variables have direct influence on the evaporation and bleed rate of the concrete which subsequently affect the capillary pressure and tensile strain at the early age. The explanations offered in this paper for the plastic shrinkage cracking mechanism and the role of each variable in the process may facilitate gaining a comprehensive understanding of the phenomenon. Moreover, knowing the influence of each variable can lead to innovation of new crack preventive measures.

Despite of the general consensus on the major role of water evaporation in the plastic shrinkage crack formation, not all the cracking incidents are explainable based on that. This illustrates the incompletely understood aspects of the whole process. The inter-connection and complexity of the different variables need to be explored. Thus, in the future, emphasis should be on documenting the various factors through laboratory tests under controlled conditions.

ACKNOWLEDGMENT

REFERENCES

1. Leemann A, Nygaard P, Lura P. "Impact of admixtures on the plastic shrinkage cracking of self-compacting concrete". *Cement and Concrete Composites*. Vol.46, 2014, pp.1-7.
2. Schmidt M, Slowik V. "Instrumentation for optimizing concrete curing". *Concrete International*. 2013;35(8).
3. Lerch W. "Plastic shrinkage". *ACI journal proceedings*; ACI; 1957.
4. Ravina D, Shalon R. "Plastic shrinkage cracking". *ACI journal proceedings*; ACI; 1968.
5. "ACI D. 305R-hot weather concreting". *American Concrete Institute International,* 1999.
6. Boshoff WP, Combrinck R. "Modelling the severity of plastic shrinkage cracking in concrete". *Cement and Concrete Research*. Vol.48, 2013 JUN, pp.34-39.
7. Sivakumar A, Santhanam M. "Experimental methodology to study plastic shrinkage cracks in high strength concrete. In: Measuring, Monitoring and Modelling Concrete Properties. *Springer*, 2006. pp. 291-296.
8. Van Dijk J, Boardman V. "Plastic shrinkage cracking of concrete". RILEM international symposium of concrete and reinforced concrete in hot countries, Technion, Israel institute of technology, Haifa, 1971, pp. 225-239.
9. Kasai Y, Vokoyama K, Matsui I. "Tensile properties of early-age concrete. Proceedings of conference on mechanical behaviour of materials". 1972, pp.288-299.
10. Cohen MD, Olek J, Dolch WL. "Mechanism of plastic shrinkage cracking in Portland cement and Portland cement-silica fume paste and mortar". *Cement and Concrete Research,* Vol.20, No.1, 1990, pp.103-119.

11. Radocea A. "A study on the mechanism of plastic shrinkage of cement-based materials". Chalmers University of Technology,; 1992.

12. Almusallam A, Abdul-Waris M, Maslehuddin M, Al-Gahtani A. "Placing and shrinkage at extreme temperatures". *Concrete International*, Vol.21, 1999, pp.75-79.

13. Qi C, Weiss J, Olek J. "Characterization of plastic shrinkage cracking in fiber reinforced concrete using image analysis and a modified weibull function". *Materials and Structures*. Vol.36, No.6, 2003, pp.386-395.

14. Josserand L, Coussy O, de Larrard F. "Bleeding of concrete as an ageing consolidation process". *Cement and Concrete Research*,Vol.36, No.9, 2006, pp.1603-1608.

15. Esping O, Löfgren I, Marchand J, Bissonnette B, Gagné R, Jolin M, et al. "Investigation of early age deformation in self-compacting concrete". 2nd International Symposium on Advances in Concrete through Science and Engineering, 11-13 September 2006, Quebec City, Canada,

16. Dao V, Dux P, Morris P, O'Moore L. "Plastic shrinkage cracking of concrete". *Australian Journal of Structural Engineering*. Vol.10, No.3, 2010, pp.207-214.

17. Slowik V, Schmidt M. "Early age cracking and capillary pressure controlled concrete curing". *Advance in Cement-Based Material*. 2010.

18. Uno PJ. "Plastic shrinkage cracking and evaporation formulas". *ACI Mater Journal*. Vol.95, 1998, pp.365-375.

19. Ghoddousi P, Javid AAS. "Effect of reinforcement on plastic shrinkage and settlement of self-consolidating concrete as repair material". *Materials and Structures*, Vol.45, No.1-2, 2012, pp.41-52.

20. Combrinck R, Boshoff WP. "Typical plastic shrinkage cracking behaviour of concrete". *Magazine of Concrete Research*, Vol.65, No.8, 2013, pp.486-493.

21. Radocea A. "A model of plastic shrinkage". *Magazine of Concrete Research,*Vol.46, No.167, 1994, pp.125-132.

22. Bloem D. "Plastic cracking of concrete". *Engineering Information*. 1960.

23. Menzel CA. "Causes and prevention of crack development in plastic concrete". Proceedings of the Portland Cement Association. 1954, pp.130-136.

24. Goff JA, Gratch S. "Low-pressure properties of water from-160 to 212 F". *Transaction of the American Society Heating and Ventilating Engineers*, Vol.51, 1946, pp.125-164.

25. Powers TC. "The properties of fresh concrete". *John Wiley and sons,* 1969.

26. Kwak H, Ha S, Weiss WJ. "Experimental and numerical quantification of plastic settlement in fresh cementitious systems". *Journal of Material of Civil Engineering*, Vol.22, No.10, 2010, pp.951-966.

27. Standards Australia 1999. "Method for the determination of bleeding of concrete". 1999. Report No.: AS1012.6-1999.

28. ASTM C232/C232M. "Standard test method for bleeding of concrete". American Society of Testing and Material, 2013.

29. Slowik V, Schmidt M, Fritzsch R. "Capillary pressure in fresh cement-based materials and identification of the air entry value," *Cement and Concrete composites*, Vol.30, No.7, 2008, pp.557-565.

30. Khayat KH. "Workability, testing, and performance of self-consolidating concrete". *ACI Material Journal*, Vol.96, No.3, 1999.

31. Carman P. "Capillary rise and capillary movement of moisture in fine sands," *Soil Science*, Vol.52, No.1, 1941, pp.1-14.

32. Pihlajavaara S. "A review of some of the main results of a research on the ageing phenomena of concrete: Effect of moisture conditions on strength, shrinkage and creep of mature concrete," *Cement and Concrete Research,*Vol.4, No.5, 1974, pp.761-771.

33. Lund A, Skoog M, Thorstensson R. "Plastiska krympsprickor i betong",. Dept. of Structural Mechanics and Engineering, Royal Institute of Technology, Stockholm, Sweden, 1997. (in swedish)

34. Samman TA, Mirza WH, Wafa FF. "Plastic shrinkage cracking of normal and high-strength concrete: A comparative study," *ACI Material Journal*, Vol.93, No.1, 1996, pp.36-40.

35. Schiessl P, Schmidt R. "Bleeding of concrete," RILEM proceedings of the colloquium, Hanover, 1990, pp.24-32.

36. Lin S, Huang R. "Effect of viscosity modifying agent on plastic shrinkage cracking of cementitious composites," *Material and Structure*. Vol.43, No.5, 2010, pp.651-664.

37. Kronlöf A, Leivo M, Sipari P. "Experimental study on the basic phenomena of shrinkage and cracking of fresh mortar," *Cement and Concrete Research,* Vol.25, No.8, 1995, pp.1747-1754.

38. Soroka I. "Concrete in hot environments," CRC Press, 2003, 251 pp.

39. Cabrera J, Cusens A, Brookes-Wang Y. "Effect of superplasticizers on the plastic shrinkage of concrete," *Magazine of Concrete Research*, Vol.44, No.160, 1992, pp.149-155.

40. Hedin, C., "Plastiska Krympsprickor – Motåtgärder", Internal technical report 85-3. Central laboratory of Betongindustri AB, 1985, (in Swedish).

41. Cordon, W. A., Thorpe, J. D., "Control of Rapid Drying of Fresh Concrete by Evaporation Control", *ACI Journal,* Proceedings Aug. 1965, pp. 977-984.

Analysis of shallowly buried reinforced concrete pipelines subjected to earthquake loads

Roghayeh Abbasiverki
Doctoral student. MSc.
KTH Royal Institute of Technology
Division of Concrete Structures
SE-100 44 Stockholm, Sweden
E-mail: roghayeh.abbasiverki@byv.kth.se

Anders Ansell
Professor
KTH Royal Institute of Technology
Division of Concrete Structures
SE-100 44 Stockholm, Sweden
E-mail: anders.ansell@byv.kth.se

Richard Malm
Researcher. PhD.
KTH Royal Institute of Technology
Division of Concrete Structures
SE-100 44 Stockholm, Sweden
E-mail: richard.malm@byv.kth.se

ABSTRACT

Buried reinforced concrete pipelines are widely used in e.g. water and wastewater systems. Failure of these infrastructures may result in drastic effects and recently they have been brought into focus as vital components in safety systems for nuclear power installations. The high level of safety has here lead to a demand for reliable earthquake risk analyses. In this paper, methods are compared and the use of seismic design loads demonstrated. FE analysis in 2D of soil-pipe interaction under seismic wave propagation is performed. The performance of concrete pipes subjected to seismic waves with different frequency content is evaluated with respect to different soil condition but also water mass effect.

Key words: Modelling, Nuclear, Reinforcement, Structural Design.

1. INTRODUCTION

Buried pipelines are linear structures often used to transport important liquid materials and gas in order to support human life. The importance of this type of infrastructure systems has been brought into focus during the last years as they are vital components in the safety system for nuclear power installations. The high level of safety has led to a demand for reliable seismic analyses, also of structures built in areas that traditionally have not been considered as highly seismically active, such as in Sweden and the other Scandinavian countries [1-3]. During propagation of seismic waves in soil the components that propagate along the pipeline axis induce alternate axial compression and tension which cause axial deformations and the components of the waves that propagate in a direction perpendicular to the longitudinal axis cause bending deformations [4]. The induced damages largely depend on material and joints of the pipelines [5]. Therefore, they divide into two categories in terms of damage patterns; continuous (ductile) pipes and segmented (brittle) pipes. Empirical data from earthquake loads on pipelines indicates that the damage induced by wave propagation for brittle pipelines is more severe than for ductile pipelines which only show 30% of the vulnerability compared with the previous [6]. Continuous and segmented pipelines have different failure modes. Continuous pipelines often fail due to tensile rupture, local buckling (wrinkling) of the pipe wall due to axial compression and flexural failure and beam buckling (global buckling). The failure modes of segmented pipelines, especially of those with large diameters and thick walls, are tensile failure (axial pull-out), compression failure (crushing of joints), and circumferential flexure and joint rotation [7]. Reinforced concrete pipes (bell and spigot joints) and steel pipes (arc-welded joints) are widely used in buried water pipeline networks. The former are considered as segmented (brittle) pipes and the latter are classified as continuous (ductile) pipes. Compared with steel reinforced concrete is an economical and durable material, widely used in water and wastewater networks. On the other hand, as mentioned above, their vulnerability during ground shaking is higher than for steel pipes. Therefore, this paper is focused on studying the behaviour of reinforced concrete pipes.

1.1 Methods for seismic analysis of buried pipelines

Investigation on seismic behaviour of buried pipelines is traditionally performed using simplified methods presented by Newmark [8]. These methods neglect the soil-pipe interaction and assume that earthquake time histories for two points along the propagation path only differ by a time lag. This is a function of the separation distance between the two points and a wave propagating speed with wave velocity c_i relative to the ground surface. Using these assumptions, the obtained free field strain and curvature respectively are:

$$\varepsilon_{max} = \frac{PGV}{c_i} \tag{1}$$

$$k_{max} = \frac{PGA}{c_i^2} \tag{2}$$

Where PGV (Peak Ground Velocity) is the maximum horizontal ground velocity in the direction of wave propagation and PGA (Peak Ground Acceleration) is the maximum ground acceleration perpendicular to the direction of wave propagation. Yeh [9] expanded the Newmark

method for P (primary, longitudinal), S (secondary, shear) and Rayliegh waves propagating in a horizontal plane for situations where there is an angle in the horizontal plane between the pipe axis and the direction of propagation. Table 1 gives a summary of induced strain due to propagation of aforementioned waves where $v_{p\theta}$ and $a_{p\theta}$ are peak particle velocity and peak particle acceleration caused by P-waves, c_p is the apparent P-wave propagation velocity, $v_{s\theta}$ and $a_{s\theta}$ are the peak particle velocity and peak particle acceleration caused by S-waves, c_s is the apparent S-wave propagation velocity, $v_{R\theta}$ and $a_{R\theta}$ are the peak particle velocity and peak particle acceleration caused by R-waves, c_R is the apparent R-wave propagation velocity and θ is the angle of incidence of the wave with respect to the buried pipeline axis [9].

Wang et al. [10] presented a quasi-static analysis for axial displacement of long segmented buried pipelines modelled as a beam on an elastic foundation for considering soil-pipe interaction, and the pipeline itself was modelled by a set of rigid segments connected by flexible joints represented by elastic springs and dashpots. Vassilev et al. [11] adopted quasi-static analysis but used a two-dimensional plain strain finite element approach. Study on seismic response of buried pipelines continued using a lumped mass model of the pipe, also with soil-pipe interaction incorporated by a spring dashpot system whose reactions derived from static and dynamic continuum theories [12-16]. The beam model and lumped mass model describe the pipes as beams or masses, thus the real distribution of soil pressure and the distortion of the pipe cross section cannot be considered, which is most important for large diameter pipes. In order to also cover this case, a cylindrical shell model of the pipe was developed [17-22]. Among the above models, beams on nonlinear Winkler foundations (BNWF) are extensively used in practice due to their simplicity, mathematical convenience and ability to incorporate nonlinearity. This method was proposed by the American Lifelines Alliance (ALA) [23] and recently many authors have implemented it [24-30]. In this paper, two dimensional (plain strain) dynamic finite element models of reinforced concrete pipelines and surrounding interacting soil subjected to seismic waves with different frequency content have been studied.

Table 1- Summary of the strain induced in pipes (by neglecting the soil-pipe interaction) [9]

Wave type		Longitudinal strain	curvature
P-wave		$\varepsilon = \pm\left(v_{p\theta}/c_p\right)\cos^2\theta$ $\varepsilon_{\max} = \pm\left(v_{p\theta}/c_p\right)$ for $\theta = 0$	$k = \pm\left(a_{p\theta}/c_p^{\,2}\right)\sin\theta\cos^2\theta$ $k_{\max} = \pm\left(a_{p\theta}/c_p^{\,2}\right)$ for $\theta = 35°16'$
S-wave		$\varepsilon = \pm\left(v_{s\theta}/c_s\right)\sin\theta\cos\theta$ $\varepsilon_{\max} = \pm\left(v_{s\theta}/c_s\right)$ for $\theta = 45°$	$k = \pm\left(a_{s\theta}/c_s^{\,2}\right)\cos^3\theta$ $k_{\max} = \pm\left(a_{s\theta}/c_s^{\,2}\right)$ for $\theta = 0$
Rayleigh wave	Compressional component	$\varepsilon = \pm\left(v_{R\theta}/c_R\right)\cos^2\theta$ $\varepsilon_{\max} = \pm\left(v_{R\theta}/c_R\right)$ for $\theta = 0$	$k = \pm\left(a_{R\theta}/c_R^{\,2}\right)\sin\theta\cos^2\theta$ $k_{\max} = \pm\left(a_{R\theta}/c_R^{\,2}\right)$ for $\theta = 35°16'$
	Shear component		$k = \pm\left(a_{R\theta}/c_R^{\,2}\right)\cos^2\theta$ $k_{\max} = \pm\left(a_{R\theta}/c_R^{\,2}\right)$ for $\theta = 0$

1.2   Ground motion parameters

There are different parameters that describe the ground motion. In general, three characteristics of earthquake motion are of primary significance: the amplitude (e.g. PGA, PGV and PGD (peak ground displacement)), frequency content (e.g. Fourier spectra and response spectra) and duration of the motion. A number of ground motion parameters also provide information about more than one of these characteristics, an example for these parameters is spectrum intensity. Spectrum intensity is the area under the pseudo velocity response spectrum (S_v) within the period range 0.1-2.5 sec and can be computed for any structural damping ratio (ξ). It indicates the earthquake severity and captures amplitude and frequency content in the range of interest for many structures [31-32]. This parameter is in displacement dimension and if divided by 2.4 sec as in Eq. (1) it takes a value similar to the maximum velocity of ground motion which is suitable for illustration of the induced damage on buried pipelines during wave propagation. In Japan, a device called SI sensor for gas supply networks has been designed. To avoid secondary disasters caused by gas leaks, monitored SI values that exceed 30 to 40 cm/sec stop the gas supply automatically [33]. This value is calculated as:

$$SI = \frac{1}{2.4} \int_{0.1}^{2.5} S_v(T, \xi) \, dT \tag{3}$$

2.   EARTHQUAKE LOADS

For a seismic analysis it is important to know which load parameters will affect the seismic response of buried pipelines. Therefore, earthquakes of different characteristics have been selected for this study; artificial accelerograms corresponding to the Swedish hard rock response spectra [34] and accelerograms recorded at CDMG 23598 Rancho Cucamonga - Deer Can station [35]. The average shear wave velocity was equal to 821.70 m/s during this 1994 Northridge earthquake where the epicentral distance for this record is 89.83 km. The former earthquake has high acceleration and short dominating period and is therefore in the following referred to as a high frequency earthquake and the latter that has lower acceleration but longer dominating period, is called a low frequency earthquake. In this study, the Northridge earthquake was scaled to have the same PGA as design earthquake of Sweden (see Table 2). Figures 1 and 2 illustrate acceleration time histories and an example of response spectrum for aforementioned earthquakes. Vertical and horizontal ground acceleration time histories are applied at the base of the soil-pipe models by assuming that the soil rests on the bedrock.

Table 2- Ground motion parameters [36]

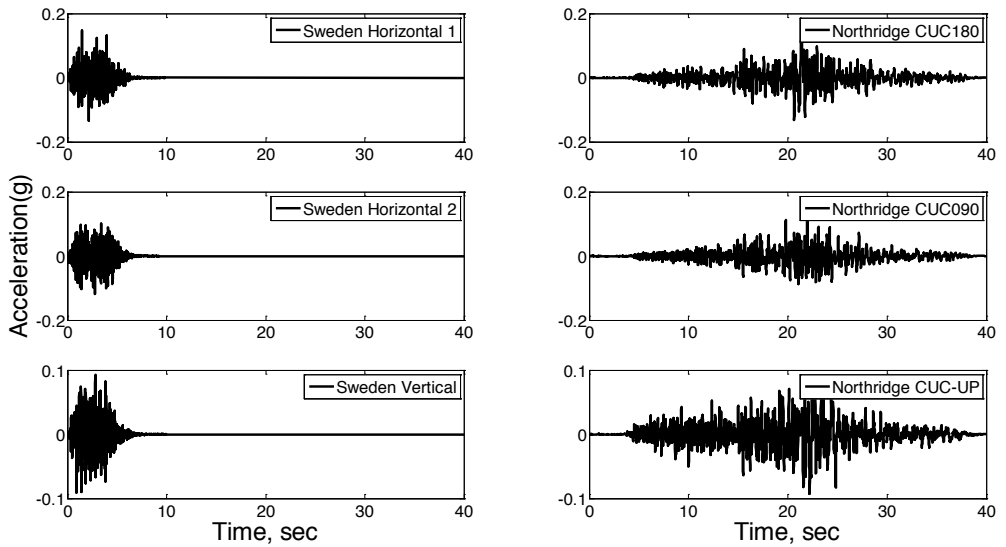| Location	PGA (g)	PGV (cm/sec)	PGD (cm)	Predominate period (sec)	Velocity spectrum intensity ($\xi = 5\%$) (cm/sec)
Sweden	0.146	2.99	0.61	0.08	3.72
Northridge (scaled)	0.146	15.45	1.87	0.28	19.65
Northridge (unscaled)	*0.072*	*5.91*	*0.70*	*0.28*	*7.61*

Figure 1 - Acceleration time history for applied seismic loads
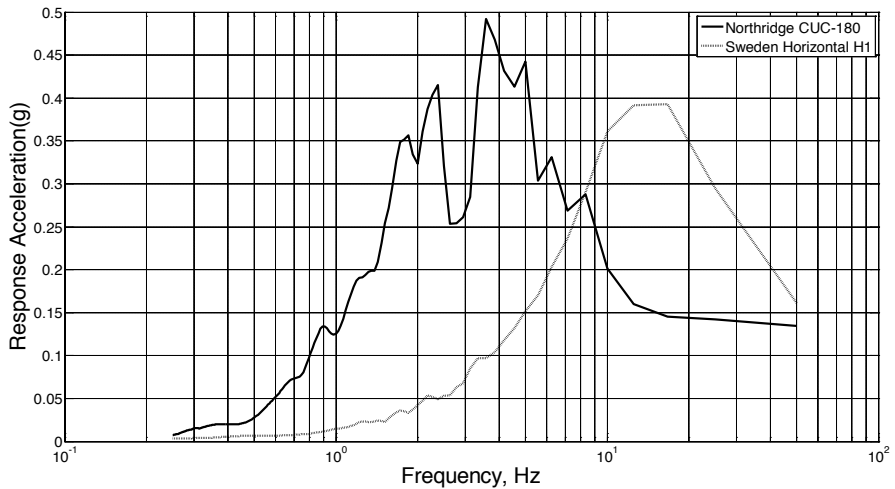

Figure 2 – Example of frequency spectra for the applied seismic loads (horizontal component)

3.   BURIED PIPE SYSTEMS

A typical reinforced concrete pipe (bell and spigot joint) with 1200 mm nominal diameter and 135 mm wall thickness (*t*) which commonly is used in water and wastewater networks in Sweden is selected for the study (see Figure 3). Material qualities C45/55 and B500B are

assigned for concrete and steel reinforcement, respectively [37]. Two types of frictional soil that are close to Sweden condition is adopted; first one with medium stiffness and second one with hard stiffness. Their density respectively are 1800 kg/m³ and 2200 kg/m³, the soil friction angle 38 degrees and 45 degrees and with shear wave velocity respectively equal to 250 m/s and 450 m/s [38].
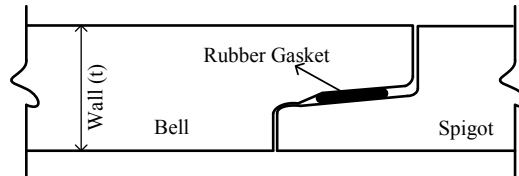

Figure 3 - Schematic of concrete pipes joint [39]

4. FINITE ELEMENT MODELLING

Seismic finite element modelling of buried concrete pipes has been performed using the ABAQUS/Standard finite element program [40]. The simulation is done in a two dimensional plane strain system. Two different models have been considered; the first model presents longitudinal cross section of an RC pipe where the simulated length of the pipe is equal to *L*=150 m and effect of the joints is neglected. The second model describes a transverse cross section of an RC pipe. The relevant width (*Z*) for this model will be discussed in next section. Distance between ground surface and bed rock is assumed to be *W*=25 m and the burial depth, i.e. the distance between ground surface and centre of pipe, is here *H*=1 m (see Figures 4 and 5). The finite element meshes consist of 4-node bilinear plane strain quadrilateral (CPE4R) elements for the soil medium and pipe cross section, 3-node quadratic 2D truss (T2D3) elements for reinforcement and 2-node linear 2D beam (B21) elements for longitudinal cross sections of pipes. Reinforcement in the pipe cross section has been modelled as embedded discrete truss elements tied to the concrete region. The interaction between reinforcement and concrete elements is assumed as fully bonded.
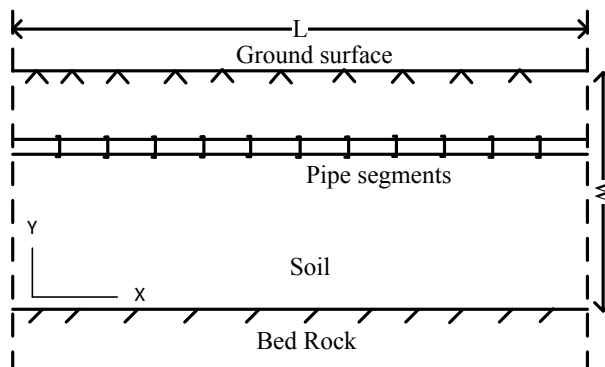

Figure 4 - Schematic view of finite element domains for longitudinal plane model
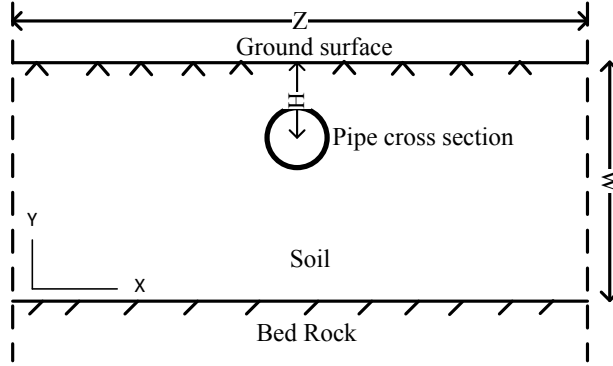
Figure 5- Schematic view of finite element domains for cross section plane model

4.1   Absorbing boundary condition

In a dynamic soil-structure interaction analysis using the finite element method, the computational region must be truncated from the infinite space. It is necessary to introduce artificial boundaries to represent both elastic continuity of the soil and radiation damping. Two kinds of methods are used to set up artificial boundary; global and local procedures, respectively. The former are rigorous, but complex and computationally expensive, e.g. as boundary element method and scaled boundary finite element method. The latter are generally approximate but simple and widely used in civil engineering, e.g. as viscous boundary and infinite elements. In order to obtain accurate results, local artificial boundaries have to be placed sufficiently far away from the structure-soil interface [41].

In this study infinite elements (CINPE4) provided by ABAQUS are implemented. These elements consider both static and dynamic response (see [40]). An infinite element boundary is a kind of implementation of a viscous boundary to absorb the energy in a dynamic analysis and consists of normal and tangential dampers with coefficients C_n and C_t respectively. These are defined as:

$$C_n = \rho\, V_p = \sqrt{\rho\,(\lambda + 2G)} \tag{4}$$

$$C_t = \rho\, V_s = \sqrt{\rho\, G} \tag{5}$$

$$G = E/2(1+\upsilon) \tag{6}$$

$$\lambda = \frac{E\upsilon}{(1+\upsilon)(1-2\upsilon)} \tag{7}$$

where V_s is shear wave velocity, G shear modulus, V_p compression wave velocity, E Young's modulus, υ Poisson's ratio, ρ mass density and λ is the Lame's constant [42]. Infinite elements are linear elements, and it is necessary to place them at a reasonable distance from the structure

since the amplitude of stress will decrease with increasing distance and consequently they restrict the nonlinearity to the finite element domain. For this reason a convergence analysis has been performed. Relevant distance between boundary structure surface was found to be larger than $2W$ (i.e. $Z/2 > 2W$). Therefore, the soil width was set to $Z=6H=150$ m.

4.2 Soil-pipe interaction

The most important part of a seismic analysis of buried pipelines is to introduce the interaction behaviour at soil and pipe interface since the soil deformations resulting from seismic waves impose forces and deformations on the pipes and may cause severe damages on buried pipeline networks. Herein the soil-pipe interaction is modelled with SPRING2 elements at the soil-pipe interface [40]. The spring behaviour is calculated from elastic-plastic models proposed by the American Lifeline Alliance (ALA) [23] which can describe the slip of pipes in soil when the earthquake is strong. The springs are distributed in three perpendicular directions with respect to pipe, see Figure 6.
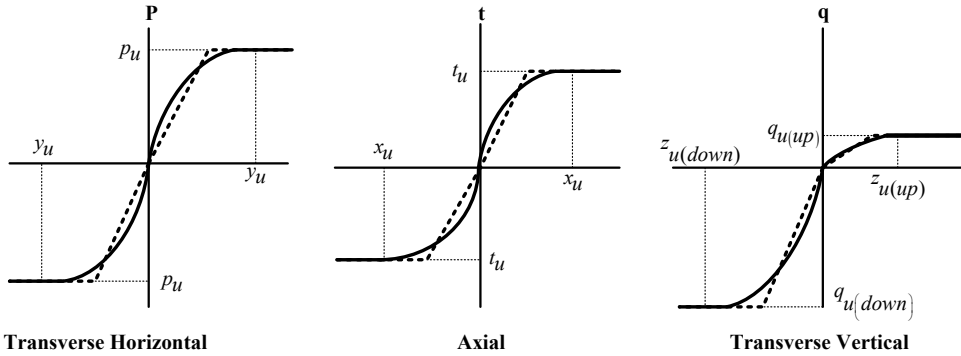

Figure 6 - Load-deformation relationships for spring elements representing soil-pipe interaction

Axial spring

Maximum soil resistance to movement in the pipe axial direction is given in units of force per unit length of pipe, as:

$$t_u = \pi D c \alpha + \pi D H \bar{\gamma} \frac{1+K_0}{2} \tan \delta' \frac{1}{2} \tag{8}$$

$$\alpha = 0.608 - 0.123 c - \frac{0.274}{c^2+1} + \frac{0.695}{c^3+1} \tag{9}$$

These soil spring are picked up from pile shaft load transfer theory, where D is outside diameter of pipe, c coefficient of cohesion of backfill soil, H depth of soil above the centre of the pipeline, $\bar{\gamma}$ is effective unit weight of soil, α adhesion factor, $\delta' = f \times \phi$ interface angle of

friction between pipe and soil, ϕ internal friction angle of the soil, f friction factor for various types of pipes (equal to 1 for concrete) and $K_0 = 1 - \sin \phi$ is coefficient of soil pressure at rest. An ultimate relative displacement (x_u) corresponding to maximum soil resistance (t_u) is 3 to 5 mm for sand and 8 to 10 mm for clays.

Lateral Soil Spring

The maximum lateral resistance of soil per unit length of pipe can be calculated as:

$$p_u = N_{ch} c D + N_{qh} \bar{\gamma} H D \tag{10}$$

$$N_{ch} = a_1 + a_2 x + \frac{a_3}{(x+1)^2} + \frac{a_4}{(x+1)^3} \le 9 \tag{11}$$

$$N_{qh} = a_1 + a_2 x + a_3 x^2 + a_4 x^3 + a_5 x^4 \tag{12}$$

These soil springs are picked up from footing and vertical anchor plate pull-out capacity theory and laboratory tests on model pipelines simulating horizontal pipe movements, where N_{ch} is horizontal bearing capacity factor for clay (zero for $c = 0$), N_{qh} is horizontal bearing capacity factor for sandy soil (zero for $\phi = 0$). Relative displacement y_u at p_u, can be determined by:

$$y_u = 0.04 \left(H + \frac{D}{2} \right) \le 0.01D \quad \text{to} \quad 0.02D \tag{13}$$

The above parameters are found in ALA [23] and are here listed in Table 3.

Table 3 - Parameters for the evaluation of N_{ch} and N_{qh}. From [23]

Factor	ϕ	x	a_1	a_2	a_3	a_4	a_5
N_{ch}	0	H/D	6.752	0.065	-11.063	7.119	-
N_{qh}	20	H/D	2.399	0.439	-0.03	1.059×10^{-3}	-1.754×10^{-5}
N_{qh}	25	H/D	3.332	0.839	-0.090	5.606×10^{-3}	-1.319×10^{-4}
N_{qh}	30	H/D	4.565	1.234	-0.089	4.275×10^{-3}	-9.159×10^{-5}
N_{qh}	35	H/D	6.816	2.019	-0.146	7.651×10^{-3}	-1.683×10^{-4}
N_{qh}	40	H/D	10.959	1.783	0.045	-5.425×10^{-3}	-1.153×10^{-4}
N_{qh}	45	H/D	17.658	3.309	0.048	-6.443×10^{-3}	-1.299×10^{-4}

Vertical Soil Spring

The soil spring properties are different for uplift and bearing cases. The maximum soil resistance per unit length of the pipeline in vertical uplift can be calculated as:

$$q_{u(up)} = N_{cv}cD + N_{qv}\bar{\gamma}HD \tag{14}$$

$$N_{cv} = 2\left(\frac{H}{D}\right) \leq 10 \quad \text{for} \quad \left(\frac{H}{D}\right) \leq 10 \tag{15}$$

$$N_{qv} = \left(\frac{\phi H}{44D}\right) \leq N_q \tag{16}$$

The properties of these soil springs are from pull-out capacity theory and laboratory tests on anchor plates and model buried pipe, where N_{cv} is vertical uplift factor for clay (0 for $c = 0$), N_{qv} is vertical uplift factor for sand (0 for $\phi = 0°$). The mobilizing displacement of soil, $z_{u(up)}$ at $q_{u(up)}$ can be taken as $0.01H$ to $0.02H$ for sands and $0.1H$ to $0.2H$ for clay. The maximum soil resistance per unit length of pipeline in vertical bearing can be calculated as:

$$q_{u(down)} = N_c cD + N_q \bar{\gamma} HD + N_\gamma \gamma \frac{D^2}{2} \tag{17}$$

$$N_c = \left(\cot(\phi + 0.001)\right)\left(\exp\left[\pi \tan(\phi + 0.001)\right]\tan^2\left(45 + \frac{\phi + 0.001}{2}\right) - 1\right) \tag{18}$$

$$N_q = \exp\left[\pi \tan \phi\right]\tan^2\left(45 + \frac{\phi}{2}\right) \tag{19}$$

$$N_\gamma = \exp\left[0.18\phi - 2.5\right] \tag{20}$$

These soil springs are picked up from bearing capacity theory for footings, where N_c, N_q and N_γ are bearing capacity factors and γ is total unit weight of soil. The soil displacement, $z_{u(down)}$ at $q_{u(down)}$ can be taken as $0.1D$ for granular soils and $0.2D$ for cohesive soils.

4.3   Damping

Material damping is another important parameter which defines the attenuation of the internal energy generated from seismic loading. Generally, damping effects can be considered in systems using two different methods; Modal damping and Rayleigh damping where the latter is applicable in direct-integration dynamic analysis. In the Rayleigh damping model, the damping matrix $[C]$ is a linear combination of the mass matrix $[M]$ and stiffness matrix $[K]$:

$$[C] = \alpha[M] + \beta[K] \tag{21}$$

where α is mass damping coefficient and b a stiffness damping coefficient. Rayleigh damping is described by the following equation:

$$\xi_i = \frac{\alpha}{2\omega_i} + \frac{\beta\omega_i}{2}$$

(22)

This equation produces a curve which is a function of natural frequency $\omega_i = 2\pi f$ and Rayleigh damping coefficients (α and β) and implies that the mass proportional Rayleigh damping α is effective for the lower frequencies and the stiffness proportional Rayleigh damping β has influence on the higher frequencies [43]. Modal damping for the materials is here assumed equal to 5%. Frequency analysis has been performed and frequency interval and Rayleigh damping coefficients for two model materials calculated (see Table 4). Aforementioned frequency intervals will capture characteristic frequencies of soil with the following equation [42]:

$$f = \frac{V_s}{4W}$$

(23)

Table 4 - Rayleigh damping coefficients

Damping parameters	Longitudinal cross section model		Transverse cross section model	
	Medium soil	Dense soil	Medium soil	Dense soil
α	1.00853	1.88725	1.26367	2.16877
β	0.0015907	0.00089188	0.00096646	0.00053439
Frequency interval	2.2 - 7.3	4 – 13.4	2.3 - 14.4	4 - 25.7

5. NUMERICAL EXAMPLES

In the following, results from examples based on FE models in accordance to the geometries presented in section 4 and Figures 4-5 are presented. The two models are two- dimensional plane models and here referred to as longitudinal plane section and axial plane cross-section models, respectively. The two earthquake loads defined in Figure 1 and Table 2, i.e. the Swedish design earthquake and the Northridge earthquake, are used as seismic loads for the analyses. The effects of the two frictional soil types referred to as medium stiff and dense in section 3 are investigated. The effect of empty or completely water filled pipes are also studied. It should be noted that wave effects in the water and interaction between the water and the inside of the pipe are not included in the model. Thus, when water is added, the mass of the pipe system is increased. However, the added water does not contribute to the stiffness or directly to the damping of the system, other than through the assumed Rayleigh damping (see section 4.3).

5.1 Effective modal mass

One important property of the two FE models used for the following examples is the effective modal mass, defined such that the sum of all effective masses in any direction will give the total mass of the model, subtracted with masses at kinematically restrained degrees of freedom [40]. Thus, the difference between the total mass and the sum of effective mass is a measure of which modes that participates in the excitation in the chosen direction. Here, cumulative masses for the

two models are given in Figures 7-8, indicating which natural frequencies and vibration modes significantly contribute to the vibrations, until the entire mass is activated. The effective mass for mode n in the direction i is defined as:

$$m_{ni}^{\text{eff}} = \left(\Gamma_{ni} \right)^2 m_n = \left(\Gamma_{ni} \right)^2 \phi_n^{\text{T}} [M] \phi_n \tag{24}$$

where m_n is the generalized mass, ϕ_n the free vibration mode n, $[M]$ the mass matrix and:

$$\Gamma_{ni} = \frac{1}{m_n} \phi_n^{\text{T}} [M] T_i \tag{25}$$

is the participation factor, with T_i being the magnitude of the rigid body response at a degree of freedom in the model caused by rigid body motion in the i-direction (see [40]).
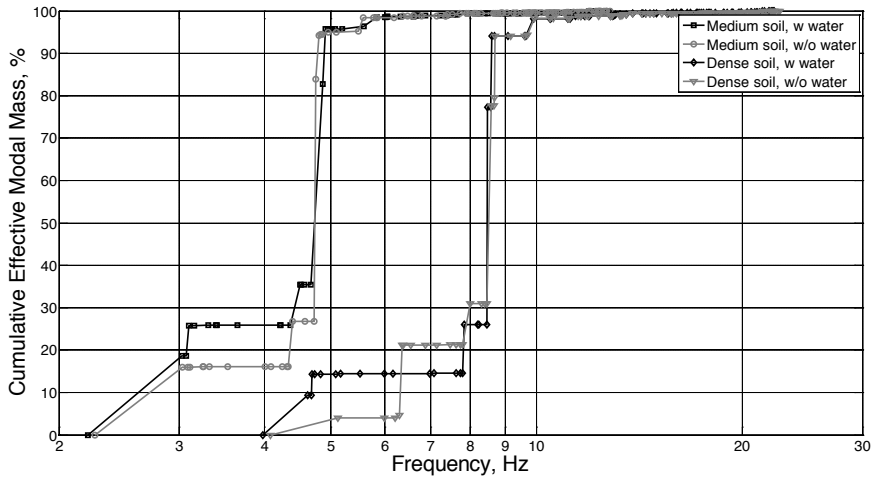
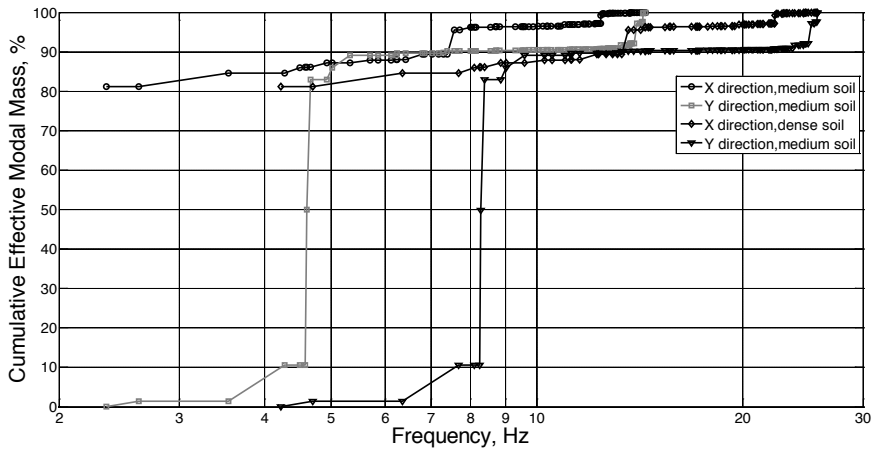*Figure 7 - Cumulative effective modal mass in direction y for the longitudinal plane section model*

Figure 8 - Cumulative effective modal mass for the axial plane cross-section model

5.2 Dynamic analyses – longitudinal plane section

The results from the model of the longitudinal plane section are presented in Figures 9-12, first showing results obtained for the Northridge earthquake followed by results for the Swedish design earthquake. The calculated maximum tensile stresses are presented as stress envelopes, i.e. the maximum stress that occurs at each section of the pipe length during the time span considered in the analysis. When studying the curves, it should therefore be noted that these do not show stress distributions and that the maximum stresses on the left and right sides do not necessarily occur simultaneously. The maximum stresses appear close to the ends but are lowest at the pipe centre. This is due to the symmetry over the normal line to the earthquake epicentre. There are also small stresses at the ends of the pipes caused by the pipe-soil interaction. In the two pairs of figures, Figures 9 and 11 show the stress that occur due to axial tension in the pipes while Figures 10 and 12 show the maximum of the bending tensile stresses. Each figure contains four curves representing the combinations of the cases with empty or water filled pipes and dense or medium hard surrounding soil, respectively.

5.3 Dynamic analyses – axial plane cross-section

The maximum principal (tensile) stresses obtained for the model of an axial plane cross-section are presented in Figure 13. The position of these stresses, which occur in the circular plane section of the pipe, is given using polar angles, positive in the clockwise direction and originating from the position with the upwards direction, as shown in Figure 13. It should be noted that the results from the Northridge earthquake are divided between subfigures (a) and (b), separated due to the large differences in maximum stress, while the results for the Swedish design earthquake are shown in subfigure (c).
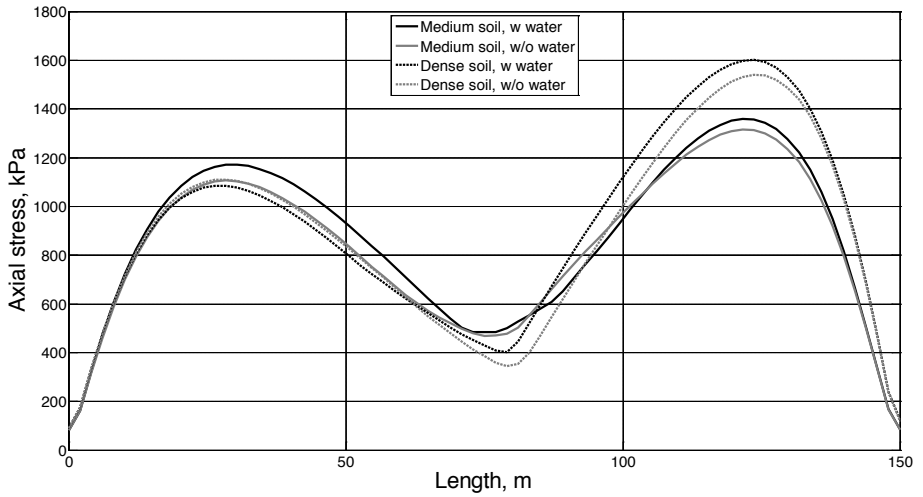
Figure 9 - Axial stress for the longitudinal plane section model subjected to the Northridge earthquake
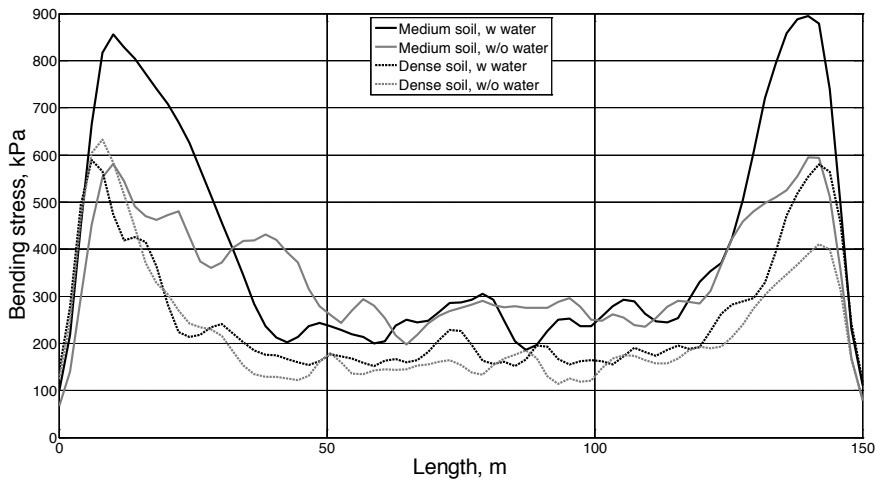

Figure 10 - Bending stress for the longitudinal plane section model subjected to the Northridge earthquake
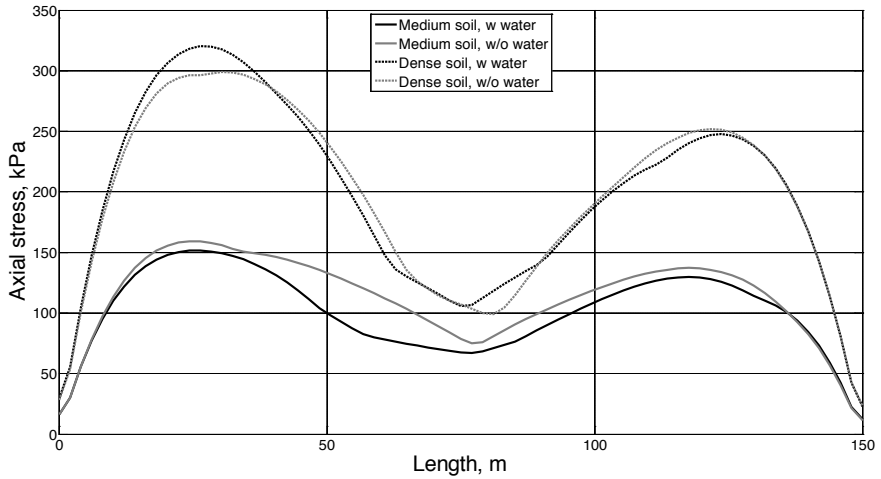
Figure 11 - Axial stress for the longitudinal plane section model subjected to the Swedish design earthquake
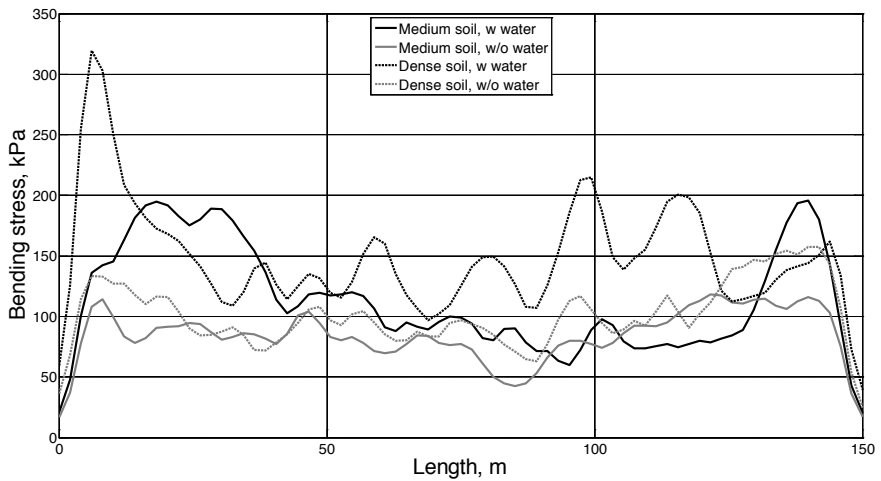

Figure 12 - Bending stress for the longitudinal plane section model subjected to the Swedish design earthquake
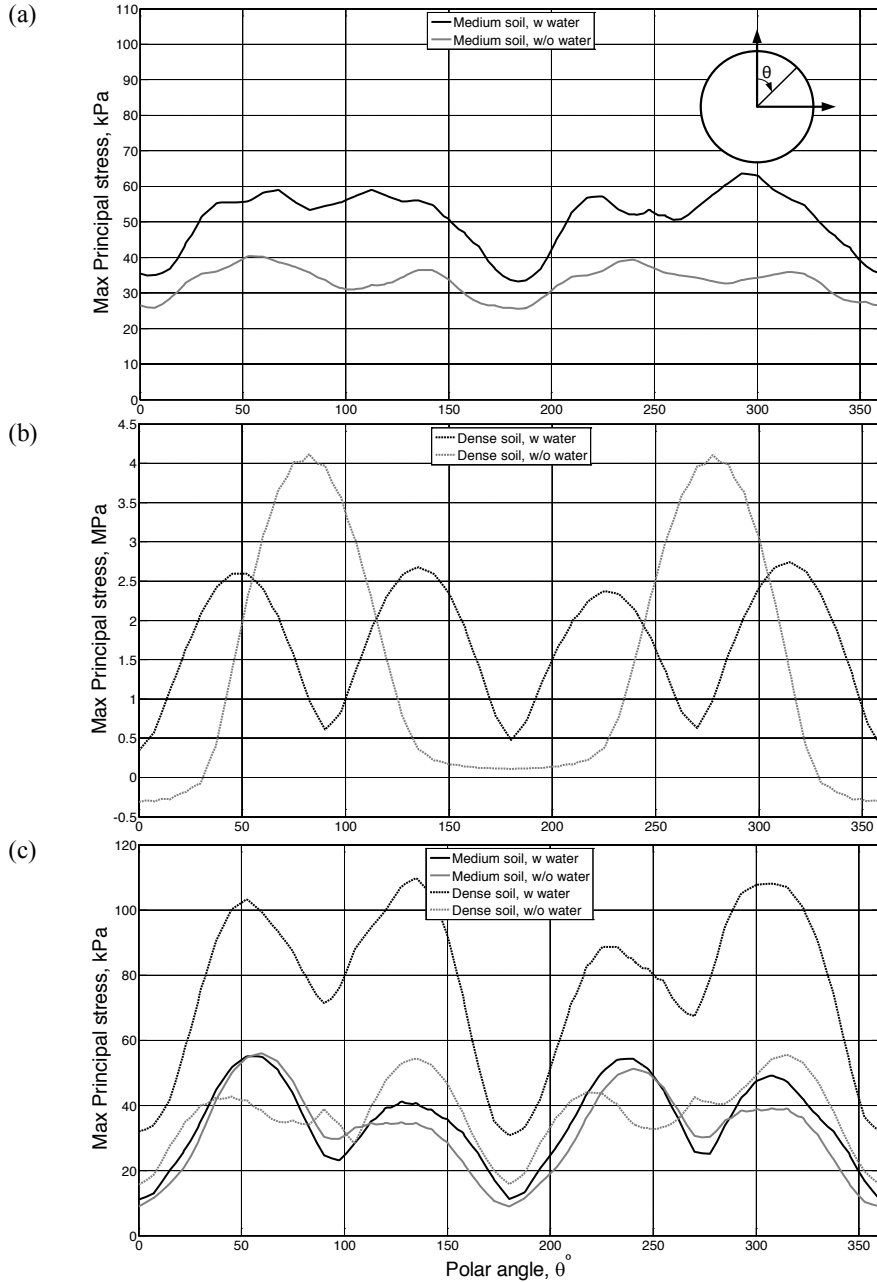
Figure 13 - Maximum principal stress for the axial plane cross-section model subjected to the Northridge earthquake (a-b) and the Swedish design earthquake (c).

6. DISCUSSION

It should be noted that the geometry used for the models is for a reference cases with the purpose of analysing the influences of parameters such as seismic input, soil type and the influence of water-filled pipes. The chosen geometry of the studied pipe-soil system results in maximum tensile concrete stresses, obtained with the longitudinal plane section model, that are close to the design value given in Eurocode 2 [37]. The results using the model with the axial plane cross-section indicate concrete tensile failure, i.e. tensile cracking and leakage, for some combinations of input parameters.

6.1 Evaluation of results

The diagrams of the variation of modal mass shown in Figures 7-8 demonstrate that the dominant free vibration modes correspond to frequencies around 4.5 Hz for the cases with medium stiff soil and around 8.5 Hz for dense soil. This should be compared to the earthquake load spectra given in Figure 2, where it can be seen that the dominant frequencies for the Northridge earthquake are at 2-5 Hz, while the corresponding frequencies for the Swedish design earthquake are at 10-12 Hz. The differences shown in Figure 7, between the curves representing empty and water filled pipes at 3-4 Hz and 5-9 Hz, respectively, are due to changes in the bending modes as water is added to the mass.

When comparing the four combinations of input parameters, there are small differences in axial tensile stresses obtained with the Northridge earthquake, as can be seen in Figure 9. In this case, the maximum tensile stress becomes 1.6 MPa, which is close to the design strength of 1.8 or 2.2 MPa [37] and obtained for the dense soil type. The effect of including the mass of the water in the pipe has a relatively low impact on the axial tensile stress. In the case of bending stresses, Figure 10 shows that the Northridge earthquake results in lower tensile stresses. However, the differences are in this case greater when comparing the cases with or without water filled pipes and different soil density. With medium dense soil and water filled pipes the tensile bending stresses reach 900 kPa while the corresponding stress with empty pipes becomes 600 kPa. The inclusion of water in the pipe is not noticeable for the case with dense soil and it can also be observed that for empty pipes and medium dense soil the result is close to the cases with denser soil. Thus, including the mass of the water increases the bending stresses when the soil is medium hard, i.e. when it provides a relatively small resistance to bending vibrations. As shown in Figures 11-12 the tensile stresses become much smaller with the Swedish design earthquakes. In the axial direction the relative effect from a denser soil is much greater in this case, leading to twice the stress levels compared to the case with medium dense soil. The effect from an added mass of water becomes almost negligible and this case is thus stiffness dominated where stiffer soil in combination with a high frequency content of the earthquake load produces high stresses. As shown in Figure 12, there are small variations in bending tensile stresses in this case. The maximum levels are reached with water included and some stress peaks occur locally along the length of the pipe, for the case with included water and dense soil.

The results obtained with the model of the axial plane cross-section show large differences in maximum tensile stress, as can be seen in Figure 13. The maximum principal stress in almost all cases show four maximum peaks that correspond to the approximate positions 45°, 135°, 225° and 315°, respectively. The one exception from this pattern is also the case that show the highest stress levels, obtained for the Northridge earthquake with dense soil and empty pipes, see subfigure (b). In the similar case but with water filled pipes the combination of input parameters

creates also high stress levels and concrete failure. However, in this case four maximum stress peaks are shown. In the remaining cases the maximum stress levels within 40-60 kPa, i.e. almost 100 times lower, for four of the combinations of parameters. However, with the Swedish design earthquake, higher stresses are reached for water filled pipe and dense soil, see subfigure (c). This indicates that the water mass has an effect on the ring stresses of the pipes, for both types of earthquakes but with a much larger impact when lower frequencies dominate. It should be noted that the maximum stress levels, except for the two extreme cases shown in subfigure (b), are lower than or equal to those observed in bending.

6.2   Conclusions

The results demonstrate how 2D plane strain models can be used for seismic analysis of concrete pipelines with circular cross sections. The two different models used have characteristic, natural frequencies within the same range. The geometry and material parameters were chosen to demonstrate the behaviour under typical conditions for large diameter, shallowly buried concrete pipes. The results show that for the conditions chosen, the design earthquake recommended for Sweden produces tensile stresses that are much lower than the concrete strength. However, the American earthquake record (Northridge) used for comparison gave relatively high stresses due to axial pipe deformation and local stresses in the pipe ring segments which would cause damage for unfavourable combinations of soil stiffness and degree of water filling. Thus, modelling the pipe-soil system with beam elements only cannot represent the exact response of soil-pipe systems as in some cases the ring stress become much higher than the axial and bending stress. The earthquakes used for the comparison had comparable levels of peak ground acceleration PGA but different dominant frequency ranges. The low frequency American earthquake was closer to the dominant frequencies in the pipe-soil FE models and, consequently, produced much higher stresses. It can be concluded that PGA is not a relevant parameter for evaluation of the damage due to earthquakes and other parameters related to both amplitude and frequency content should be selected instead.

Future work will focus on finding combinations of parameters where the relatively high frequency content of the Swedish design earthquake will cause damage to the pipelines. The work will include comparisons between shallow and deep pipes, also including further soil types, e.g. cohesive soils. Cases with pipelines spanning areas with variable soil depths to the bedrock will also be included. The efficiency of concrete pipelines will be compared to that of steel pipes to determine under which conditions the two alternatives, i.e. light and stiff vs. brittle and heavy, are most efficient.

REFERENCES

1. Rydell, C., "Seismic high-frequency content loads on structures and components within nuclear facilities", Bulletin 123, KTH Civil and Architectural Engineering, Stockholm, 2014.
2. Tabatabaei Araghi, P., "Seismic analysis of concrete structures within nuclear industry", Master Thesis, KTH Civil and Architectural Engineering, Stockholm, 2014.
3. Drivas, G.V., "Cost evaluation of seismic load resisting systems based on the ductility classes in Eurocode 8", Master Thesis, KTH Civil and Architectural Engineering, Stockholm, 2014.

4. Owen, G.N., Scholl, R.E, "Earthquake engineering of large underground structures", Federal Highway Administration and National Science Foundation, Washington, D.C, USA, 1981.

5. Lanzano, G., Salzano, E., Santucci De Magistris, F., Fabbrocino, G., "An observational analysis of seismic vulnerability of industrial pipelines", *Journal of Chemical Engineering Transaction*, 26, 2012, 567-572.

6. FEMA: HAZUS-MH MR4, "Multi-hazard loss estimation methodology, earthquake model", Technical Manual, National Institute of Building Science, Washington, D.C., 2003.

7. O'Rourke, M.J., Liu X., "Response of buried pipelines subjected to earthquake effects", MCEER Monograph: 3, University of New York, Buffalo, USA, 1999.

8. Newmark, N.W., "Problems in wave propagation in soil and rock", Proc. Int. Symposium on Wave Propagation and Dynamic Properties of Earth Materials, Albuquerque, New Mexico, 1967, 7-26

9. Yeh, G.K, "Seismic analysis of slender buried beams", Bulletin of the Seismological Society of America., 64:5, 1974, 1551-1562.

10. Wang, L.R.L., Cheng, K.M. "Seismic response behaviour of buried pipelines", *Journal of Pressure Vessel Technology, ASME*, 101:1, 1979, 21-30.

11. Vassilev, V.H., Flores-Berrones, R., "Seismic analysis of segmented buried pipelines", Proceeding of Eleventh World Conference on Earthquake Engineering, 1986, Paper no. 1586.

12. Hindy, A., Novak, M., "Earthquake response of underground pipelines", *International journal of Earthquake Engineering and Structural Dynamics*, 7, 1979, 451–476.

13. Novak, M., Hindy, A., "Seismic analysis of underground tubular structures", Proceeding of the Seventh World Conference Earthquake Engineering, 8, 1980, 287–294

14. Datta, T.K.., Mashaly, E.A., "Pipeline response to random ground motion by discrete model", *International journal of Earthquake Engineering and Structural Dynamics*, 14, 1986, 559–572.

15. Datta, T.K., Mashaly, E.A., "Seismic response of buried submarine pipelines", Transactions of the ASME, *Journal of Energy Resources Technology*, 1988, 208–218.

16. Hindy, A., Novak, M., "Pipeline response to random ground motion" *Journal of the Engineering Mechanics Division*, 106, 1980, 339–360.

17. Muleski, G.E., Ariman, T., Aumen, C.P., "A shell model for buried pipes in earthquakes", *Journal of soil dynamics and earthquake engineering*, 4, 1985, 43–51.

18. Takada, S., Tanabe, K., "Three dimensional seismic response analysis of buried continuous or jointed pipelines", *Journal Pressure Vessel Technology, ASME*, 109, 1987, 80–87

19. Yang, R., Kameda, H., Takada, S., "Shell model FEM analysis of buried pipelines under seismic loading", Bull. Disas. Prey. Res. Inst., Kyoto Univ., 38:336, 1988, 115-146.

20. S. K. Datta, P. M.O'Leary, A. H. Shah, "Three-dimensional dynamic response of buried pipelines to incident longitudinal and shear waves", *Journal of Applied Mechanics*, 52:919, 1985, 915-926.

21. Kouretzis, G.P, Bouckovalas, G.D, Gantes, C.J., "3-D shell analysis of cylindrical underground structures under seismic shear (S) wave action", *Journal of Soil Dynamic Earthquake Engineering*, 26, 2006, 909-921

22. Kouretzis, G.P., Bouckovalas, G.D., Karamitros, D.K., "Seismic verification of long cylindrical underground structures considering Rayleigh wave effects", *Journal of Tunnelling and Underground Space Technology*, 26, 2011, 789-794.

23. American Lifelines Alliance (ALA), "Buried Steel Pipes", American Society of Civil Engineers (ASCE) & Federal Emergency Management Agency (FEMA), 2001.

24. Lee, D.H., Kim, B.H., Lee, H., Kong, J.S., "Seismic behaviour of a buried gas pipeline under earthquake excitations", *Journal of Engineering Structures*, 31, 2009, 1011–1023.

25. Hosseini, M., Roudsari, M.T., "A study on the effect of surface transverse waves on buried steelpipelines considering the nonlinear behaviour of soil and pipes", Proceedings of the ASCE Pipeline Conference, Kingston, Colorado, USA, 2010, 1078-1087.

26. Saberi, M., Behnamfar, F., Vafaeian, M., "A semi-analytical model for estimating seismic behavior of buried steel pipes at bend point under propagating waves", *Bulletin of Earthquake Engineering Journal*, 11, 2013, 1373–1402

27. Hosseini, M., Jalili, S., Azizpour, O., Alikhani, M., "Evaluating the functionality of water distribution networks in the aftermath of big earthquakes based on nonlinear modeling of pipes connections", Proceedings of the ASCE Pipeline Conference, Kingston. Colorado, USA, 2010.

28. Roudsari, M.T., Hosseini, M., "Using neural network for reliability assessment of buried steel pipeline networks subjected to earthquake wave propagation", *Journal of Applied Sciences,* 11:18, 2011, 3233-3246.

29. Sadat Shokouhi, S.K., Mokhlespour, M.E., "Optimal sensor placement for bolted-gland joints in the water pipeline networks subjected to near-fault and far-fault earthquakes", Proceedings of the International Conference on Pipelines and Trenchless Technology, Xi'an, China, 2013.

30. Sadat Shokouhi, S.K., Dolatshah, A., Vosoughifar1, H.R., Hosseininejad, S.Z., Rahnavard, Y., "Optimal sensor placement of TYTON joints in the water pipeline networks Subjected to near-fault and far-fault earthquakes", Proceedings of the Pipelines Conference, Fort Worth, Texas, 2013.

31. Kramer, S.L., "Geotechnical earthquake engineering", Prentice-Hall, Upper Saddle River, NJ, 1996.

32. Housner, G.W., "Intensity of ground motion during strong earthquakes", ONR Report, 1952, 1-60.

33. Nakayama, W., Shimizu, Y., Koganemaru, K., "Development of super dense real-time disaster mitigation system for urban gas supply network", *Journal of Japan Association for Earthquake Engineering*, Special Issue, 2004, 124-127.

34. Swedish Nuclear Power Inspectorate (SKI), Seismic safety – Characterization of seismic ground motions for probabilistic safety analyses of nuclear facilities in Sweden, Stockholm, 1992.

35. Pacific Earthquake Engineering Research Center (PEER), 2014, http://peer.berkeley.edu/

36. Seismosoft, 2014, http://www.seismosoft.com/en/SeismoSignal.aspx

37. Eurocode 2, "Design of concrete structures, European Standard EN 1992-1-1. European Committee for Standardisation (CEN), Brussels, 2004.

38. Bowles, J.E., "Foundation analysis and design", The McGraw-Hill Companies, NY, 1996.

39. S:T Eriks, "Underground Infrastructures, Handbook for water and waste water networks", 2013 (in Swedish).

40. Abaqus 6.12 Online documentation. Dassault Systèmes Simulia Corp., Providence, 2014.

41. Bazyar Mansoor Khani, M.H., "Dynamic soil-structure interaction analysis using the scaled boundary Finite-Element Method", PhD thesis, University of New South Wales, Sydney, 2007.

42. Das, B.M., Ramana, G.V., "Principles of Soil Dynamic", 2ed, USA, Cengage Learning, 2011.

43. Chopra, A.K., Dynamics of structures, "Theory and applications to earthquake engineering", 2ed, Berkley, Prentice-Hall, Inc.; 2001.

Self-Healing Performance and Microstructural Characterization of Concrete Containing Energetically Modified Cement with a High Volume of Pozzolans

Prof. Dr. Vladimir Ronin
EMC Cement B.V.,
Alvägen 33, SE-973 32 Luleå and
Division of Structural Engineering
Luleå University of Technology, SE-971 87 Luleå
E-mail: emcdev@telia.com

Prof. Dr. Mats Emborg
Division of Structural Engineering
Luleå University of Technology, SE-971 87 Luleå
E-mail: mats.emborg@ltu.se

Prof. em. Dr. Lennart Elfgren
Division of Structural Engineering
Luleå University of Technology, SE-971 87 Luleå
E-mail: lennart.elfgren@ltu.se

ABSTRACT

Self-healing can increase the lifetime and durability of concrete structures. The self-healing properties of concrete made with Energetically Modified Cement (EMC), which has a pozzolan content of up to 70%, have been investigated. In such concretes, pozzolanic reactions within the cement cause the gradual formation of fresh C-S-H gel, which seals cracks as they form. The self-healing of small EMC concrete samples was tested in a laboratory, and field observations of an EMC concrete highway pavement were made. The EMC concrete exhibited fewer cracks than conventional concrete, and was observed to self-heal cracks with widths of up to 0.2 mm.

Key words: Self-healing, cracking, pozzolanic reactions, modified cement binders

1.   INTRODUCTION

1.1   Background

Many countries are experiencing civil infrastructure deterioration so severe that the annual outlay on repair and rehabilitation often exceeds the cost of constructing new infrastructure. This is partly due to the cracking (including thermal cracking, shrinkage cracking, etc.) of concrete during various stages of the hardening process. Concrete deterioration is also a problem in housing and industrial applications, where cracking is unacceptable because of its effects on durability, aesthetic value, hygiene, and acoustic insulation.

In the United States, the annual economic impact associated with the maintaining, repairing, or replacing such deteriorating structures is estimated to be $18-21 billion [1]. About half of all field repairs fail, necessitating re-repairs. Around three-quarters of these failures are attributed to

a lack of durability and the remainder to structural failures. This inadequate performance is often ascribed to inappropriate material selection, the use of a poor application method, or both factors together [2].

In addition to the economic costs of repair and rehabilitation, civil infrastructure deterioration presents social and environmental costs. While these costs have not been well documented or quantified, it is generally agreed that repeatedly repairing civil infrastructure over the course of its service life is decidedly unsustainable.

Consequently, there is great interest in concrete capable of self-healing, i.e. sealing cracks as they form. Such concrete enables the construction of more durable structures with increased lifetimes, both of which are important and desirable in a sustainable society that uses concrete as a major building material. It is therefore important to explore the self-healing capabilities conferred by new cementitious binders.

One such new cementitious binder is Energetically Modified Cement (EMC), which is formed by mechanically activating mixtures of Portland cement with a pozzolan, silica sand or blast furnace slag. A pozzolan is here defined as a siliceous or siliceous and aluminous material that has little or no intrinsic cementitious value but reacts chemically with calcium hydroxide at ambient temperatures when finely divided and exposed to water, forming compounds with cementitious properties. The EMC process was discovered in 1992 at Luleå University of Technology (LTU) and has since been developed extensively [3] - [7].

It is thus interesting to evaluate the self-healing performance of concretes incorporating Energetically Modified Cements and its relationship with the microstructural characteristics of the cement. This paper presents laboratory and field test results relating to the self-healing performance of concretes with EMC.

1.2   Self healing

Various Scandinavian groups have recently studied self-healing concretes [8] - [11]. RILEM's Technical Committee 221 [12] distinguishes between autogenic and autonomic self-healing (see Figure 1) and it has been argued that self-healing phenomena can also be classified in terms of process and action, as shown in Figure 2 [13] [14]. This article concerns autogenic self-healing, i.e. recovery processes involving material components that might be present even if the material had not been specifically designed for self-healing.

Figure 1. Definition of Self-Healing according to RILEM-TC221 [12].

Figure 2. Self-Healing defined in terms of action and process according to references [13] from [14].

Autogenic healing has been attributed to the hydration of unreacted cement (leading to fresh C-S-H gel formation, etc.), the expansion of concrete in crack flanks (i.e. swelling), crystallization of compounds such as calcium carbonate, closing of cracks by solid particles in water, and closing by spalling of loose concrete particles resulting from the cracking itself [8], [9], [14], [15]. Crystallization appears to be the most important mechanism in mature concrete. However, the hardening of many pozzolanic binders continues beyond the first month after pouring, so further hydration and C-S-H gel formation is considered to be the main reason for healing in concrete incorporating these binders. Through cracks in structures exposed to water pressure on one side can also heal via the precipitation of lime in the crack [16]. However, many applications do not involve any such one-sided pressure.

Researchers have examined the effects of diverse factors on self-healing, including crack width; the temperature; water pressure; the composition of the concrete and binder; and the chloride concentration, pH, and hardness of the water to which the concrete is exposed [8], [15], [17]. The relative importance of these factors is of course dependent on the dominant mechanism of self-healing in the structure of interest.

The effects of self-healing on strength are considered to depend on three factors [8], [9], [17]: (a) the moisture content in the crack and the duration of storage; water-stored concrete heals more effectively than concrete exposed to high relative humidity, (b) the initial crack width; smaller cracks seems to heal more completely whereas specimens that are completely broken clearly will not heal efficiently, and (c) the applied pressure; exposure to pressure clearly implies more effective healing than would be possible in a stress-free crack.

1.3 Modifying the binder's particulate structure – Energetically Modified Cement (EMC)

EMC is produced by processing cement with various other inorganic materials in high intensity grinding mills or commuting devices that subject the solids to severe mechanical stress and transient high temperatures, leading to particle surface modification (see Figure 3). These commuting devices have been called "mechano-chemical reactors" instead of traditional mills because the physiochemical processes that occur during comminution (which include phase

transitions, melting and solidification) can induce a range of solid state chemical reactions in the treated material as well as modifying its physical structure. Binders treated in this way can be incorporated into concrete mixtures, yielding new materials with promising properties [3], [4], [18]. Moreover, their usage makes it possible to significantly reduce the proportion of Portland cement in concrete while maintaining and sometimes even improving the concrete's properties [19]-[22]. Both traditional powders (fly ash and blast furnace slag) and new alternatives (fine quartz sand, recycled concrete) can be used, potentially reducing the content of Portland cement in concrete by more than 50 % relative to standard formulations.

A product known as CemPozz is obtained by processing mixtures of pozzolans with 2%-5% ordinary Portland cement using EMC technology. Extensive field tests in the U.S. have shown that replacing up to 70% of the Portland cement in concrete mixtures with CemPozz significantly reduces cracking and greatly increases the concrete's capacity for self-healing of cracks [20].
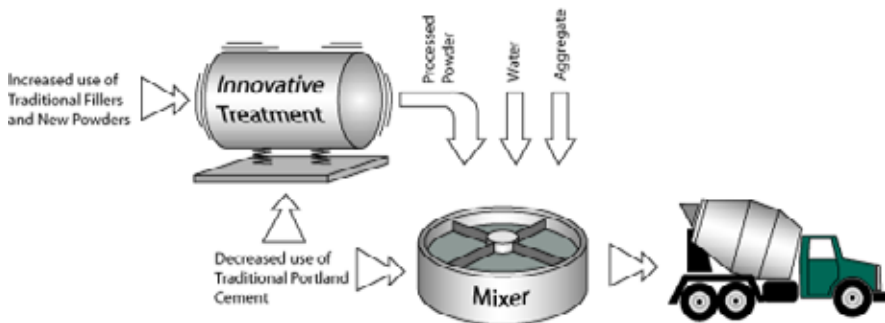
(a)
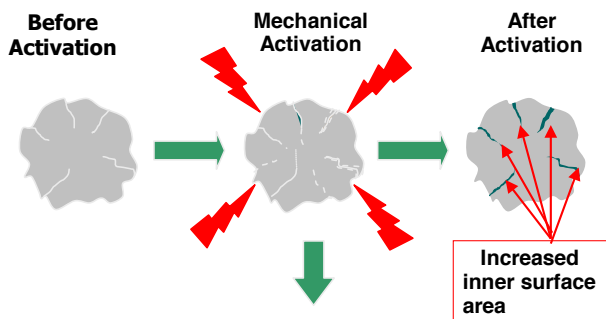
(b)

Figure 3. The key steps in the creation of a durable and environmentally friendly concrete using Energetically Modified Cement (EMC) materials: (a) the overall procedure (b) the mechanical activation process.

2.   EXPERIMENTAL

2.1   General

This paper reports the results of laboratory experiments and field tests on the self-healing performance of different types of concrete. Laboratory tests were performed by LTU and field tests by EMC Cement BV and Texas EMC Products LLC (USA). Microstructure assessments were performed by SINTEF, Norway as a continuation of the field test project, [22]. Preliminary results of these investigations were presented at the XXII Nordic Concrete Research Symposium in Reykjavik 2014 [18].

2.2   Test Program –self-healing in laboratory

Laboratory tests were conducted in 2012 and 2013 at LTU's Complab facility. EMC concrete beams were loaded 28 days after casting using the RILEM 3-point bending protocol [24], as shown in Figures 4 and 5. The loading induced crack formation, enabling assessment of the material's self-healing capabilities. The tested concrete (total amount of binder: 350 kg/m³, w/cm ratio 0.40, max aggregate size 16 mm) contained 40% Portland cement (Byggcement, type Cem II/A-LL, 42.5, Cementa) and 60% CemPozz made from 5% Anläggningscement (type Cem I 42.5N, SR3 MH/LA, Cementa) and 95 % low calcium fly ash. The mean and maximum diameters of the CemPozz particles were 17 microns and 35 microns, respectively, meaning that their size distribution closely matched that of the product examined in the field tests.

If the loading process failed to produce sufficiently wide cracks, the beam was returned to the test frame and the procedure described above was repeated. Once an acceptably large crack had formed, it was locked by gluing a small plate of carbon fibre to one side of the specimen (Figure 5). To assess the compressive strength of the concrete, unloaded control cubes were tested for compressive strength at different ages. The cracked beams were stored in the laboratory in a water bath at a temperature of 20 – 22 °C. The cracks were inspected with an optical microscope at various points in time between 0 and 135 days after their initial formation.

Figure 4. A concrete test beam made with Energetically Modified Cement (EMC) undergoing RILEM 3-point bending [23] at Complab, LTU.

*Figure 5. The cracks were locked by gluing pieces of carbon fibre **to** the sides of the beams.*

2.3 Field observation – self-healing

Field testing was performed on a highway pavement made of CemPozz concrete east of Houston, USA (see Figures 6 and 7). Three 20 km long sections of the pavement were paved with an ECM concrete made with CemPozz mixtures having different CaO contents. In addition, a fourth section was paved with a reference concrete containing no CemPozz. The reference concrete was prepared using a binder consisting of 80 % ordinary Portland cement (OPC) and 20% Class F ash (by mass) with a CaO content of 5%. The three CemPozz concretes were prepared using binders consisting of 50 % OPC and 50 % CemPozz; the CemPozz was prepared using Class F fly ash as a raw material, and had a CaO content of 2 %, 5 %, or 10 %.The regulations of the Texan road authorities limit the maximum CaO content of raw ash used in paving concrete, preventing the assessment of CemPozz with a CaO content above 10%. The total cementitious content of the CemPozz concrete was 300 kg/m^3, its OPC/CemPozz ratio was 1:1 by weight, and its w/cm ratio was 0.30.

The highway sections were paved over a period of four weeks during the summer time. Each section can be assumed to have experienced the same weather conditions and should thus have undergone the same levels of plastic and drying shrinkage. Due to the high humidity (80 – 85 %) during the paving process, the risk of plastic shrinkage cracking was considered to be rather low, and paving contractors working in this region generally do not take measures to protect against evaporation.

However, shortly after casting, all four of the concrete surfaces exhibited cracking, largely due to a combination of plastic and drying shrinkage. Three months after casting, samples with and without drying shrinkage cracks were drilled out from the pavements. Cylindrical samples with diameters of 100 mm and heights of 150 mm were tested in compression immediately after drilling and then subjected to curing in water at room temperature (20-22 °C). In addition, ten paved areas of 25 m^2 each were inspected to determine the average total number of cracks and average crack length at different time points after casting.

Figure 6. Pouring of self-healing concrete on highway IH-10, east of Houston, USA.

Figure 7. Reinforcement ahead of concrete placers on IH-10, east of Houston, USA.

2.4   Test Program – Microstructure Evaluation

To investigate the relationship between cement paste microstructure and the kinetics of crack healing, the microstructure of a cement paste made from a 50/50 blend of OPC and CemPozz was characterized at SINTEF, along with that of a paste prepared using a 50/50 blend of OPC and raw (unprocessed) fly ash The paste samples (cubes with 20 mm long sides) were prepared using CEM I 42.5N with a water-to-binder ratio of 0.40.

Paste samples for DTA/TG (Differential Thermal Analysis/Thermo Gravimetry) analysis were cured for set time periods then crushed to a fine powder and dried at 105 °C to remove physically adsorbed water. The DTA/TG experiments were conducted using a NETZSCH 409 STA with a heating rate of 10 °C/min until 1000 °C and nitrogen as a carrier gas. The sample (≈150 mg) was held in an alumina crucible during the analysis, and alumina powder was used as a reference material. The accuracy of the temperature determined for phase transitions was within ± 2 °C, while the accuracy of the mass loss measurements was within ± 0.3 mg.

MIP/HeP (Mercury Intrusion Porosimetry/Helium Pychnometry) experiments were performed using paste fragments around 5 mm in length. The MIP experiments were conducted with a Carlo Erba Porosimeter (Model 2000), which measures the sample's pore size (radius) distribution over a range of 5 - 50,000 nm, assuming cylindrical pores. The density of solid samples, ρ_s, was determined with a Micrometrics AccuPyc 1330 He-pycnometer, while the particle density, ρ_p, was determined with a Carlo Erba Macropores Unit 120. The accuracies of the total porosity and density measurements were within ± 0.5 and ± 0.01 units, respectively.

3. RESULTS

3.1 Self-healing in laboratory

Figures 8a-c show optical microscope images of a crack whose width ranges from 0.06 to 0.15 mm after different curing periods in the water bath. Due to the high chemical reactivity of CemPozz manufactured with low calcium fly ash (i.e. with a CaO content of ca. 3 %), the first signs of fresh C-S-H gel formation via pozzolanic reactions are apparent within 30 days of curing (see Figure 8b). Self-healing of the crack was complete after about 135 days, and the average penetration depth of the newly formed C-S-H gel was around 0.20 mm (see Figures 8b and c). Without any external intervention, the high volume pozzolan concrete gradually filled the cracks that had formed as the concrete set. It is believed that this was due to the ongoing formation of C-S-H gel within the concrete via pozzolanic reactions.

The high volume pozzolan concrete also exhibited continuous increases in strength over the observation period as a consequence of the ongoing pozzolanic reactions: the concrete had a strength of 85 MPa after 30 days' curing, rising to 94.5 MPa after 150 days. Such strength increases should appreciably increase the concrete's durability.

3.2 Field observation

The field studies conducted in the U.S. showed that the self-healing effect of the high-volume CemPozz concrete has a beneficial impact on concrete strength. Notably, the compressive strength of uncracked concrete samples was very similar to that of samples with self-healed cracks after 180 days of curing (see Table 1). This will undoubtedly increase the concrete's durability and abrasion resistance. The results obtained are consistent with previous findings [25], which indicated that concrete mixtures with higher fly ash contents exhibited enhanced self-healing leading to more effective recovery of compressive and bending strength as well as the dynamic modulus of elasticity after cracking.
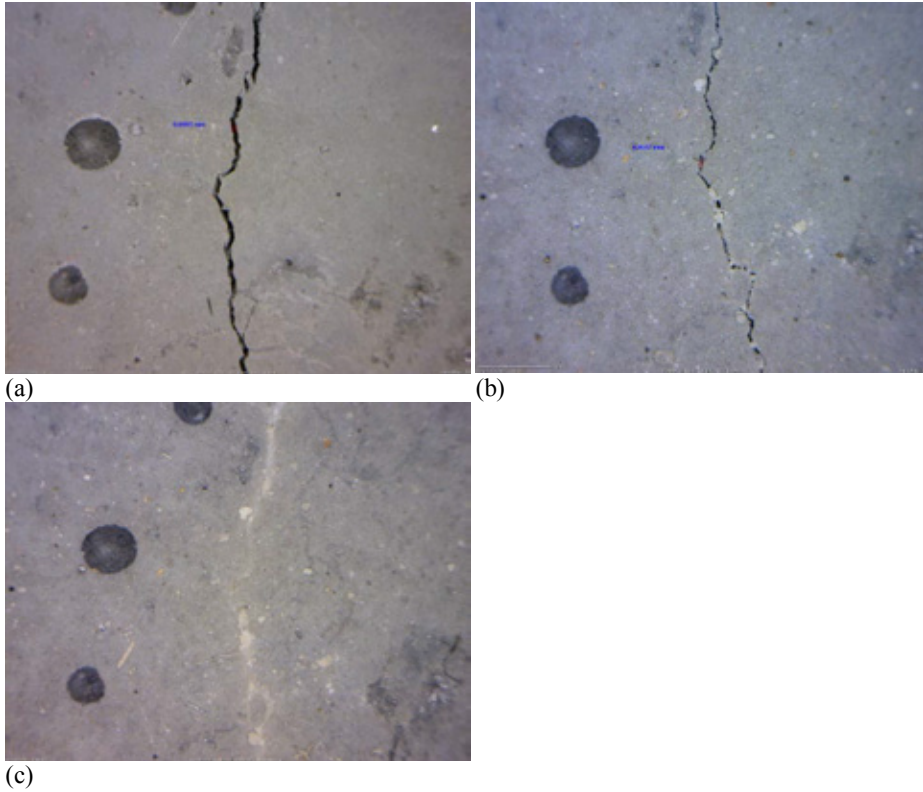
Figure 8. A concrete crack (a) shortly after its formation; (b) 30 days after its formation; and (c) 135 days after formation. Signs of [C-S-H gel] can be seen in (b) and the completely self-healed crack is observed in (c).

The strengths of the concretes examined in the field tests are shown in Table 1 and the kinetics of their self-healing processes are presented in Table 2. Visual inspection of the 25 m^2 observation areas of each pavement section clearly showed that at all ages, the 50% CemPozz concrete had substantially fewer and shorter cracks than traditional 20% fly ash concrete due to its lower levels of drying shrinkage [20]. Table 2 also demonstrates that the average number of cracks in the high volume pozzolan concrete (50 % CemPozz) decreases over time, which is a direct consequence of the self-healing of its micro cracks. This increased self-healing ability is explained by the high pozzolanic activity of CemPozz manufactured with fly ashes having high calcium oxide (CaO) contents.

Table 1. Compressive strength, MPa, of drilled cores collected during field tests in Texas

Type of sample	Compressive strength after 3 months in the field	Compressive strength after 3 months in the field and 3 months under water
Control without drying shrinkage cracks	45.6	53.8
Samples with drying shrinkage cracks	38.7	52.1

Table 2. Number and average lengths of cracks in the 25 m^2 observation areas of pavements with different CaO contents as recorded during field tests in Texas.

Curing period, months	Ref. concrete (20% fly ash), 5% CaO		CemPozz concrete, 2% CaO		CemPozz concrete, 5% CaO		CemPozz concrete, 10% CaO	
	Number of cracks	Average crack length, mm	Number of cracks	Average crack length, mm	Number of cracks	Average crack length, mm	Number of cracks	Average crack length, mm
2	12	24	8	17	9	15	6	11
3	14	22	10	18	10	15	8	12
6	12	18	7	12	5	11	5	8
9	11	17	6	10	4	8	4	6

3.3 Microstructure characterization

The results of Thermo Gravimetry, TG, and porosimetry experiments on the studied cement pastes after curing for up to 2.5 years (50/50 sealed/wet cured) are presented in Tables 3 and 4, respectively. EFAP denotes energetically modified 50/50 OPC/FAP paste, while BFAP is a 50/50 OPC/FAP blended paste.

As shown in Table 3, the total mass loss from the EFAP (energatically modified) paste was only slightly greater than that for the BFAP (blended) paste at most time points, and was actually slightly lower after 910 days' aging, probably because its denser matrix hindered its reactions. The calcium hydroxide (CH) content of EFAP exceeds that of BFAP after one day of aging but decreases more rapidly over time and is below the value for BFAP after 28 days. This indicates that the pozzolanic reaction of fly ash is faster in EFAP (in which it clearly begins after only 1-3 days of aging) than in BFAP (where the reaction apparently starts at some point between 7 and 910 days). This is understandable because the spherical shells of untreated fly ash particles are crushed during the milling process used to produce EFAP, allowing reactions to occur simultaneously on both sides of the glassy fly ash wall [22]. CH is consumed far more rapidly in EFAP paste than in BFAP: after 28 and 910 days' curing, its rate of consumption in EFAP is 13 % and 27 % greater than in BFAP, respectively.

Table 3 Thermal analysis results for Energetically modified (EFAP) and Blended (BFAP) pastes of 50% Ordinary Portland Cement (OPC) and 50% Fly Ash Paste (FAP) as a function of curing time. Results for the two pastes are separated by a slash (EFAP / BFAP).

Curing time	Total mass loss (%)	Degree of hydration (%)	CH (%)	CH/mass loss (%)
6 h / 12 h	6.89 / 7.30	28 / 29	4.11 / 3.90	60 / 53
1 day	8.64 / 7.96	69 / 64	8.65 / 6.92	100 / 87
3 days	9.93 / 9.73	79 / 78	9.28 / 8.67	93 / 89
7 days	10.38 / 10.20	83 / 82	9.18 / 8.62	88 / 85
28 days	11.15 / 10.89	89 / 87	7.37 / 8.25	66 / 76
910 days	13.46 / 14.27	108 / 114	3.99 / 5.78	30 / 41

The general trends revealed in Tables 3 and 4 are that the porosity decreases as a function of time and the specific surface area increases over time as the pores becomes smaller in size but more numerous (possibly indicating the development of gel pores). The average density of solids decreases as a function of time because the amount of crystal water in the paste increases as hydration proceeds. The EFAP paste is less porous than the BFAP paste after around 7 days due to its greater degree of hydration and more rapid pozzolanic reactions. The difference between the pastes is especially pronounced after 910 days.

Table 4 Specific surface area, S_g, particle density (ρ_p), solid density (ρ_s), mercury-accessible porosity (ε_{Hg}) and helium-accessible porosity (ε_{He}) of EFAP / BFAP pastes as a function of curing time.

Curing time	S_g (m^2/g)	ρ_p (kg/m^3)	ρ_s (kg/m^3)	ε_{Hg} (vol%)	ε_{He} (vol%)
6 h /12 h	8.4/9.7	1,300/1,231	2,588/2,519	48.2/47.7	49.8/51.1
1 day	20.0/15.5	1,302/1,243	2,373/2,359	43.7/44.7	45.2/47.3
3 days	32.8/22.7	1,349/1,313	2,264/2,260	39.3/38.4	40.4/41.9
7 days	30.6/20.7	1,377/1,383	2,235/2,248	37.6/35.9	38.4/38.5
28 days	40.2/27.2	1,349/1,371	1,931/2,102	31.7/34.7	30.1/34.8
910 days	35.7/44.7	1,324/1,180	1,609/1,856	23.2/40.5	17.7/36.4

The pore size distributions of the two samples are plotted in Figure 9, revealing that both pastes have a relatively fine pore structure: the average pore openings of EFAP and BFAP are 11 and 22 nm in diameter, respectively. However, the two pastes' pore size distributions are very different. BFAP has a bimodal distribution with substantial numbers of pores having diameters of around 600 nm and the rest being smaller than 100 nm. EFAP, on the other hand, has only a few pores with diameters above 40 nm. The reason why $\varepsilon_{Hg} > \varepsilon_{He}$ after 910 days' curing (see Table 4) is probably that the highly pressurized mercury used to determine ε_{Hg} crushes delicate structures that form in the paste after extensive curing, opening up otherwise inaccessible pores.
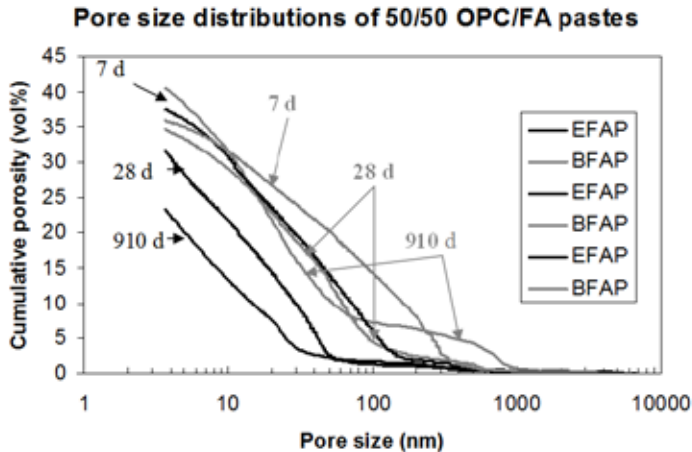
Figure 9. Pore size distribution in EFAP and BFAP pastes at 7, 28 and 910 days.

4.   CONCLUSIONS AND FUTURE WORK

The results of the laboratory and field tests as well as visual inspections of the studied concretes indicate that:

1. Cracks in the surfaces of high volume pozzolan concrete beams were gradually filled in without any external intervention. It is suggested that this was due to the synthesis of C-S-H gel within the concrete, driven by ongoing pozzolanic reactions. The cracks were completely filled in after about 135 days.

2. Crack healing during field tests conducted in the United States was even more rapid than in the laboratory. This may be due to the comparatively low CaO content of the raw ash used in the concrete studied in the field test, and the higher curing temperature.

3. Self-healing of drying shrinkage cracks had a positive impact on the long-term strength of the tested concrete. After 90 days of curing, the compressive strengths of the control samples (without cracks) and concrete samples with self-healed cracks were about the same.

4. The number and length of cracks in paving made with 50 % CemPozz (EMC-processed pozzolan) decreased over time. This process was accompanied by a recovery of the concrete's strength.

5. Observations of a highway pavement indicated that increasing the content of calcium oxide had a favourable effect on the kinetics of crack healing in concrete mixes with 50% Portland cement replacement.

6. Cement pastes containing 50% by mass of highly reactive EMC-treated pozzolans (i.e. CemPozz) exhibited high levels of hydration with lower levels of porosity and much finer pores than traditional OPC/Fly ash blends. These features are expected to increase the self-healing capacity and overall durability of EMC concrete.

Future studies will build on the results presented herein by seeking to validate the hypothesis that voids and cracks up to 0.2 mm wide can be filled by self-healing, and will assess the effect of such self-healing on the durability of concrete structures. In addition, efforts will be made to identify boundary conditions that can be used to select appropriate EMC concrete mixtures for various applications such as road construction.

5.   ACKNOWLEDGEMENTS

REFERENCES

1. The Strategic Development council (SDC), "Vision 2020. A Vision for the Concrete Repair, Protection and Strengthening Industry". 2006, 29 pp. Available at: http://www.concretesdc.org/_pdfs/Vision2020-Version1.0_%20May2006.pdf (Accessed 2014-08-29)
2. Li, V.C. and Herbert, E., " Robust Self-Healing Concrete for Sustainable Infrastructure", *Journal of Advanced Concrete Technology*, Vol. 10, 2012, pp. 207-218
3. Ronin, V. and Jonasson, J-E., "Investigation of the Effective Winter Concreting with the Usage of Energetically Modified Cement (EMC) - Material Science Aspects." *Report 1994:03*, Division of Structural Engineering, Luleå University of Technology, Luleå, Sweden, 1994, 24 pp.
4. Ronin, V., "Process for Producing Blended Cements with Reduced carbon Dioxide Emissions", US Patent nr. 6, 2005,936,098 B2.
5. Rao, K. H., Ronin, V. and Forsberg E., "High Performance Energetically Modified Portland Blast-furnace Cements", Proceedings of the *10th International Congress of the Chemistry of Cement* (Ed. by H. Justnes), Gothenburg, Sweden, June 1997. Inform Trycket AB, Gothenburg, 3ii104, 9 pp. (ISBN 91-630-5497-5).
6. Johansson, K., Larsson, C., Antzutkin, O. N., Forsling, W., Rao, K. H. and Ronin V., "Kinetics of the Hydration reactions in the Cement Paste with Mechanochemically Modified Cement by ^{29}Si Magic-Angle-Spinning NMR Study", *Cement and Concrete Research*, Vol. 29, 1999, pp. 1575-1581
7. Justnes, H., Dahl, P.A., Ronin, V., Jonasson, J.-E., and Elfgren, L., "Microstructure and performance of energetically modified cement (EMC) with high filler content". *Cement and Concrete Composites*, Vol 29, 2007, pp. 533-541. Elsevier
8. Fagerlund, G. & Hassanzadeh, M., "Self-healing of cracks in concrete long-term exposed to different types of water. Results after 1 year's exposure". Report TVBM-3156, Lund Institute of Technology, Division of building Materials, 2010, 58 pp.
9. Fagerlund, G. & Hassanzadeh, M., "Self-healing of cracks in concrete exposed to different types of water. Effects on chloride penetration". Report TVBM-3161, Lund Institute of Technology, Division of building Materials, 2011, 75 pp.
10. Fjälberg, L., "Självläkande betong", (In Swedish), CBI-nytt, The Swedish Cement and Concrete Institute, No 1, 2014, 2 pp.
11. Wallevik, Olafur H.; Bager, Dirch B.; Hjartarson, Björn and Wallevik, Jon E., Editors (2014): Environmentally Friendly Concrete – Eco-Crete. Proceedings of the International

Symposium on Eco-Crete, Reykjavik, Ice3land, 13-15 August 2014. ICI Rheocenter – Reykjavik University & Innovation Center, Iceland, xii + 456 pp

12. RILEM technical committee –TC221-SHC, Self-healing of Cement Based Materials, http://www.rilem.org/docs/2013142416_unedited-version-221-shc.pdf

13. de Rooij, M. R., Schlangen E. (eds) "Self-healing phenomena in cement-based materials", Draft of State-of-the-Art Report of RILEM Technical Committee 221 – SHC (Quoted from Mihashi et al [13]

14. Mihashi H., Nishiwaki T., "Development of Engineered Self-healing and Self-Repairing Concrete State-of-the-Art Report, *Journal of Advanced Concrete Technology* ,Vol. 10, 2012, Japan Concrete Institute, pp. 170-184

15. Yang, Y., Lepech, M. D., Yang, E. and Li, V. C., "Autogenous healing of engineered cementitious composites under wet-dry cycles." *Cement and Concrete Research*, 2009, 39, pp 382-390.

16. Edvardsen C., "Water Permeability and autogenous healing of cracks in concrete", *ACI Materials Journal*, Vol 96, 1999 (Quoted from Fagerlund & Hassanzadeh [8])

17. Wieland, Ramm, Michaellea, Biscoping, "Autogenous Healing and Reinforcement Corrosion of Water-penetrated Separation Cracks in Reinforced Concrete, *Journal of Nuclear Engineering and Design,* Vol. 179, 1998, pp. 191- 200 (quoted from Yang et al [14])

18. Ronin, V., Jonasson, J-E., and Elfgren, L., "Self-Healing Concrete – Results with Energetically Modified Cement (EMC)", Proceedings XXII Nordic Concrete Research Symposium, Reykjavik, 13-15 August, *Nordic Concrete Research*, Vol. 50, No 2/2014, Oslo, pp. 57-60.

19. Ronin, V., Jonasson, J-E., and Hedlund, H., "Advanced modification technologies of the Portland cement based binders for different high performance applications. Proceedings of the *10th International Congress on the Chemistry of Cement* (Ed. by H. Justnes), Gothenburg, Sweden, June 1997. Inform Trycket AB, Gothenburg, 2ii077, 8pp. ISBN 91-630-5496-5.

20. Pike, C., Ronin, V., and Elfgren, L., "High volume pozzolan concrete: Three years of industrial experience in Texas with CemPozz". *Concrete In Focus Magazine*, 2009, Vol.8, No. 2. March/April, pp. 22-27.

21. Justnes, H., "Concrete with high volume of supplementary cementing materials and admixtures for sustainable and productive construction". Indian Concrete Industry, ICI Update, Vol 2, Feb 2011, No 2, pp 12-26,

22. Justnes, H., Elfgren, L. and Ronin, V., "Mechanism for Performance of Energetically Modified Cement versus Corresponding Blended Cement", *Cement and Concrete Research*, Vol. 35 2005, pp. 315-323.

23. RILEM, "Determination of the Fracture Energy of Mortar and Concrete by means of three-point bending tests on notched beams". *Materials and Structures*, Vol 18, No 106, 1985, pp.285-290

24. Nishiwaki, T., Mihashu, H., Byong-Koog, J., Kazuaki, M, "Development of self healing System for Concrete with Selective Heating around Crack", *Journal of advanced Concrete Technology*, Japan Concrete Inst., Vol 4, No 2, 2006, pp. 267 – 275,

25. Na S.H., Hama Y., Tanguchi M., Katsura O., Sagawa T., and Zakaria M., " Experimental Investigation on Reaction Rate and Self-healing Ability in Fly Ash Blended Cement Mixtures." *Journal of Advanced Concrete Technology*, Vol.10, 2012, pp. 240-253

Methods to Optimize Aggregate Distribution – Evaluation by Concrete and Mortar Experiments

Tekn Lic, Niklas Johansson
PhD-student
Cementa AB
P.O. Box 104, SE-624 22 Slite
Div. Structural and Construction Engineering
Luleå University of Technology
SE-971 87 Luleå
E-mail: niklas.johansson@cementa.se / niklas.johansson@ltu.se

Prof. Dr. Mats Emborg
Div. Structural and Construction Engineering,
Luleå University of Technology
SE-971 87 Luleå
Betongindustri AB
P.O. Box, SE-473 12 Stockholm
E-mail: mats.emborg@ltu.se / mats.emborg@betongindustri.se

ABSTRACT

A proper mix design optimizes the environmental impact and the cost effectiveness of a concrete mix. A minimum cement paste content is desirable without jeopardizing the concrete properties. As the paste content is dependent on the packing properties of the aggregates it is of interest to estimate the packing correctly. Three methods to optimize the aggregate distribution have been evaluated by concrete tests: one curve fitting method and two particle packing methods. Also mortar tests were performed. It is shown that the methods suggest very different aggregate distributions for an optimum concrete mix and they cannot handle fine crushed aggregate consuming a lot of mixing water correctly.

Key words: Aggregate, Mix design, Fresh concrete, Mortar, Cement paste

1.   INTRODUCTION

The environmental impact and the cost effectiveness of concrete highly depend on the cement paste content as cement is responsible for a major part of the CO_2 emissions in a concrete, see e.g. [1]. Water cement ratio, binder types, aggregates and admixtures have a big impact on the cement paste content in the concrete and it is of interest in mix design to optimize the paste content without jeopardizing the concrete properties. Moreover, 60-70% of the concrete volume consists of aggregate i. e. its properties and distribution have a large influence on the concrete performance.

Crushed fine aggregates have been introduced in concrete production as a replacement for 0-8 mm natural aggregate. The crushed fine aggregates have normally a higher content of fines (< 63 μm) and a flakier shape which result in higher requirements of water, binder and admixture [2]. The shape of the crushed particles can be adjusted by different crushing processes. For instance vertical-shaft impactors (VSI:s) can be used to cubisize flaky particles but the process generates a large amount of fines.

One problem today is that the aggregate properties can be described in many ways among others: sieve curve, flakiness index, packing density, flow value, surface texture. Furthermore there exist no standardized (package of) test methods that evaluate if the aggregate is suitable for concrete production. For crushed fine aggregates 0-2 mm, these test methods can give an indication how the concrete rheology is affected but none of them can be used as a fundamental parameter [2].

However it is clear that the aggregate distribution in the concrete can to some extent be based on optimization curves and/or particle packing models to provide a low air void ratio of the particles leading to reduced cement paste content [1], [3]. Thus, loose and compacted packing measurements of crushed aggregate fractions tend to show a rather good correlation with concrete rheology [2].

Hence, the purpose with this examination is to evaluate three methods to optimize the aggregate distribution in concrete and to study if the methods are suitable for crushed aggregate fractions. The research question is if the methods can be an input to the concrete mix design with suitable fresh concrete behaviour.

2. METHOD

2.1 Aggregate characterization

The following types of aggregate were used in this study

   a) 0-4 mm crushed and cubisized rock
   b) 0-8 mm natural sand
   c) 4-8 mm crushed and cubisized rock
   d) 8-16 mm crushed and cubisized rock
   e) 8-16 mm crushed rock
   f) 8-16 mm natural stone

A VSI-crusher has been used by the aggregate supplier to make the crushed particles more cubical. Particle density, water absorption, sieve curve, flakiness index, loose particle packing and compressive particle packing were tested for each fraction. In the packing trials, the whole aggregate fraction was used i. e. no more fine or coarse material than the specified fractions was separated from the aggregate fraction by sieving.

The loose particle packing tests were performed by simply pouring the aggregate fraction into a cylinder, see Figure 1, and the upper surface was adjusted. The packing value, φ as % by volume is calculated by the following equation

$$\varphi = 1 - \frac{\rho_P - \frac{m}{V}}{\rho_P} \qquad (1)$$

ρ_P = solid density, kg/m^3
m = mass of aggregates, kg
V = cylinder volume, m^3

 A one litre cylinder was used for aggregate fractions up to 8 mm and a five litre cylinder was used for the 8-16 mm fractions. The packing values were not adjusted regarding the size of the cylinder. The compressive particle packing value was determined by filling a five litre cylinder in three levels. Each level was compacted by 80 hits on a jolting table, see Figure 2.

Figure 1 – Testing of loose particle packing.

Figure 2 – Testing of compressive particle packing.

2.2 Methods to optimize aggregate distribution

Three models of optimizing the aggregate distribution were studied.

1. Fuller curve
2. Toufar model
3. 4C-packing

The Fuller curve is an optimum sieve curve presented by Fuller & Thompson [4] and it is often used in traditional concrete mix design. The Fuller curve optimizes the aggregates in the concrete, however not the whole particle mix. According to Vogt [3] the Fuller curve ensures continuous grading but not the highest possible grading.
The Fuller curve P(d) is based on the following equation

$$P(d) = \left(\frac{d}{d_{max}}\right)^{0,5} \qquad (2)$$

d = particle size, mm
d_{max} = largest particle size, mm

The required input to the Fuller curve model is the sieve curve of each aggregate fraction, i.e. no packing value is considered.

The Toufar model is a particle packing model that was initially developed for binary systems but can also be used for three aggregate fractions [5], [6]. According to the inventors of the model [5], the packing density depends on the diameter ratio of the two particle fractions that are to be mixed. Ideally, it is assumed that each of the fine particles is placed exactly between four course particles. Input data to the model, which has been modified by Goltermann et al. [6], includes packing density φ and characteristic diameter d_{char} of each material used in the aggregate combination. It is the modified Toufar model that has been used in this examination.

The 4C-packing concept is a computer software based on the Linear Density Packing Model [7]. The software was developed by DTI in Denmark and can be used as a base for concrete mix design. The 4C-tool calculates the total packing densities for various mixed fractions of aggregate and thus suggests an optimized grading curve. Input data needed is particle density, sieve curve and particle packing value of each aggregate fraction. There is also a parameter called μ that needs to be decided. The μ-value quantifies the so called loosening effect and will normally be in the range of 0.07 - 0.13 [8]. The value indicates possible ratio between small and large particles. Moreover, spherical particles have higher μ-value than flaky particles.

2.3 Concrete trials

Concrete recipes were created based on the suggested optimum aggregate distribution as an output from the three methods above. The following aggregate compositions were tested.

  I.   0-8 mm natural sand + 8-16 mm natural stone (aggregate b and f above).
  II.   0-4 mm crushed and cubisized rock + 4-8 mm crushed and cubisized rock + 8-16 mm crushed and cubisized rock (a, c and d).
 III. 0-4 mm crushed and cubisized rock + 4-8 mm crushed and cubisized rock + 8-16 mm crushed rock (a, c and e).

Concrete mixtures with two *w/c* (0.40 and 0.65) were tested with a fixed dosage of superplasticizer per cement weight, 0.4% for *w/c* 0.40 and 0.1% for *w/c* 0.65. Concrete batches of 20 litres were mixed and slump, density and air content were documented on the fresh concrete. The water cement ratio was kept constant. The cement paste content was varied to change the consistency.

2.4   Mortar rheology

The rheology of the mortar phase (< 1.0 mm particle diameter) from the fresh concrete was tested by sieving a mortar sample using a 1.0 mm sieve and a bottom container. Approximately 500 gram of the fresh concrete was put on the sieve and the bottom container that were placed on the vibrating table. By vibration it was possible to collect mortar sample of approximately 50 gram to be examined in a rheometer of type TA-Instruments AR 2000 ex, see Figure 3.

Figure 3 Rheometer TA-Instruments AR 2000 ex.

The used geometry in the rheometer is a serrated cup with diameter 32.0 mm and a serrated cylinder with diameter 24.0 mm, which provides a gap of 4 mm. The height of the cylinder is 60.0 mm. The measurement testing sequence uses a 10 seconds pre-shear rate at 300 s^{-1} followed by 5 different shear rates in descending order; 300, 240, 180, 120, 60 s^{-1}. Each shear rate lasts for 15 seconds and the average torque is read off the last 5 seconds. The Bingham model is used to calculate the yield stress and plastic viscosity.

3.   RESULTS

3.1   Aggregate properties

The sieve curves of the aggregates, see Figure 4, show that the 0-4 mm crushed and cubisized material contains more fine particles than the natural, which means an increased water demand. It is also seen that the crushed 8-16 mm aggregate demonstrates a large amount of particles (36%) passing the 8 mm sieve.

Other properties of the aggregates used are shown in Table 1, where it is observed that there is a big difference between the aggregates regarding loose packing. The difference is smaller for compressive packing since the crushed materials gets more compacted with this packing method compared to the natural material.
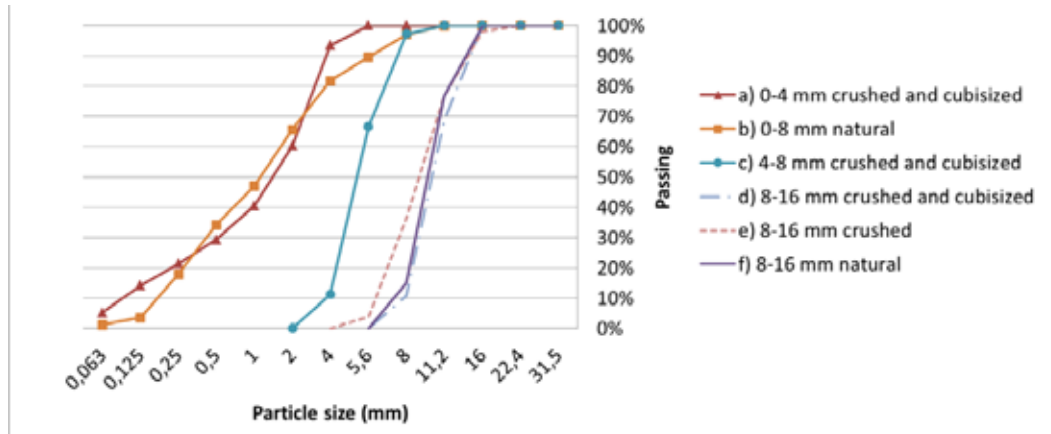

Figure 4 – Sieve curves for the aggregates used in this study.

Table 1 – Aggregate properties. Solid density is measured according to EN 1097-6 and Flakiness index according to EN 933-3. Packing values are presented as % by volume.

	Solid density	Flakiness index	Loose Packing	Comp. Packing	Increased Packing Loose to Comp
	(kg/m³)	(%)	(%)	(%)	(%)
a) 0-4 mm crushed + cubisized	3020	-	61.7	76.4	23.8
b) 0-8 mm natural	2650	-	66.3	76.8	15.8
c) 4-8 mm crushed + cubisized	3100	-	54.4	61.1	12.3
d) 8-16 mm crushed + cubisized	2950	14	53.3	59.7	12.0
e) 8-16 mm crushed	3110	22	48.5	55.5	14.4
f) 8-16 mm natural	2660	4	60.5	64.8	7.1

3.2 Aggregate compositions

The aggregate properties above were used as input data to computer models of the methods (Section 2.2). The outcome, i. e. the optimum distribution for the highest packing value is presented in Table 2. The μ-value in 4C-packing was set to 0.10 for natural aggregates and 0.07 for crushed aggregates according to recommendations [8].

Table 2 – Optimum aggregate distributions presented as % by volume for composition I - III.

Aggregate Composition	Fuller	Toufar		4C-packing	
		Loose Pack	Comp Pack	Loose Pack	Comp Pack
I					
0-8 mm natural	**61%**	43%	**50%**	49%	**42%**
8-16 mm natural	**39%**	57%	**50%**	51%	**58%**
II					
0-4 mm crushed + cubisized	**55%**	**43%**	54%	39%	**57%**
4-8 mm crushed + cubisized	**12%**	**19%**	14%	0%	**0%**
8-16 mm crushed + cubisized	**33%**	**38%**	32%	61%	**43%**
III					
0-4 mm crushed + cubisized	**55%**	**50%**	66%	65%	**75%**
4-8 mm crushed + cubisized	**0%**	**19%**	11%	0%	**4%**
8-16 mm crushed	**45%**	**31%**	23%	35%	**21%**

It is shown that there are big differences in optimum aggregate combination depending on method and packing technique. One logic reflection is that the 8-16 mm crushed aggregate is a flaky material with low particle packing and therefore the particle packing models suggest a very low amount (21-35%) from that fraction. Another observation from Table 2 is that the 4C-packing model avoids using the 4-8 mm fraction – the reason of this is not clear.

The combinations in bold characters in the table were used in the concrete trials where compressive packing values were solely chosen for 4C-packing based on the instructions in the user´s manual [8]. From the Toufar model results, the most realistic aggregate composition mix was chosen based on the authors´ experience.

3.3   Concrete results

The results from the concrete trials with aggregate composition I, see Figure 5, show that all three methods work quite well for natural aggregates with quite spherical particles. The required cement paste content to reach 200 mm slump (consistency class S4 – upper limit) was 310 – 320 litres for *w/c* 0,40 and 300 litres for *w/c* 0.65. The corresponding cement contents are approximately 400 kg for *w/c* 0.40 and 285 kg for *w/c* 0.65.

The lowest paste volume needed, i. e. the lowest environmental impact and thus the "best composition", is obtained by means of the 4C-packing. However these concrete mixes were very unstable at the visual inspection which is explained by a very high amount of 8-16 mm aggregate (58%). Instead, it was judged that the Toufar model and the Fuller curve gave the most convincing concrete mixes regarding consistency and robustness for aggregate composition I, despite a somewhat larger amount of cement paste needed.
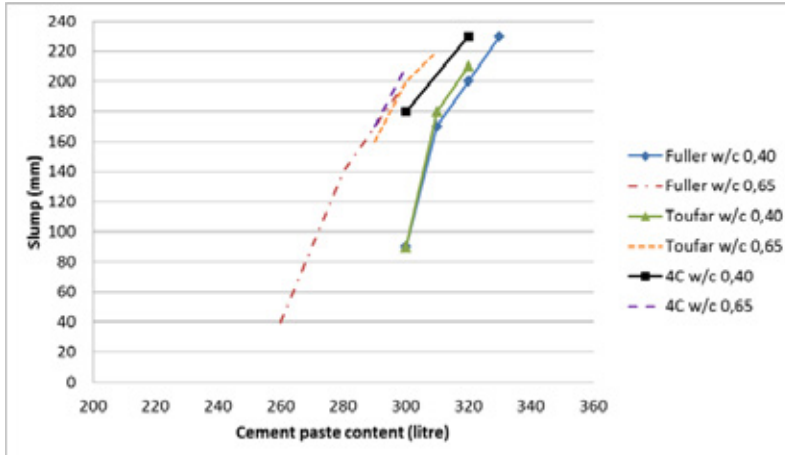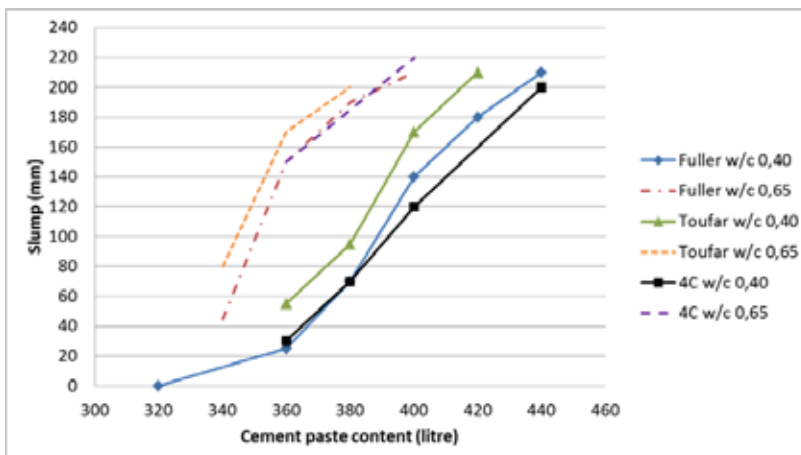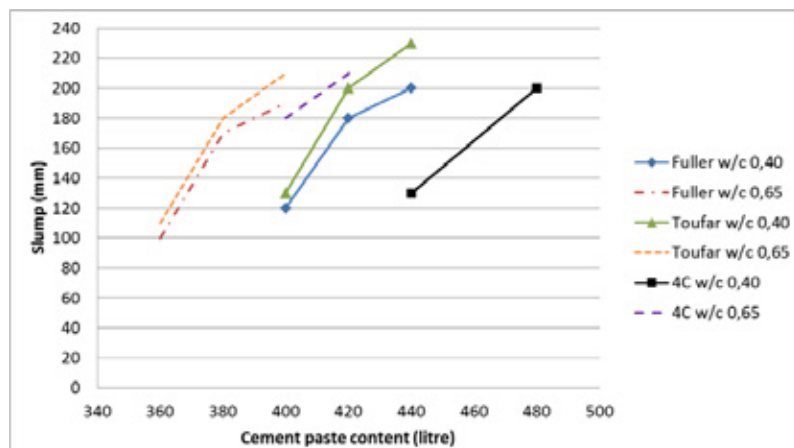
Figure 5 – Slump as a relation to cement paste volume for concrete with aggregate composition I. Fuller: 61% 0-8 mm ; Toufar 50% 0-8 mm ; 4C 42% 0-8 mm.

With aggregate composition II, the clear impact of aggregate performance on required cement paste content is observed especially at low w/c ratios, see Figure 6. Compared to the natural aggregates in Figure 4, the required cement paste content to reach 200 mm slump has increased by approximately 100 – 120 litres when 100% crushed and cubisized aggregate is used.

It is also observed in the figure that there is a correlation between the cement paste content and the amount of 0-4 mm aggregate in the mix i. e. the lowest volume of fine particles, as suggested by the Toufar model, leads to the lowest paste content needed. Regarding fresh concrete performance, none of the mixes showed any tendencies to segregation. All of the *w/c* 0.40 concretes have a high viscosity due to the high amount of fines.

Figure 6 – Slump as a relation to cement paste volume for concrete with aggregate composition II. Fuller: 55% 0-4 mm ; Toufar 43% 0-4 mm ; 4C 57% 0-4 mm.

For composition III, with a change of coarse aggregate type, the required cement paste content is even higher, see Figure 7. Due to the poor particle packing values for the new crushed 8-16 mm aggregate (some 3 - 5 % lower than the cubisized 8 – 16 mm, see Table 1), the packing models suggests this fraction on a low level. Instead, this leads to high amounts of 0-4 mm crushed and cubisized material, which consumes a lot of water which in turn has a negative influence on the concrete.

The optimal packing based on the 4C-packing software suggest 75% of 0-4 mm which is rather unrealistic as the required cement paste content get very high. Again, it seems that the Toufar model is the best method for aggregate composition III, i. e. the method suggests the lowest cement paste needed without having a negative influence on the concrete performance as judged from the visual inspection. It is also noted that the concretes with *w/c* 0.40 were very viscous.

Figure 7 – Slump as a relation to cement paste volume for concrete with aggregate composition III. Fuller: 55% 0-4 mm ; Toufar 50% 0-4 mm ; 4C 75% 0-4 mm.

The air content was tested in the fresh concrete, see Figure 8 and 9. The increased slump was caused by an increased cement paste content and not by addition of superplasticizer since that dosag was constant. The results show that there is a general difference in air content between the *w/c* ratios. A possible reason is the difference in viscosity of the cement paste. A low viscosity (*w/c* 0.65) makes it easier for the entrapped air to release from the concrete. For *w/c* 0.65 also a relation between the slump and the air content can be observed i. e. a higher slump value gives lower air content. In the concrete with *w/c* 0.40 there are two low air contents that differ from the others which are obtained with concretes with aggregate composition I and a high amount (58%) of 8-16 mm aggregates.
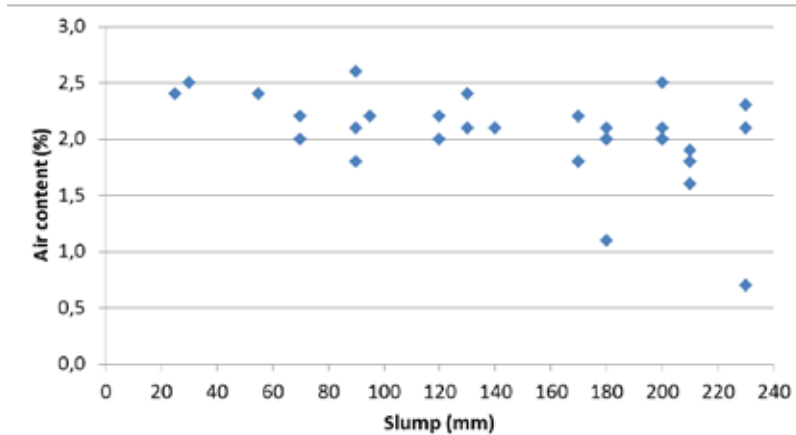
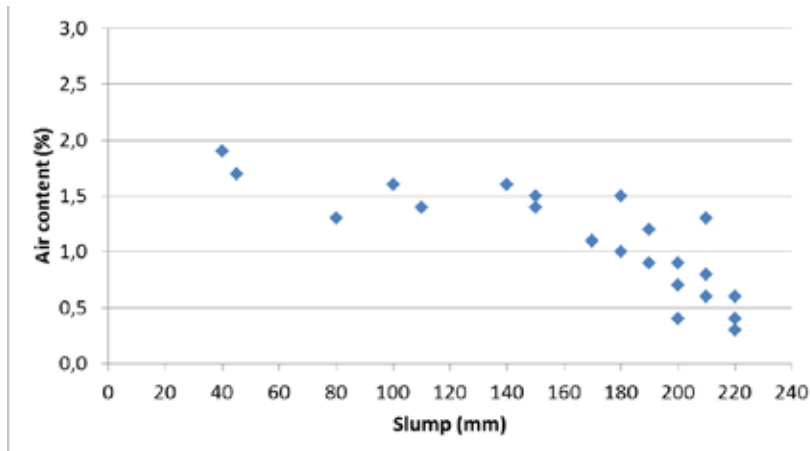*Figure 8 – The relation between slump and air content at w/c 0.40.*

Figure 9 – The relation between slump and air content at w/c 0.65.

3.4   Mortar results

The rheolocical properties expressed as yield stress and plastic viscosity are presented in Figures 10 - 12. It is shown that the plastic viscosity increases by using crushed aggregates instead of natural, compare Figures 11 and 12 with Figure 10. This is expected since there are more fine particles in the 0-4 mm crushed and cubisized compared to 0-8 mm natural that logically increases the stiffness (i. e. yield stress) and viscosity of the mortar. For all compositions, the yield stress and plastic viscosity decreases by increasing the cement paste content in general. The results with composition II and III with crushed aggregates indicate that the distribution by the Toufar model has the lowest plastic viscosity. This corresponds well to the lower amount of 0-4 mm crushed and cubisized material suggested by the model as compared with the other methods.
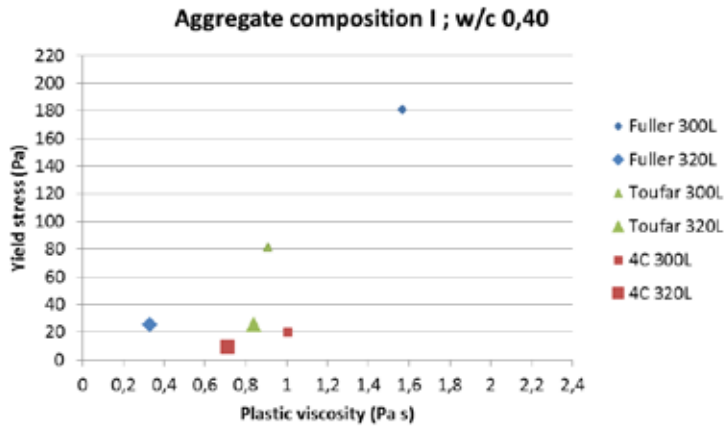
Figure 10 – Rheology of the mortar phase < 1.0 mm extracted from concrete with aggregate composition I, different cement paste contents and aggregate distributions.
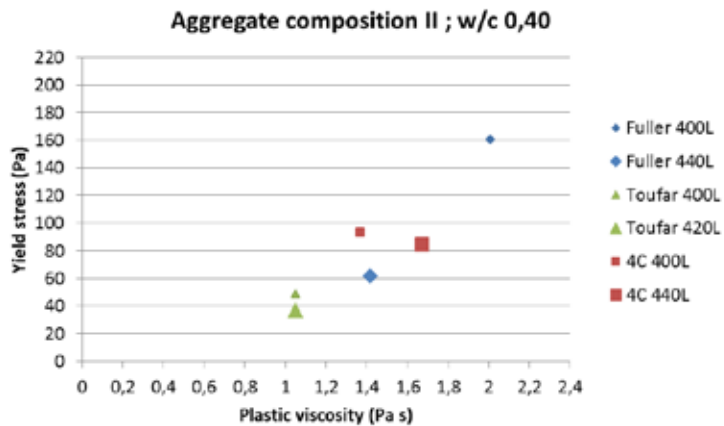
Figure 11 – Rheology of the mortar phase < 1.0 mm extracted from concrete with aggregate composition II, different cement paste contents and aggregate distributions.
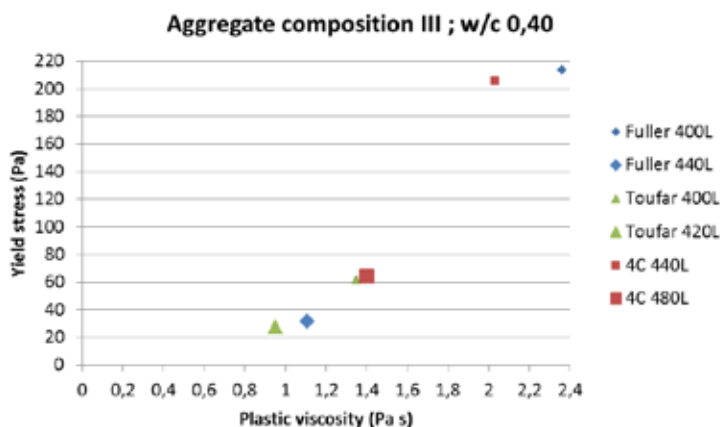
Figure 12 – Rheology of the mortar phase < 1.0 mm extracted from concrete with aggregate composition III, different cement paste contents and aggregate distributions.

The relation between concrete slump and mortar yield stress is presented in Figure 13. A tendency of decreasing slump value by higher mortar yield value is seen. The correlation is quite good for aggregate composition I but for II and III the scatter is evident.
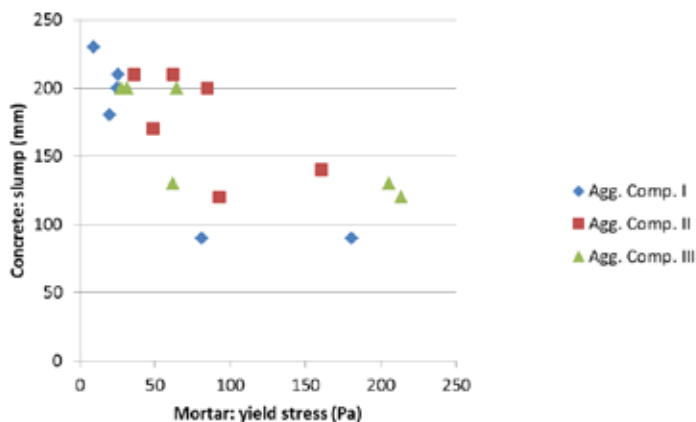
Figure 13 – The relation between concrete slump and mortar yield stress

4.   DISCUSSION AND CONCLUDING REMARKS

Crushed aggregate in all fractions is already a reality for many concrete producers and the use of it will increase in the future. New opportunities with larger numbers of aggregate fractions to combine at the concrete plant will be possible but there will also be challenges to handle flaky particle shapes and more fine particles of the crushed aggregate than with natural aggregate.

In this study some existing methods to optimize the aggregate distribution were tested by laboratory test of fresh concrete behaviour. Interesting and logical results are obtained e. g. that

the slump i. e. the consistency increases by increasing cement paste and that the output aggregate compositions from the methods suggest complete different concretes.

It is thus obvious that these methods are not fully suitable to optimize all the fractions of crushed aggregates among other things since the curve optimization and particle packing models do not take the water demand into account. In this case, the 0-4 mm crushed and cubisized material used, despite a high packing value, is a poor material for concrete production since it consumes a lot of mixing water. Thus, there is a risk that the suggested percentage of fine aggregates will be too high and the need for cement paste gets high for achieving an acceptable fresh concrete consistency.

Another disadvantage with the methods of aggregate optimization tested is that the w/c ratio is not taken into account and the aggregate distribution will be the same for all concrete qualities, from the lowest strength class to a high strength concrete. Normally, according to experience of concrete engineers, the coarse aggregate fraction is increased when the w/c gets lower since the amount of fine particles (cement) increases.

The results in this study also show that the air content in the fresh concrete depends on the *w/c*-ratio and the consistency. It might be possible to create more accurate concrete recipes by choosing air content based on the concrete quality and consistency class.

The method to evaluate the concrete rheology, by testing yield stress and plastic viscosity on a mortar with $d_{max} < 1$ mm extracted from the fresh concrete, seems promising. The mortar results look logical with a good correlation to the concrete behaviour.

REFERENCES

1. Fennis, S.A.A.M., "Design of ecological concrete by particle packing Optimization", TU Delft. Doctoral thesis, 2010, 256 pp.
2. Cepuritis, R., "Effects of Concrete Aggregate Crushing on Rheological Properties of Concrete and Matrix" Norwegian University of Science and Technology, Trondheim. Master Thesis, 2011, 236 pp.
3. Vogt, C., "Ultrafine Particles in Concrete – influence of ultrafine particles on concrete properties and application to concrete mix design" Royal Institute of Technology, Stockholm. Doctoral Thesis, 2010, 155 pp.
4. Fuller, W.B., & Thompson, S.E., "The laws of proportioning concrete", Transactions of the American society of civil engineers 33, 1907, pp. 222-298.
5. Tofar, W., Born, M., Klose, E., " Contribution of optimisation of components of different density in polydispersed particles systems", Freiberger Booklet A, 1976, pp. 29-44.
6. Goltermann, P., Johansen, V., Palbøl, L., "Packing of aggregates: An Alternative Tool to Determine the Optimal Aggregate Mix", ACI Materials Journal, Vol 94 (5), 1997, pp. 435-443.
7. Stovall, T., Larrard, F.de., Bull, M., "Linear Density Packing Model of Grain Mixtures", Powder Technology, Vol 48, 1986, pp. 1-12.
8. Pade, C., Nyholm Trane, L., Kaasgaard, M., "4C-packing – User´s manual", Version 3.0, Danish Technological Institute, 2009, 24 pp.

Research Council and Editorial Board for Nordic Concrete Research

Active reviewers for Nordic Concrete Research as per December 2014

DENMARK	
Dr.	Dirch H. Bager
Dr.	Mette Glavind
Prof., Dr.	Per Goltermann
Mr.	Oscar Klinghoffer
Prof., Dr.	John Forbes Olesen
Mr	Claus Pade
Prof., Dr.	Eigil V. Sørensen
Prof., Dr.	Jens Peder Ulfkjær
FINLAND	
Dr.	Klaus Juvas
Dr.	Matti V. Leskala
Prof., Dr.	Jussi Mattila
Dr.	Jouni Punkki
Mr.	Juha Valjus
ICELAND	
Mr.	Einar Einarsson
Mr.	Haukur J. Eiriksson
Dr.	Gisli Gudmundsson
Mr.	Karsten Iversen
Mr.	Torfi G. Sigurdsson
Mr.	Sveinbjörn Sveinbjörnsson
Dr.	Jon E. Wallevik
Prof., Dr.	Òlafur H. Wallevik
Prof., Dr.	Børge J. Wigum
NORWAY	
Dr.	Helge Brå
Ms.	Danielle Bosnjak
Mr.	Anton Gjørven
Mr.	Steinar Helland
Dr.	Bernt Jacobsen
Prof., Dr.	Terje Kanstad
Dr.	Terje F. Rønning
Mr.	Tor Kristian Sandaker
Mr.	Sverre Smeplass
Mr.	Hans Stemland
SWEDEN	
Prof., Dr.	Anders Ansell
Dr.	Thomas Blanksvärd
Prof.	Lennart Elfgren
Prof., Dr.	Mats Emborg
Prof., Dr.	Kent Gylltoft
Prof., Dr.	Mikael Hallgren
Prof., Dr.	Jan-Erik Jonasson
Prof., Dr.	Björn Lagerblad
Prof., Dr.	Karin Lundgren
Prof., Dr.	Tang Luping
Prof., Dr.	Per-Erik Petersson
Prof., Dr.	Johan Silfwerbrand
Dr.	Peter Utgenannt